Modeling of Hall thruster lifetime and erosion mechanisms

by

Shannon Yun-Ming Cheng

S.B., Aeronautics and Astronautics, Massachusetts Institute of Technology (2000)

S.M., Aeronautics and Astronautics, Massachusetts Institute of Technology (2002)

Submitted to the Department of Aeronautics and Astronautics
in partial fulfillment of the requirements for the degree of
Doctor of Philosophy in Space Propulsion
at the
MASSACHUSETTS INSTITUTE OF TECHNOLOGY
June 2007

Author .....
Department of Aeronautics and Astronautics
25 May 2007

Certified by .....
Manuel Martinez-Sanchez
Professor of Aeronautics and Astronautics
Thesis Supervisor

Certified by .....
Jaime Peraire
Professor of Aeronautics and Astronautics

Certified by .....
Oleg Batishchev
Principal Research Scientist

Accepted by .....
Jaime Peraire
Professor of Aeronautics and Astronautics
Chair, Committee on Graduate Students

Modeling of Hall thruster lifetime and erosion mechanisms

by

Shannon Yun-Ming Cheng

Submitted to the Department of Aeronautics and Astronautics
on 25 May 2007, in partial fulfillment of the
requirements for the degree of
Doctor of Philosophy in Space Propulsion

Abstract

Hall thrusters and other types of electric propulsion have become a tempting alternative to traditional chemical propulsion systems for in-space applications due to the high specific impulses (I_{sp}) they provide. Large I_{sp} translates to a highly desirable mass savings and system trades show that Hall thrusters fall in an optimum operation regime well suited for missions such as station-keeping and orbit transfers. However, uncertainty about thruster lifetime has impeded the device's widespread integration as mission designers want a propulsion system guaranteed to last the entire mission duration. Furthermore, recent interest in applying the technology to more complex propulsion tasks has suggested that throttle-capable thrusters will become desirable and concern about the effect of operating condition on thruster longevity has been raised.

To aid in early design stages and later thruster qualification, development of a computational life-prediction tool is needed since experimental lifetime testing is prohibitively expensive and time-consuming. In this work, an axisymmetric hybrid-PIC model, *HPHall*, has been upgraded to simulate the erosion of the Hall thruster acceleration channel, the degradation of which is the main life-limiting factor of the propulsion system. Evolution of the thruster geometry as a result of material removal due to sputtering is modeled by calculating wall erosion rates, stepping the grid boundary by a chosen time step and altering the computational mesh between simulation runs.

The code is first tuned to predict the nose cone erosion of a 200W Busek Hall thruster, the BHT-200. Simulated erosion profiles from the first 500 hours of operation compare favorably to experimental data. The thruster is then subjected to a virtual life test that predicts a lifetime of 1,330 hours, well within the empirically determined range of 1,287-1,519 hours. The model is then applied to the BHT-600, a higher power thruster, to reproduce wear of its exit ring configuration over 932 hours of firing. Better understanding of the physics of anomalous plasma transport and low-energy sputtering are identified as the most pressing needs for improved lifetime models.

Thesis Supervisor: Manuel Martinez-Sanchez
Title: Professor of Aeronautics and Astronautics

Acknowledgments

The path followed in pursuing this PhD has been anything but straightforward and there are many people I would like to thank who have helped me along the way.

First, a huge thanks to my advisor, Professor Manuel Martinez-Sanchez. His genuine curiosity about how the world works and his open door are what makes him a great mentor. I am also grateful for the freedom he gave me to explore and satisfy my own intellectual curiosity, even when it didn't apply directly to my research. The immense respect I have for him is what made me decide to stay on.

The rest of my committee, Professor Jaime Peraire and Dr. Oleg Batishchev, have always been supportive and provided helpful feedback throughout my doctorate. Thanks are also in order for my thesis readers, Dr. Mike Fife and Dr. James Szabo, whose outside perspective and comments about my work were greatly appreciated. Special thanks to Mike for originally writing *HPHall*.

Without the help and support of Busek Co. Inc., this work would have never happened. Thanks especially to Bruce Pote and Rachel Tedrake for their guidance in modeling their thrusters. Financial support through the DoD SBIR program made the work possible. The electric propulsion group out at Edwards Air Force Base has consistently been very helpful and fun to work with. For this project, Bill Hargus and Taylor Matlock kept me honest about my computations by providing insight into the experiments used to validate my model.

My family has always been there for me and ready to cheer me through my triumphs, support me through my struggles and help me stand back up after my defeats. Thanks to Dad for knowing what it's like to do a PhD and trying to explain to Mom what it was all about. Thanks to Mom for trying to understand Dad and for being my number one supporter even if it didn't really make sense. Thanks to Serena (Inky) and Adrian (Poctopus) for always reminding me of life outside school. I hope we have time for more adventures now that I'm finally done with this degree.

Doing this PhD would have been miserable without the company of Noah and Yassir. From Team Quals to our successful hood trick, grad school has been full of

laughs and I can't think of a better pair to have gone through the trenches with.

The many students of the SPL and SSL have made the lab a fun environment to work in – I would especially like to thank Mark, Jorge, Kay and Ollie for the hilarity of my first years as a PhD student. And Jorge for all the good talks that have continued even from Germany. Al and Julie have also been fantastic remote supporters, cheering for me from California ever since I started. My final year was brightened by my officemate Dan, who reminded me why I love grad school with his enthusiasm and non-jaded first-year perspective.

During my ProjectX days, it was a privilege to work with the ACDL - thanks especially to Professor Darmofal, Bob Haimes, Krzysztof, Garrett and Todd for adopting me as an unofficial member of their lab and patiently answering all my questions about discontinuous Galerkin. Jean Sofronas made life run more smoothly by helping me schedule all my meetings with Professor Peraire. And thanks to Professor Peraire and the Fall 2006 16.07 Dynamics class for giving me the chance to TA. Everyone was fun to work with and I hope I was able to teach a fraction of what I learned from all of you.

Raffi, Jessica and Ethan have shared the ups and downs of both school and life with me since our undergrad days. Thanks. Finally, Ethan, for being there, helping me learn about myself and others as well as giving me confidence to face the world by believing in me.

Contents

List of Figures

List of Tables

Chapter 1

Introduction

This thesis investigates the lifetime and erosion mechanisms of Hall thrusters through computational modeling. In this introduction, chemical and electric propulsion as well as the regimes each are well-suited for are discussed. Following is a description of the Hall thruster and its operation. Then, motivation for studying the thruster erosion is given. Finally, an outline is provided for the rest of the thesis.

1.1 Chemical vs. electric propulsion

Chemical and electric propulsion (EP) both serve important purposes in the arsenal of a space mission designer. Chemical thrusters are characterized by a high thrust-to-mass ratio (F/M), but a low specific impulse, meaning a small acceleration for the amount of propellant mass expelled. The reason for this property is the limiting of a chemical rocket's exit velocity by the propellant's finite internal energy, which is released during combustion. In contrast, electric thrusters typically have a low thrust-to-mass ratio, coupled with a high specific impulse. Since EP devices use an external power source to accelerate the propellant, no inherent limitation on the working fluid's internal energy exists and higher specific impulses are achieved. However, given current technology, when the mass of the power source and associated power-processing unit is added to the total system mass, the low F/M appears.

Chemical propulsion is necessary for missions requiring high thrust. For some,

such as planetary takeoff or landing, a large force is required. In other cases, the goal is to conserve time, as for rapid maneuvering or fast plane change. On the other hand, electric propulsion is well-suited for missions requiring high specific impulse. Generally, these tasks seek to conserve mass, examples being deep space missions or long-term formation flight and drag cancellation. In addition, there are missions that fall into a grey area where it is up to the discretion of the mission designer to choose a system – usually, the decision involves a trade between time and mass. An oft-used analogy equates chemical propulsion with a sports car in that a destination is achieved quickly, but with small payload. Conversely, electric propulsion is similar to a truck – the destination is approached slowly, but the mass savings allows a larger payload [55].

Further reasoning for the case of EP can be seen if one considers that the mission cost scales roughly with the initial launch mass, M_o,

$$Mission\ Cost \approx M_o = \underbrace{\left(\frac{M_o}{M_{to\ orbit}}\right)}_{Booster\ engine} \underbrace{\left(\frac{M_{to\ orbit}}{M_{payload}}\right)}_{Space\ engine} M_{payload}. \tag{1.1}$$

The launch mass is proportional to two mass ratios. One represents the mass ratio dealt with by the booster rocket or that used to launch the spacecraft from Earth. The other represents that dealt with by the space engine or that used once the spacecraft is already in orbit. Both ratios are equally important and it is highly desirable to minimize them, not only to reduce cost, but to maximize payload. In reality, the most flexibility lies in the space engine ratio and it is here where a choice of electric over chemical propulsion could provide great benefit.

1.2 Hall thruster physics

Hall-effect thrusters are a specific type of electric propulsion and are characterized by an annular acceleration channel and a radial magnetic field. Figure 1-1 illustrates a typical engine cross-section. Electrons are emitted by an external cathode and back-stream towards the anode, setting up an axial electric field. Once inside the thruster

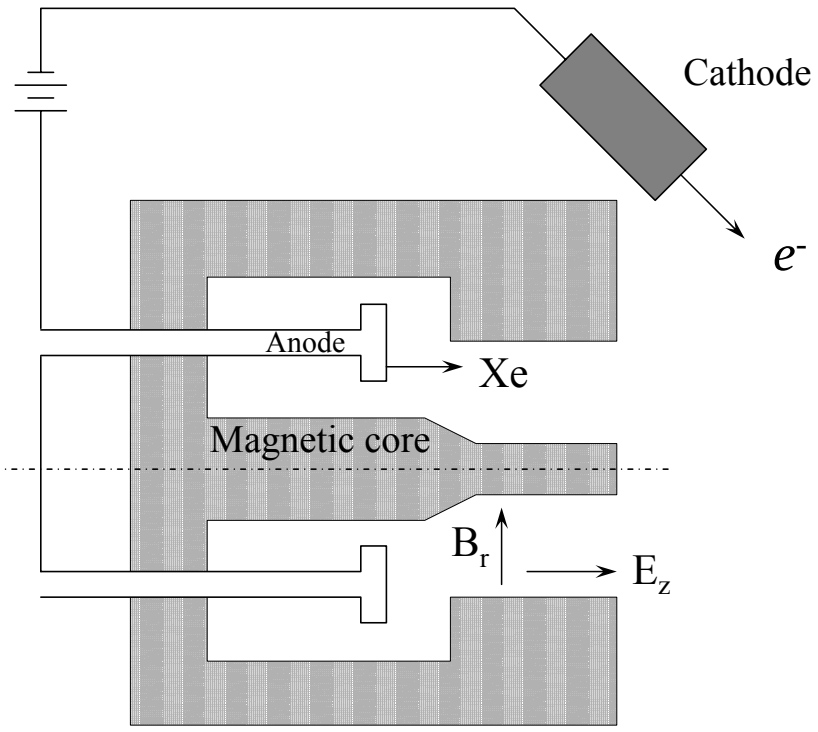

Figure 1-1: Cross-section of typical Hall thruster.

channel, a radial magnetic field is encountered and because of their small Larmor radius and long collision mean free path, electrons are magnetized and effectively captured in azimuthal drifts along field lines, preventing their direct streaming to the anode. Meanwhile, neutral propellant gas, typically xenon, is injected into the channel near the anode and undergoes ionization upon contact with the trapped electrons. The resultant heavy ions have a Larmor radius much larger than the thruster's dimensions and are accelerated out of the channel by the axial electric field with little influence from the magnetic field. This ion beam is neutralized with electrons from the cathode, resulting in equal and opposite electric forces. The mechanism for thrust transmission to the engine structure is via the trapped electrons. Through the azimuthal Hall current they generate, a $\vec{j} \times \vec{B}$ force acts on the thruster magnets, thereby producing thrust.

1.3 Motivation

Traditionally, Hall thrusters have been used for propulsion tasks such as geosynchronous orbit stationkeeping and other low thrust orbit-adjusting maneuvers [54]. These missions have primarily employed the thruster at a single nominal operating point and require electric propulsion lifetimes of 2000-3000 hours [77] which is easily satisfied by thrusters like the SPT-100 with a 7000 hour lifetime. As confidence in the technology builds, mission planners are investigating the feasibility of expanding the use of Hall thrusters to purposes ranging from interplanetary cargo transfer [30, 79] to aerobraking [42]. To succeed at these functions, it may be desirable to throttle the thruster over a range of operating conditions, either varying power or specific impulse. The effect of off-nominal firing on the device's longevity has not been fully characterized, although lifetime is an important design metric that determines the number of thrusters needed for an extended cargo mission or whether the system is a cost-effective propulsion alternative for cost-capped science missions. Oftentimes, life testing done to qualify thrusters focuses on operating at full power in order to maximize propellant throughput in the shortest amount of time possible. However, during the actual mission, this full power mode may not be the primary firing condition and lifetimes could be significantly longer than those predicted by experiment [16]. Clearly it would be prohibitively expensive and time-consuming to experimentally determine the life span of a thruster at every possible operating condition. Thus, the ability to accurately simulate the mechanisms that lead to failure of the thruster as well as how they are affected by differing firing regimes is required from a mission planning standpoint.

Another benefit of a computational model for Hall thruster lifetime and erosion mechanisms is its contribution to the design process. Thruster designers need a tool to foresee how changes in their blueprints affect lifetime as running a life test after each design iteration is costly in both time and resources. Having a predictive capability expedites the process by allowing only promising concepts to reach the materialized phase.

1.4 Outline of thesis

Chapter 2 of the thesis summarizes previous work on comprehending the erosion mechanisms and predicting the lifetime of Hall thrusters. Chapter 3 gives an overview of the sputtering process and reviews current understanding of the phenomenon specific to boron nitride, the ceramic used in construction of the two thrusters considered. A model for the sputtering of boron nitride is then presented. A description of how this model is implemented in a Hall thruster simulation as well as how the code is tailored to forecast lifetime is given in Chapter 4. Chapters 5 and 6 present simulation results for the BHT-200 and BHT-600. Finally, a summary of contributions and suggestions for future work are provided in Chapter 7.

Chapter 2

Prior research

In this chapter, previous research done in the area of Hall thruster lifetime prediction is summarized. This work primarily falls in two categories – experimental measurements to determine thruster lifetime or erosion characteristics and development of models to predict lifetime. Following is a discussion of the modeling efforts and identification of its shortcomings, providing impetus for this research.

2.1 Definition of lifetime

The lifetime of a Hall thruster is mainly limited by the erosion of components protecting its magnetic circuitry from the discharge plasma. Once the magnetic poles are exposed, further degradation or heating may occur, affecting the nominal magnetic field and consequently the thruster's performance. Accordingly, end of life is declared when the dielectric exit rings in stationary plasma thrusters (SPT-type) or the conducting guard rings in thrusters with anode layer (TAL-type) are breached. These two Hall thruster variants and their sensitive components are illustrated in Figure 2-1.

Because the magnetic and electric fields are imperfectly configured, the plasma is not ideally focused, causing channel wall ion impingement and gradual wearing. It is generally accepted that thruster lifetime increases with size [56]. This result can be seen via scaling arguments that show how mass flow rate density reduces as size grows

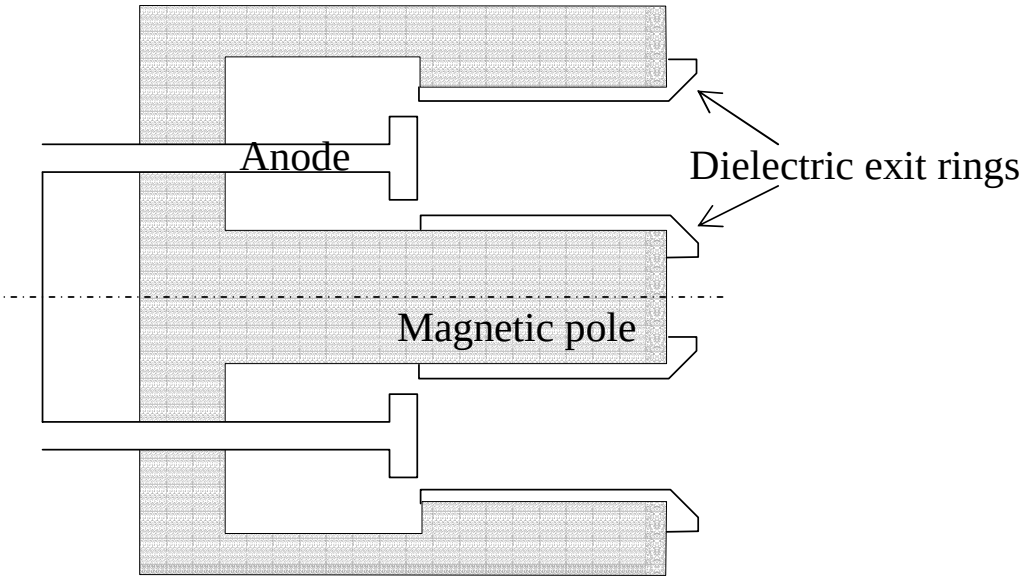

(a) Stationary plasma thruster (SPT).

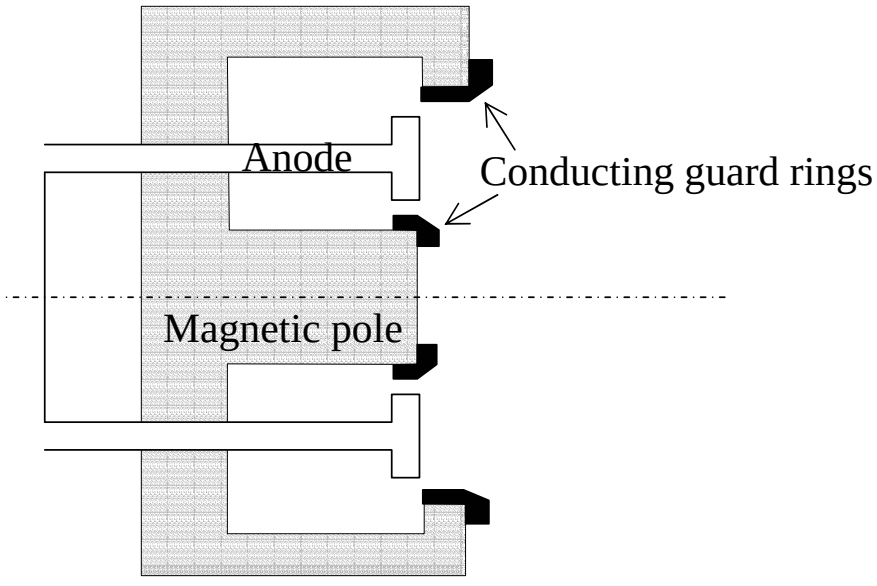

(b) Thruster with anode layer (TAL).

Figure 2-1: Hall thruster types.

Table 2.1: Lifetime of Fakel SPT family – designation number corresponds to thruster diameter in mm [56].

	SPT-35	SPT-50	SPT-70	SPT-100	SPT-140	SPT-200	SPT-280
Power (W)	200	350	670	1350	2700	5400	11000
Lifetime (h)	2500	3500	4900	7000	10000	15000	22000

[15]. Table 2.1 gives lifetimes for the family of Fakel SPT thrusters – the SPT-100 has been empirically life tested and the remaining thruster lifetimes are scaled from this data point.

2.2 Experimental work

Experiments related to thruster longevity have either been long-duration qualification tests that directly determine lifetime or shorter tests intended to characterize erosion behavior and allow extrapolation of lifetime. Table 2.2 summarizes published completed and continuing tests longer than 400 hours. Though performance parameters (thrust, efficiency and specific impulse) may show some variation at the beginning of life, values do not deviate greatly from nominal and tend to stabilize later in life. In many of the life tests, measured erosion profiles show azimuthal asymmetry and may exhibit a periodic structure about the channel circumference. In some cases, this phenomena can be explained by a misaligned channel (in the T-220) or by a non-uniform magnetic field caused by spacing between the electromagnets that creates minimum erosion depths where the radial magnetic field is strongest (in the D-55) [53]. Theories that attribute this anomalous erosion to interaction between the electron dynamics and the channel geometry have been proposed but not verified [8, 58].

In addition to these lengthy tests, shorter experiments have also been performed with the aim of characterizing erosion behavior. Trials using five different grades of boron nitride exit rings in the laboratory model NASA-120M Hall thruster show significant variation in erosion profiles after 200 hours [62]. Similar to a few of the long tests, greater erosion near the cathode is observed as well as less erosion in regions of maximum radial magnetic field. Testing of a D-80 in different operating modes for

Table 2.2: Long-duration Hall thruster lifetime tests.

SPT-type:

Thruster	Time (h)	Agency	Power (W)	I_D (A)	V_D (V)	Performance notes	Erosion notes	Refs
SPT-100	5730	JPL	1350	4.46-4.48	300	- 0-1000 cycles, decrease - 1000-3000 cycles, increase - 3000-6925 cycles, decrease	- outer insulator grooves - inner asymmetric - more erosion near cathode	[32, 34]
SPT-100	7008	Fakel	1350	4.5±0.1	300±2	- 0-200 h, decrease - 600 h, stabilize - 1500+ h, increase/stabilize	- outer insulator grooves - erosion rate decreases by factor of 5 after 1000 h	[6, 7]
T-100	2000	KeRC	1300	4.4±0.05	300±5	- stable throughout	- less erosion of inner wall	[63]
T-220	1000	GRC	10000	20	500	- 2% variation at most	- erosion rate decreases with time - asymmetry due to misaligned channel - higher opposite cathode	[57]
PPS1350	7506	Snecma	1500	4.28	350	- 0-200 h, decrease - 200-400 h, increase - 400-1950 h, decrease/increase - 1950-2500 h, fluctuate - 3500 h, stabilize	- >1200 h, azimuthal variation	[52]
BPT-4000	5800	Aerojet	3000-4500	7.5-15	300-400	- 0-500 h, decrease - 1800-2000 h, thrust stabilizes - 1800-2000 h, I_{sp} increases	- optical measurements of insulator corner from outside tank	[17]
BPT-4000	400	Aerojet	1000-2000	5	varies	- varies with power level	- test continuing	[78]

TAL-type:

Thruster	Time (h)	Agency	Power (W)	I_D (A)	V_D (V)	Performance notes	Erosion notes	Refs
D55	636	JPL	1350	4.47	300	- stable throughout	- accelerated test with stainless steel guard rings - azimuthal periodic structure	[33]
TAL-110	1018	TsNIIMASH	3000	8.6±0.1	350±10	- stable throughout	- first and last test segment: 3x erosion rate	[69]
TAL-110	1000	JPL	3100-3400	9.0-9.5	350±10	- stable throughout	- erosion rate stable	[69]
D80	1200	GRC	2800	4	700	- 2% variation at most	- more erosion near cathode - 600-900 h, magnet exposed, still operates well	[43]

100 hours proves that erosion is highly dependent on firing condition and exhibits a nonlinear relationship between erosion rate and applied voltage [72]. Spectroscopy has also been used to quantify overall erosion rates with a non-intrusive method that does not require interruption of the life test to physically measure a wear profile [11, 20, 76, 86]. In these experiments, the intensity of emission lines from sputtered wall material is used to determine the rate and confirms that erosion depends on operating condition. Finally, the influence of magnetic field topology on the initial upstream location of channel wear is used in conjunction with a numerically simulated wall energy distribution to estimate the sputter threshold of the thruster ceramic [37].

2.3 Lifetime prediction models

Besides work done to empirically quantify lifetime and erosion mechanisms of Hall thrusters, development of predictive lifetime models has also been pursued. The basis of all these models gives the wall recession rate as,

$$\xi = j_{iw} S_v(E_i, \theta_i), \tag{2.1}$$

where j_{iw} is the ion flux to the wall and $S_v(E_i, \theta_i)$ is the volumetric sputtering coefficient which is a function of the target material, the incident ion energy and the ion angle of incidence. Thus, necessary components of any life span forecasting tool are a sputter model for the material in question and a plasma discharge model that gives the wall flux.

2.3.1 Theoretical modeling

Beginning with an expression similar to Equation 2.1, Baranov et. al [9, 64] make the simplification that the volumetric sputtering coefficient only depends on z, the axial coordinate along the thruster channel,

$$\xi = \frac{dr}{dt} = V(z) \left[n(z, r) v(z) \right], \tag{2.2}$$

where V is the averaged volumetric sputtering coefficient, n is the ion density, v is the ion velocity and r is the radial coordinate. Possible expressions for the variation of density across the channel are tried and used to solve for $r(t)$, the wall profile as a function of time. A density dependence of the form,

$$n(r) = n(0)e^{-r/L}, \tag{2.3}$$

where L is a characteristic length is found to be the most realistic. Plugging Equation 2.3 into 2.2,

$$\frac{dr}{dt} = \left.\frac{dr}{dt}\right|_{t=0} e^{-r/L} = Ce^{-r/L}, \tag{2.4}$$

where C is the initial wear velocity. This expression can then be integrated to yield,

$$r(t) = L\ ln\left(1 + \frac{C}{L}t\right), \tag{2.5}$$

giving a logarithmic dependence in time for the lifetime. When considering observations of actual thruster lifetimes that are often characterized by an initial period of great erosion followed by a settling period where the profile reaches a steady-state and wear rates slow, this relationship seems plausible.

2.3.2 Semi-empirical modeling

The goal of a semi-empirical model is to estimate the lifetime of a thruster based on data from minimal experimental testing. The general idea is to run a thruster for a short time, measure the erosion profile and fit it to a formulation for the wall shape that incorporates descriptions of the ion flow and the material sputtering [1]. The main assumptions of this model are that ion flow can be approximated as originating in ray-like fashion from one or two effective centers and that ion energy is purely a function of axial distance along the channel. Solving the model for best-fit parameters to the empirical data then allows calculation of erosion rates and a future wall profile. The thruster is then mechanically processed to advance the wall forward in time and

the entire procedure is repeated until lifetime is determined [10, 46, 50]. The method is quite sensitive to the test duration used to represent the thruster operation. Further study to optimize this variable as well as how far a thruster should be stepped in time is needed.

2.3.3 Computational modeling

A number of approaches to numerically simulating the erosion processes in a Hall thruster and their consequences on lifetime have recently emerged. In 2004, Manzella et al. [51] proposed a lifetime prediction model that attributed the mechanism for wall erosion to scattering collisions, arguing that ions impacting the wall must have been diverted from an otherwise uniform plasma flow along the acceleration channel. Building a 1D model around this theory, decent agreement to erosion profiles of the SPT-100 is achieved, but only when the neutral density is increased by a factor of two. Because scattering collisions alone do not produce enough erosion, the assumption of an ideally-focused axial flow is improbable.

Continuing work on this issue, Yim et al. have expanded on these ideas and developed a 2D fluid model more grounded in physics [83, 84, 85]. The hydrodynamic description models the plasma species with a finite volume flux-splitting method on an axisymmetric Cartesian mesh. To allow for a changing geometry as the walls erode, a cut cell method is used. In addition to a model for the sputter yield, near-wall scattering collisions are included, ion wall fluxes are given a Maxwellian distribution and the Bohm coefficient is varied to affect the potential profile across the channel. Simulation results tend to underpredict erosion at long times and is weakest at capturing the upstream erosion behavior.

The remaining computational modeling has focused on using 2D hybrid-PIC codes to provide the plasma discharge parameters. In a study to determine the effect of different magnetic field configurations on the SPT-100, Garrigues et al. [36] included a sputtering model to analyze the influence on lifetime. The main conclusion of the analysis confirms the fact that erosion damage to thruster walls decreases when more of the plasma's potential drop occurs outside the channel. This result is already

well-understood in the context of TALs which exhibit less erosion than their SPT counterparts due to the acceleration zone being pushed outside the thruster.

Gamero et al. have built upon an existing code, *HPHall* [25, 26], as the foundation of their lifetime prediction capability [31]. Over the course of a simulation run, averaged flux and energy distributions to the channel walls are tracked. During post-processing, these properties are used to generate sputter yields and then erosion rates. Armed with these, the geometry is stepped forward in time and the process is repeated, allowing self-consistent modeling of the geometry evolution. The SPT-100 is used as the test case since erosion profiles over its lifetime are available for direct comparison in the literature [2]. Computational efforts yield results that correctly place the location of channel erosion onset, but overall erosion is underpredicted. Further work on the model is being done to improve neutral injection and electron mobility modeling with the intent of better matching erosion data [41].

Sommier et al. use a simulation based on *HPHall* as its research base [73, 74]. Instead of post-processing with averaged properties, sputtering caused by individual particles crossing the grid boundary is tracked. Neutral sputtering is accounted for, but found to be a factor of 1000 less than that caused by ions. Both charge exchange (CEX) and momentum-exchange ion-neutral collisions are modeled – CEX tends to decrease while momentum-exchange collisions increase erosion. Overall, erosion is decreased by these interactions. The effect of self-induced magnetic fields is also found to have a minimal effect on the simulation results. Both the Stanford Hall Thruster and SPT-100 are subjected to a virtual life test with the model. Erosion profile data for the Stanford Hall Thruster is unavailable, so only comparison to the SPT-100 profiles gives an indication of the success of the code. As with Gamero's model, Sommier's findings underpredict erosion.

2.4 Discussion of previous work

Based on the experimental work that has been done in this area, the need for prediction tools is apparent. Full lifetime tests are expensive, time-consuming and do not

cover the entire range of possible operating conditions. Nevertheless, empirical data are crucial for validating proposed models and should be continued.

Theoretical modeling provides a general and simple picture of the erosion issue, but since it relies on gross assumptions, it is unlikely to give detailed insight into a problem that appears, from the experimental efforts, quite thruster-specific. Addressing this concern are the semi-empirical accelerated wear tests that ground theoretical models with data from short-duration tests. However, this approach still involves destruction of a thruster, which may not be desirable in the early design stages or if cost is a consideration.

Thus, simulations have the greatest potential to provide a resource-efficient solution as a good model should be able to handle a variety of thruster configurations at different operating conditions. Upon reviewing the current numerical work being done, the greatest roadblock seems to be difficulty in acquiring a complete set of key information needed for successful lifetime modeling. Thruster geometry is usually not a problem, whereas magnetic field configuration is more difficult as these designs are generally proprietary. To model the SPT-100, Gamero and Sommier both used a combination of experimental centerline measurements of the field and a magnetic streamline map from Garrigues that represented the typical configuration. When re-gridding to account for erosion of the walls, assumptions had to be made about the field in the newly exposed regions. As the magnetic field plays the fundamental role in Hall thruster plasma dynamics, it is difficult to expect good results if this input is suspect in any way. Another complication is a lack of understanding of material sputtering behavior at low energy. All the computational models discussed use the same experimental sputter yield data of borosil, the SPT-100 channel ceramic, taken by Garnier [35]. However, the data points are taken at higher energies than those typically seen in a Hall thruster and a method for approximating sputter behavior at low energies is necessary. The approaches taken by the modelers range from logarithmic curve fits to using the form of a theoretical model developed for elemental sputtering. These disparities are further highlighted by the inability to converge on the sputter threshold value, E_{th}, the fundamental parameter of these models. Table

Table 2.3: Comparison of borosil sputter thresholds used in computational models.

Model	E_{th} (eV)	Reference
Manzella	50	[51]
Yim	50	[83]
	70	[84]
	50, 60, 70	[85]
Garrigues	30-70	[36]
Gamero	56.9	[31]
Sommier	50	[73, 74]

2.3 illustrates the differences across and sometimes within simulations.

The development of the model in this thesis strives to overcome these obstacles by being as detailed as possible in the definition of thruster-specific parameters. Also, when faced with uncertainty in the physics, an effort is made to base the applied solution on solid theory. Two low-power thrusters developed by Busek Co. Inc., the BHT-200 and the BHT-600, are studied. These thrusters are chosen because a complete set of data needed for lifetime prediction can be compiled. Geometry and magnetic field information are acquired from Busek Co. Inc., sputtering data on the identical grade of channel ceramic have been taken and erosion profiles for simulation comparison are also accessible. Once the model is tuned for one thruster, its applicability to the other thruster is tested to determine if all appropriate physics affecting erosion has been implemented.

Chapter 3

Sputtering

In order to quantify the degradation of Hall thruster lifetime due to erosion of the acceleration channel by the plasma flow, a sputter yield model for the channel material is required. In this chapter, a general overview of sputtering is first presented. As sputtering is a material-dependent property and both thrusters considered in this thesis have ceramic insulators made of boron nitride, the current understanding of boron nitride sputtering is then surveyed. Finally, development of the sputter yield model used in the erosion module is discussed.

3.1 General sputtering overview

Sputtering is the removal of material from a solid surface undergoing particle, usually ion, bombardment. An enormous body of work has been done to characterize sputtering trends under a wide variety of conditions. The excellent review paper by Smentkowski [71] summarizes this extensive literature well. Here, a comprehensive discussion of sputtering will be omitted in favor of selected highlights relevant to the problem at hand.

Sputter yield is the metric used to quantify the sputtering phenomenon and has units of amount of material eroded per incident ion. When an energetic particle strikes a sputterable surface as illustrated in Figure 3-1, energy is transferred to the target via collisions with its atoms.

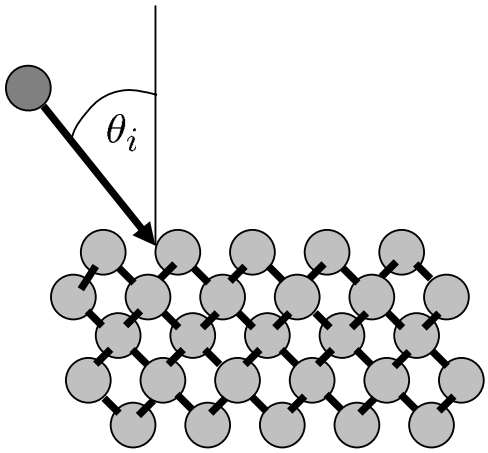

Figure 3-1: Incident particle bombards sputterable solid.

Figure 3-2 depicts mechanisms in which the incident particle's energy can be deposited and cause sputtering at the surface. In Figure 3-2(a), the incoming particle directly knocks out a target atom. Figure 3-2(b) shows the impacted target atom recoiling backwards and ejecting a neighboring atom. As represented in Figure 3-2(c), the linear cascade regime occurs when the bombarding particle initiates a collision cascade through the material – target atoms are then sputtered via secondary recoils. The exact means by which material is sputtered from a surface depends on a variety of factors such as incident species, incident energy, incident angle, surface lattice structure, surface binding energy and surface morphology. The processes these factors lead to can be quite complex and sputtering by all three mechanisms may happen concurrently. Thus the sputter yield is used to describe their net effect.

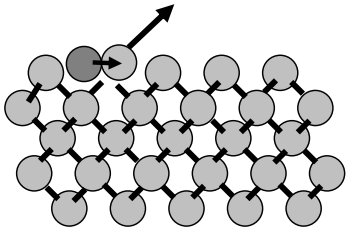

(a) Direct knock-on regime: incident particle sputters target atom directly.

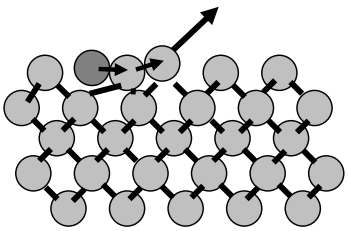

(b) Single recoil regime: incident particle sputters target atom indirectly via backward recoil.

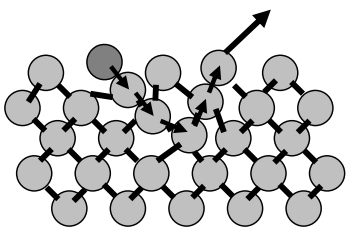

(c) Linear cascade regime: incident particle causes collision cascade, target atom sputtered via secondary recoil.

Figure 3-2: Energy transfer mechanisms during sputtering.

Experimentally measuring accurate sputter yields requires a well-designed method performed under ultra-high vacuum conditions to minimize erroneous readings due to impurity deposition. Additional elements of a successful sputtering test include a stable and well-characterized ion source, measurement of the actual beam current striking the surface and an ability to precisely determine the amount of eroded surface material. A projectile source with a known ion energy distribution and orientation with respect to the sputter target is needed to correlate the yield with incident energy and angle. To measure the true current to the surface, the current generated due to secondary electron emission by the target must be accounted for. Finally, the quantity of material removed by the impinging beam must be found – methods include weighing of the sample before and after exposure to the ion beam, measuring frequency changes of a quartz microbalance oscillation crystal as matter gets deposited on it or direct determination of crater volumes through optical profilometry. Each of these procedures have limitations, but when carefully done, provide reliable yields.

Computational modeling of sputtering has been performed using molecular dynamics and binary collision approximation codes. The general technique of these codes is to predict how much of the incident ion energy gets deposited near the target surface. The distribution of this energy throughout the impact vicinity then determines the resulting energies of atoms near the surface and of atoms that approach the surface due to recoil. Atoms energetic enough to exceed the surface binding energy are sputtered. Using these methods, details of the exact process of how an atom gets sputtered can be studied, as well as the effects of different incident and target species, incident angle and lattice structure.

A survey of the literature shows that the sputtering behavior of elemental materials is well-studied, whereas that of multicomponent materials is less so. Many trends can be identified – following is a summary of those particularly relevant to Hall thruster erosion and comments on their applicability.

- Sputter yield increases with incident energy up to ∼10-100 keV. Beyond these energies, ions penetrate deeper into the material, less energy gets deposited at the surface and the sputter yield decreases. The range of energies of concern in-

side Hall thrusters (<600eV) is well below where the yield begins to exhibit this decline. Thus, for Hall thrusters, higher energies correspond to more sputtering.

- Sputter yield is a function of the incoming particle's incident angle, θ_i, as defined in Figure 3-1. A particle impacting the target directly normal to its surface has a θ_i of 0° while one that just grazes the surface has a θ_i of 90°. It is observed that as θ_i increases from 0°, the sputter yield does as well. This behavior is attributed to the decrease of the particle's penetration depth as the incident angle increases. As a result, more energy is deposited near the surface and the sputter yield is greater. As the incident angle continues to increase, the sputter yield reaches a maximum value at θ_{max}, beyond which it begins to decrease. The exact details of the sputtering scenario determine the value of θ_{max}, but it tends to be in the range of 70-80° and occurs because energy transfer to the surface is no longer as efficient. For grazing angles of incidence, $\theta_i \sim 90°$, sputtering is prevented by the incoming particle being repulsed by the surface atoms. The entire range of possible incident angles is considered in Hall thrusters as the plasma flow is not laminar and the specific geometry of a thruster may not be aligned with the bulk velocity direction.

- The sputter threshold is the energy below which sputtering ceases. Measurement of true sputter thresholds has proven to be difficult as it requires techniques sensitive enough to detect miniscule sputter amounts. The experiments that have been performed in the near-threshold energy regime reveal a concave shape to the sputter yield versus energy curve, suggesting that using linear extrapolation to find the energy threshold from yield data at higher energies is invalid. However, in the absence of concrete data, it can define an upper bound for the sputter threshold and may provide a useful "effective threshold". For Hall thruster lifetime prediction, knowledge of the low-energy sputter behavior is paramount as the majority of ions impacting the walls are near-threshold.

- Sputter yield is affected by the target material temperature and its correlation with the amount of surface damage present. The observed pattern is that

sputter yield decreases as surface damage increases since rough surfaces erode less than smooth ones. At high temperatures (∼30% of the melting point), the sputter yield is large as the surface anneals and rids itself of any accumulated damage. In contrast, at low temperatures, the surface retains its roughness and the sputter yield remains in check. The issue of sputter yield temperature dependence in Hall thrusters deserves closer inspection and will be discussed further in Section 3.2.5 – correctly predicting erosion profiles relies on properly determining where along the sputter yield versus temperature curve one lies.

- In multicomponent samples, given similar binding energies, preferential sputtering of the component closest in weight to the projectile is detected. In general, the sputter rate of each component goes as the inverse of its binding energy and mass. Although multicomponent materials have been shown to possess these tendencies, exhaustive study of the intricacies of their behavior has not been performed and further work is required. For Hall thrusters with ceramic insulators, the specific material used should be identified and studied.

3.2 Boron nitride sputtering

The two main types of Hall thruster are distinguished by the wall material that comes in contact with the plasma. Stationary plasma thrusters (SPT) generally have long acceleration channels constructed out of insulating ceramics, while thrusters with anode layer (TAL) have short channels built out of conducting metals. Different ceramics have been tested and used in SPT-type thrusters. In this thesis, the two thrusters considered both have high-purity boron nitride (BN) lining their acceleration channels. Boron nitride is an attractive choice for insulation of the magnet poles due to its mechanical strength and thermal shock resistance. In comparison to other insulator materials, BN also exhibits lower erosion rates. As mentioned earlier, sputtering of multicomponent materials is not well-understood and further study is required to fully characterize the phenomenon – a review of current work on BN sputtering follows.

3.2.1 Normal sputter yield

Few experimental data have been taken on the absolute sputter yield of BN by xenon ions, especially in the energy ranges that concern Hall thrusters. Typical Hall thrusters operate at a 300 V discharge voltage, leading to single ions having a maximum energy of ∼300 eV. Most ions will be born along the latter part of the potential gradient and will be well below this upper bound. Double ions, composing a small percent of the plasma, would acquire approximately twice the energy of a single ion. Published data [1, 22, 35, 80] for low-energy (<600 eV) BN sputter yield are displayed in Figure 3-3 – all measurements are taken using weight loss methods. The ion source used in Abgaryan et al.'s experiment is a SPT and sputter yields are related to the thruster's average distribution energy – thus, the data provide good estimates of the yield, but may not be completely accurate. Abgaryan et al., Garnier et al. and Yalin et al. report their yields in units of mm^3/C while Elovikov et al. use atoms/ion. To compare their results in Figure 3-3, Elovikov et al.'s results are converted into units of mm^3/C. Since densities for the two types of BN studied are not reported, values found in other references are used to perform the conversion. A density of 2.28 g/cm^3 is used for hexagonal boron nitride (h-BN) [13] and 2.26 g/cm^3

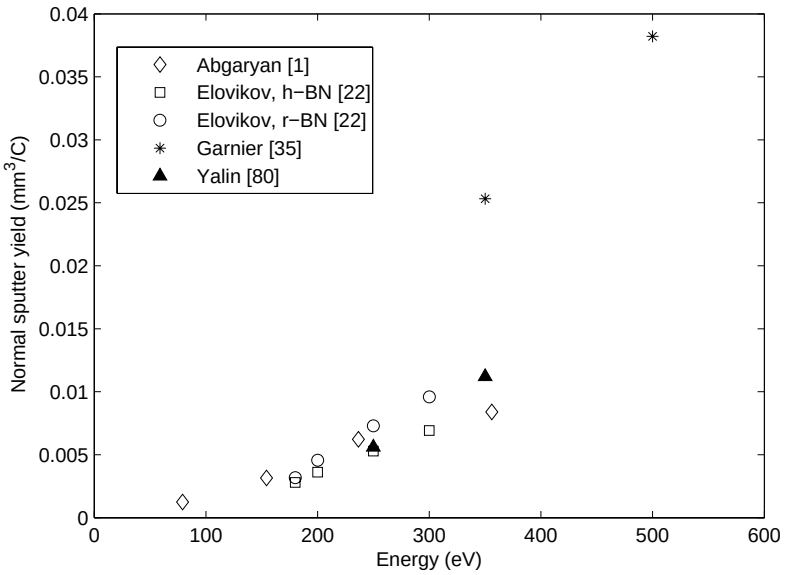

Figure 3-3: Sputter yield of BN bombarded by Xe^+ at normal incidence.

for rhombohedral boron nitride (r-BN) [49]. Furthermore, the molecular weight of boron nitride is taken to be 24.82 g/mol and ions causing the sputtering are assumed to be singly charged. The Abgaryan, Elovikov and Yalin data compare well to each other in magnitude, while the Garnier data are approximately two times greater. Elovikov's results show r-BN having slightly higher sputter yields than h-BN – in a 1994 paper [21], the author explains how the crystal structure of h-BN results in fewer collisions between ions and target atoms than in r-BN. Hence, h-BN sputters less than r-BN. The boron nitride used in Yalin's tests is HBC grade BN from GE Advanced Ceramics with a density of 1.98 g/cm^3 and a hexagonal crystal structure. Garnier and Abgaryan do not specify details about the BN sample used in their experiments, except that it is obtained by pyrolysis. It appears that specifics of lattice structure and boron nitride grade play a role in the material's sputter yield – such properties should be taken into consideration when developing a sputter yield model.

In conjunction with experiments, efforts at simulating the sputtering process are pursued to predict sputter yields. In these models, the key input parameter is the surface binding energy (SBE) of the target surface, which represents the energy barrier a target atom must overcome to leave the surface. As shown by Chen et al. [13], sputter yield results are quite sensitive to changes in the SBE used in TRIM (a binary collision approximation code) calculations. Thus, the general procedure is to adjust the SBE value until good agreement with experimental data is achieved. In surveying the literature, a wide range of values is chosen. For TRIM calculations of Ar^+ and N_2 sputtering h-BN, Reinke et al. [67] use 3 eV as the SBE of both boron and nitrogen. Chen et al. also use 3 eV for B and N in their TRIM calculations of Ar^+ and N^+ bombardment of both c-BN and h-BN. However, Elovikov et al. [22] use 8.1 eV when employing a molecular dynamics model to match their experimental data of h-BN and r-BN being sputtered by Xe^+. Also at the high end, Promokhov et al. [65] use 10 eV in their molecular dynamics simulation of Ar^+ impacting wurtzite BN. Using results from the modeling to predict sputter yields at the lower energies that experiments cannot capture is desirable. However, given that consensus on the most important simulation parameter cannot be reached, it is questionable if these models can be

trusted to be reliable.

3.2.2 Angular sputter yield

Both Garnier and Yalin explore the angular dependence of the sputter yield at low energies. Elovikov only reports sputter yields at one oblique angle (θ_i=45°) and at high energy (>1 keV). Abgaryan has plots of angular sputter yields at different energies, but does not specify the material they are for. Figure 3-4 summarizes Garnier and Yalin's data. Again, Garnier's data are higher in magnitude than Yalin's, but both generally increase in yield from normal incidence until $\theta_i \sim 60 - 70°$ and then begin to decrease. Garnier comments that the incident angle dependence of the sputter yield is weaker in the ceramics tested than is observed in a control case of a standard coverglass. The author conjectures that this effect is explained by the comparatively higher surface roughness of ceramics over the amorphous glass. Simulations of angular sputtering yields are also performed and have the same shortcoming as discussed in the previous section.

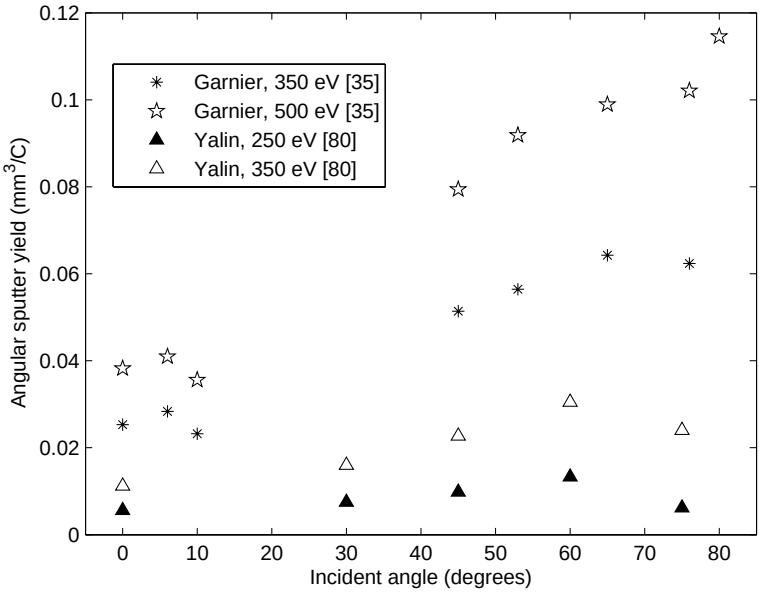

Figure 3-4: Angular yield of BN sputtered by Xe^+.

3.2.3 Outgoing sputter distributions

In addition to the absolute amount of material being ejected from the surface, details of the emission products and their properties have also been investigated. Zhang et al. [87] investigate the sputter products of Xe^+ bombarding BN at an incident angle of 50° using secondary ion (SIMS) and secondary neutral (SNMS) mass spectrometry. Although bombarding ion energies down to 10 eV are tested, sputter products are not detected below 100 eV by SIMS and 300 eV by SNMS. When operated in the p-SIMS regime, it is found that B^+ dominates the positive ion sputter yield, followed by B_2^+, $(^{11}B+^{10}B)^+$ and BN^+. The n-SIMS spectrum exhibits, in order of their abundance, BN^-, B^- and B_2^-. It is noted that neither positive nor negative ions of N are observed, though both B and N do show up in the SNMS spectra. Spectrometry measurements are performed independently of one another and do not provide ratios between different charge state species. Using the same experimental setup, Shutthanandan et al. [70] look into distinguishing the isotopes of boron ions that are emitted during sputtering. Heavy isotope ($^{11}B^+$) enrichment is seen at low energies – however, as incident ion energy increases beyond 350 eV, the sputtered flux becomes light isotope ($^{10}B^+$) enriched. Initially, this result seems counterintuitive as one expects the lighter isotope to be preferentially sputtered at all energies. It turns out that if the incident ion mass is much greater than the target atom mass, as is the case with xenon ions hitting boron nitride, heavy isotope enrichment is expected at low energies. This situation arises since the massive bombarding ion will not penetrate as far into the surface at low energies and the sputter mechanism pictured in Figure 3-2(a) or 3-2(b) is more likely. In these cases, since fewer collisions are involved, energy randomization is not completely achieved and due to their collison cross-sections it is more probable that ^{11}B atoms receive more energy than ^{10}B atoms, as reflected in the greater $^{11}B^+$ secondary ion flux. In contrast, if a lighter ion such as Ar^+ is the incident species, deeper penetration into the crystal lattice happens and the sputter mechanism depicted in Figure 3-2(c) is predominant. During a collision cascade, energy transfer to lighter atoms is preferred and a $^{10}B^+$-enriched emission is attained. This hypothesis is

supported by experiments performed by Franke et al. [29] in which energy spectra of ejected B as a result of argon ions sputtering boron nitride exhibit a distribution that points to linear collision cascades as the dominant sputter mechanism. As energy is increased with the heavy incident species, this behavior also becomes characteristic as the projectile implants itself further and we observe the resulting crossover from heavy to light isotope enrichment.

Simulations [21, 22, 65] predict that in general, B, the lighter component, is preferentially sputtered. Promokhov et al. observe that at low energies and oblique ion incidence, the heavier component, N, could erode initially instead. The reasoning for this effect is similar to that above – at grazing angles and small energies, initiation of collision cascades is difficult and the heavy species is sputtered first. However, the only experimental look at post-sputtering surface composition done by Garnier et al. sees little variation between the BN sample before and after exposure.

Spatial distributions of sputtered particles are also investigated by Franke et al. – experimental observations are made for 15° and 30° incidence and compared to TRIM calculations. Promokhov et al. use their model to compute the angle distribution of material sputtered off the (0001) face of BN under normal Ar^+ incidence. In work looking at the dependence on mass of nitride sputtering, Elovikov et al. [23] model the mean energies and energy spectra of the outgoing sputter products as well as the depth beneath the surface and mechanisms from which the sputtered particles originate. Mosunov et al. [59] use molecular dynamics modeling of Ar^+ sputtering different BN crystal structures to discover that the outgoing spatial distribution of sputtered atoms is controlled by scattering off of neighboring surface atoms. For graphite-like boron nitride (h-BN or r-BN), only the first surface layer affects the sputter patterns, whereas for diamond-like boron nitride (c-BN), patterns are also sensitive to second layer atom configuration. Though this initial work shows promise, the outgoing angular distributions of sputtered BN are far from fully characterized.

3.2.4 Sputter mechanisms

Simulations have also been used to study the detailed mechanisms by which sputtered particles are created. Mosunov et al. look at sputtering of BN crystal structures at both normal incidence and at an oblique angle ($\theta_i = 75°$). Although normally incident particles penetrate deeper into the target surface, the collision cascades that they generate are shallower than those of their oblique counterparts that penetrate less deeply, but are more capable of producing energetic recoils. Thus, the depth of origin of sputtered particles caused by normal incidence projectiles is smaller than those caused by oblique ones. Furthermore, differences in surface channeling between graphite-like and diamond-like crystals show that since more channeling is allowed by a graphite-like structure, impinging particles can travel further along the surface, thereby increasing the probability of surface atom sputtering. It should be noted that these findings are for the case of Ar^+ bombarding boron nitride. Elovikov et al. [23] study the sputter mechanisms for varying incident ion masses. Though only normal incidence is considered, one observes differences in behavior of depth of origin as a function of incident energy between lighter mass (Ar, 39.948 amu) and heavier mass (Xe, 131.29 amu) ions. Further study is required before applying conclusions from one projectile-target combination to another.

Another property that deserves mention is surface roughness and its effect on sputter mechanisms. As mentioned in Section 3.2.2, surface roughness may have a role in the weakened dependence of the sputter yield of a ceramic on incident angle. Garnier et al. perform further surface analyses of sputtered samples and conclude that irregularities in surface morphology mean that the macroscopic sputter yield is actually a convolution of microscopic sputter yields off of the material's various exterior facets. Smoothing of the surface is not noticed after sputtering, so surface roughness is a concern throughout the process. These observations are backed up by Franke et al., who measured the sputter yield of titanium by argon ions to be less than that of boron nitride, converse to what would be expected by theory based on reduced masses. Upon further investigation using scanning electron microscopy and Laue X-

ray diffractometry, it is found that the Ti target has a very strong surface roughness and coarse crystal structure as opposed to the BN target with a smoother surface and finer polycrystalline microstructure. Hence, it appears the surface roughness of Ti contributes to its lower-than-expected sputter yield. Khartov et al. observe an increase in ceramic micro-structure over 44 hours of a SPT-70 operating [45], further suggesting the effect's relevance in Hall thrusters.

3.2.5 Sputter yield temperature dependence

The temperature dependence of the boron nitride sputter yield has not been measured. The effect of temperature on the sputter yield of borosil (BGP), or $BNSiO_2$, the ceramic used in the construction of the Russian SPT thrusters is illustrated in Figure 3-5 [66]. The sharp increase in sputter yields past 600°C is of great concern to the issue of Hall thruster lifetime – depending where on the curve one lies, erosion could be a factor of two or three higher.

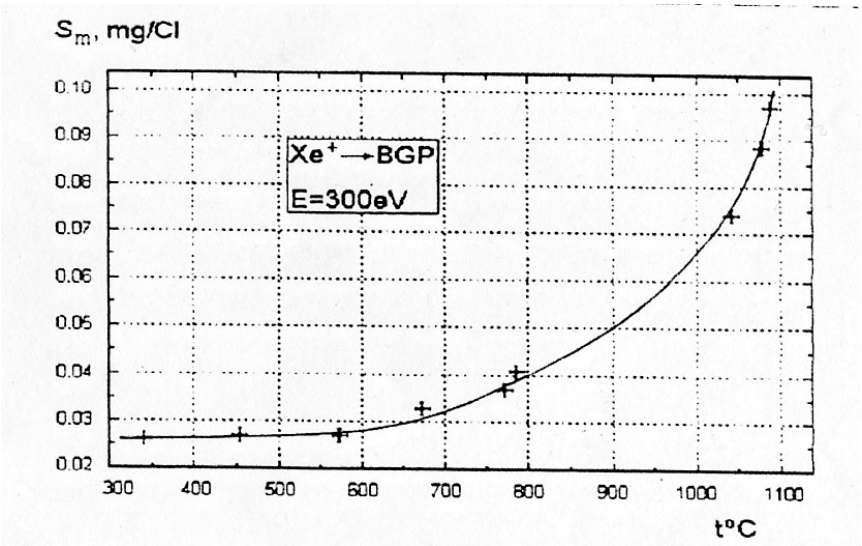

Figure 3-5: Temperature dependence of borosil (BGP) sputtered by Xe^+ [66].

Although this behavior has not been investigated for BN specifically, it has been observed and studied in other materials. In his review, Smentkowski notes that as ion fluences of Ar, Ne and Xe to Ru(0001) increase, the sputter yield decreases. The author explains that the damage induced on a surface by sputtering acts to sup-

press the obtained yields. When a damaged target is annealed at high temperature, this damage is effectively removed and sputter yields return to normal levels. If the temperature of a material during sputtering is high enough, the sample could be continuously annealed and the decrease in sputter yield would not be observed. However, this theory does not seem to explain the exponential increase depicted in Figure 3-5. In a series of papers, Doerner et al. [18, 19, 68] discuss possible hypotheses for the phenomenon. The authors first note weaknesses in the currently accepted description of surface erosion as given by,

$$\textit{Total erosion rate} \;=\; \textit{Physical sputtering rate} \;+\; \textit{Sublimation rate},$$

which states the total erosion has contributions from material that is physically sputtered and from material that is directly sublimated. Physical sputtering depends only on incident particle flux and not surface temperature, while sublimation is independent of particle flux and hinges solely on surface temperature. Given this picture, one expects a constant erosion rate at low temperatures, where physical sputtering dominates. At high enough temperatures, when sublimation and physical sputtering rates become similar, one expects a sharp increase in the total rate with temperature, as sublimation overcomes physical sputtering. However, neither of these mechanisms explains the sudden increase in erosion rate at temperatures well below the sublimation level. For reference, the sublimation temperature of boron nitride and borosil is $\sim$3000 K, while the increase in Figure 3-5 begins around 900 K. Therefore, it seems an additional mechanism is needed to fully describe the total erosion.

Using experimental data of Be exposed to a He plasma, Doerner et al. test two theories that provide a sputtering mechanism that depends on both incident particle flux and surface temperature. The first explanation, radiation activated adatom sublimation (RAAS), is pictured in Figure 3-6. In this model, the bombardment of a target surface by energetic particles not only causes direct sputtering of atoms, but also induces the creation of surface adatoms. An adatom is an atom that gains enough

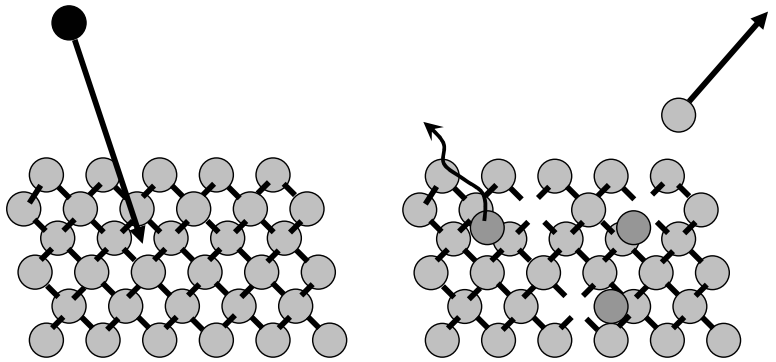

(a) Surface lattice bombarded by energetic particles.

(b) Surface adatoms with reduced binding energy created.

Figure 3-6: Radiation activated adatom sublimation (RAAS) model.

energy from the slowing of an incident particle to become free of its lattice, but does not have enough energy to fully escape the surface via sputtering. Generation of adatoms results in surface vacancies – some are quickly filled as adatoms recombine with the surface, while others are left empty as the associated adatom diffuses away from the site. These adatoms will move across the surface until they encounter another recombination site, or, if the surface temperature is sufficiently high, they sublimate from the surface. Because it is no longer constrained by the lattice, an adatom will sublimate at a lower temperature than the bound surface atoms. Thus, one sees an increase in sputtering beyond the temperature at which unbound adatoms sublimate. The dependence on incident particle flux comes about since higher flux means a larger supply of adatoms available for sublimation.

Figure 3-7 illustrates the inclusion model, an alternative interpretation of the temperature-dependent behavior. As before, bombardment of a target surface results in direct sputtering of atoms. In addition, the energetic particles are embedded within the target crystal lattice and cause shielding and distortion of the structure, effectively reducing the binding energy of neighboring surface atoms. These atoms are more loosely held and subject to sublimation at lower surface temperatures. The greater the incident flux, the greater the number of implanted particles causing weakening of the lattice structure.

Analytical expressions for both theories are developed and molecular dynamics

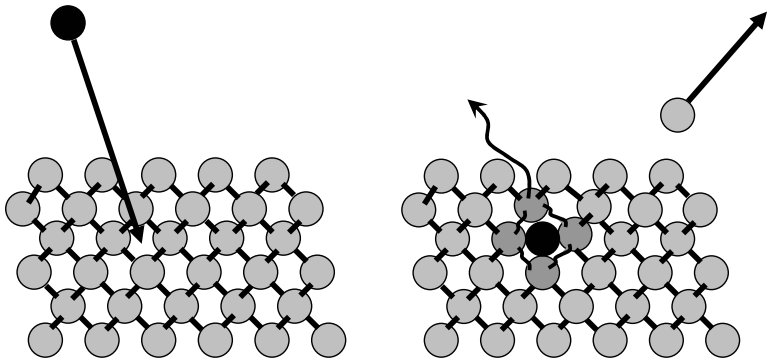

(a) Surface lattice bombarded by energetic particles.

(b) Embedded particles distort lattice, reduce binding energy.

Figure 3-7: Inclusion model.

(MD) simulations are used to calculate model parameters. The number of free parameters in the adatom model is reduced to one, δ_{Def}, the areal defect density, while all parameters for the inclusion model can be found with MD-calculations. Having no free parameters, the inclusion model is directly compared to the experimental data and provides good agreement. However, it turns out the required value of δ_{Def} that results in the best fit of the adatom model to the data is much smaller than what would be considered realistic. The authors conclude the inclusion model best describes the sputter yield temperature dependence, but also concede that further validation with other projectile-target combinations is needed. Evidence of Xe in the near-surface layers of the ceramic isolator of a SPT-70 after 40 hours of operation [44] lends credibility to the physical feasibility of the theory.

3.3 Sputter yield model

Having reviewed the current state of understanding of boron nitride sputtering, a sputter yield model is now developed for use in Hall thruster lifetime prediction. Several simplifying assumptions are made due to the limited available relevant data. As detailed knowledge of preferential sputtering of boron versus nitrogen and its effect on the sputter yield is missing, BN will be treated as a single-component material in the analysis. Next, consideration of surface temperature for the thrusters simulated is

not given. Thermal measurements of the BHT-200 nose cone during operation give the temperature as $\sim 400°C$ [40]. If BN and BGP sputter yields have similar correlation to temperature, the thruster operating condition is safely below the critical level where temperature needs to be accounted for. It should be noted that as thrusters are pushed to higher operating voltages, this supposition should be reexamined as the region of drastic sputter yield increases could be reached.

3.3.1 Normal yield model

Unfortunately, the available experimental data on boron nitride sputter yields do not completely address the low-energy behavior, as the majority of ions in a Hall thruster will lie in this near-threshold regime. The approach then is to use an analytical model and rely on the experimental data for calibration. As mentioned in Section 3.2.1 and seen in testing by Peterson et al. [62], specific properties of the boron nitride tested affect the sputter yield. As such, in developing the sputter yield model, only the Yalin et al. data [80] are used since the BN grade experimented on is identical to that utilized in construction of both the BHT-200 and the BHT-600. The model adapted for use is that of Yamamura et al. [82] who give a theory-based analytical formula that has been empirically tested against available data and is valid for any ion-target combination, though only monatomic targets are included. Following the outlined procedure, the normal sputter yields for boron and nitrogen are calculated and presented in Figure 3-8. For comparison, Yalin's data as well as the average of the Yamamura-predicted B and N yields are also plotted. Although the analytical formula underpredicts the experimental sputter yield, the results are on the same order of magnitude and show reasonable agreement considering the formula is calibrated to monatomic solids.

The form of Yamamura's formula for normal sputter yield, Y_n, is,

$$Y_n(E) = 0.042 \frac{Q(Z_2)\alpha^*(M_2/M_1)}{U_s} \frac{S_n(E)}{1 + \Gamma k_e \epsilon^{0.3}} \left[1 - \sqrt{\frac{E_{th}}{E}}\right]^{2.5}, \tag{3.1}$$

where E is the energy in eV, E_{th} is the threshold energy in eV and $Q(Z_2)$, $\alpha^*(M_2/M_1)$,

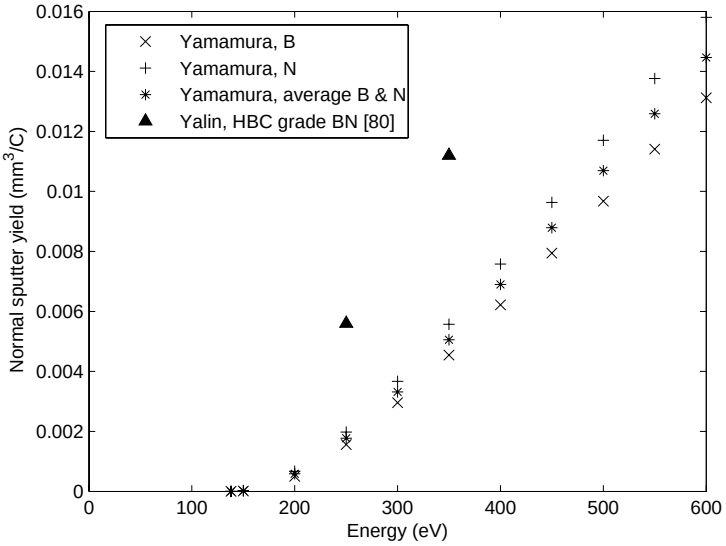

Figure 3-8: Comparison of $Xe^+ \rightarrow$ BN analytical and experimental normal sputter yields.

U_s, Γ and k_e are constants of the projectile-target combination. ϵ is the reduced energy and is linear in E for a given projectile-target combination. $S_n(E)$ has an energy dependence defined by an analytical expression based on the Thomas-Fermi potential,

$$s_n^{TF}(\epsilon) = \frac{3.441\sqrt{\epsilon}\, ln(\epsilon + 2.718)}{1 + 6.355\sqrt{\epsilon} + \epsilon(6.882\sqrt{\epsilon} - 1.708)} \,. \tag{3.2}$$

Because the constants determined by the projectile-target combination are not known for the BN ceramic, it is desirable to find a fit that incorporates parameters that represent these unknowns. For small values of ϵ, Equation 3.2 scales $\sim \sqrt{\epsilon}$. Thus, a fit of the form,

$$Y_n(E) = \frac{AE^{0.5}}{1 + BE^{0.3}} \left(1 - \sqrt{\frac{E_{th}}{E}}\right)^{2.5}, \tag{3.3}$$

is proposed, where A and B are fitting parameters. To test its validity, the approximation is compared to the full expression for boron and nitrogen, since all parameters needed to evaluate Equation 3.1 are known. These comparisons are given in Figure 3-9 – only the range of low energies relevant to the problem is considered. It is ap-

Table 3.1: Calculated parameters for normal yield approximation.

	A	B	E_{th}
Boron	0.069368	1.50312×10^{-10}	137.62
Nitrogen	0.027407	7.74653×10^{-11}	134.66

parent that the fit as given in Equation 3.3 does not agree well with the Yamamura model curve since the energy dependence of Equation 3.2 is not adequately captured. However, if the fit exponent is changed to a value of 0.474, excellent matching is achieved for both elements. Thus, the revised fit,

$$Y_n(E) = \frac{AE^{0.474}}{1 + BE^{0.3}} \left(1 - \sqrt{\frac{E_{th}}{E}}\right)^{2.5}, \tag{3.4}$$

is used. Table 3.1 gives the values of A, B and E_{th} for boron and nitrogen.

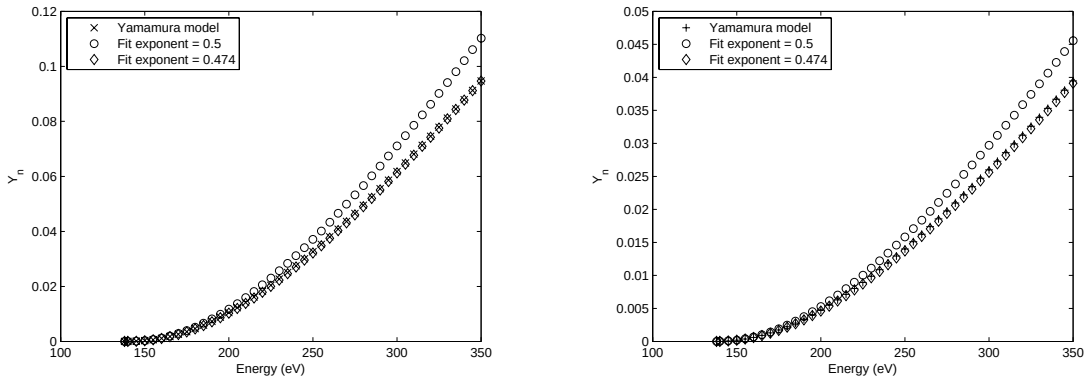

(a) Boron.

(b) Nitrogen.

Figure 3-9: Comparison of Yamamura model to Equation 3.3 and 3.4 approximations.

Using Yalin's boron nitride data, best-fit values of A and B are found for several energy thresholds. These values are given in Table 3.2. Figure 3-10(a) plots the yield fit corresponding to a 30 eV energy threshold and Figure 3-10(b) shows the fits for a range of threshold energies in the near-threshold region. All of the curves pass through Yalin's experimental data points at higher energies. It is apparent that selection of E_{th} is quite important as it can shift the yield curve a significant amount. Since the threshold energy of boron nitride is not known, choice of the appropriate E_{th} will be one of the goals of the modeling.

Table 3.2: Fitted parameters for $Xe^{+}\rightarrow$ BN normal yield approximation.

E_{th} (eV)	A	B
0	0.0000835484	-0.151824
10	0.000164433	-0.146887
20	0.000233999	-0.143251
30	0.000320828	-0.139106
40	0.000436831	-0.133966
50	0.000600157	-0.12718

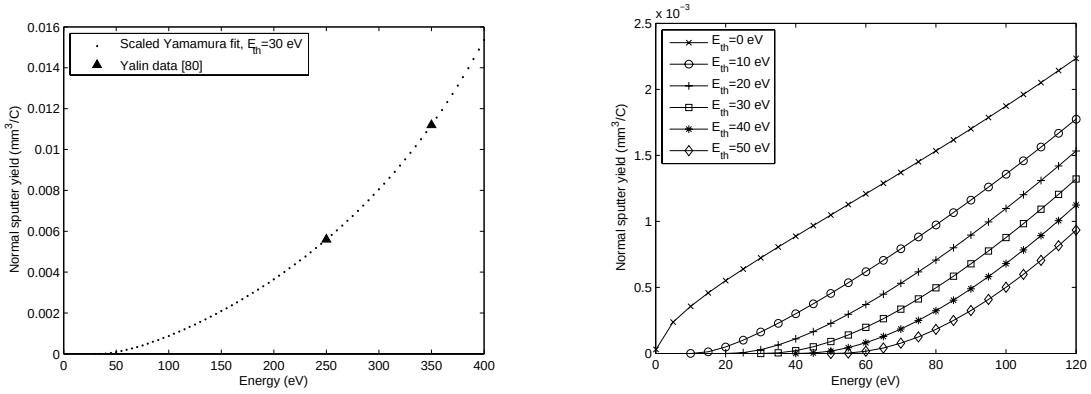

(a) Yield fit for E_{th}=30 eV.

(b) Near-threshold region yield fits.

Figure 3-10: Yamamura-based normal sputter yield model.

3.3.2 Angular yield model

The angular dependence of the sputter yield is also based on a Yamamura empirical formula [81]. For the case of heavy-ion sputtering, the angular yield has the form,

$$Y_\theta(Y_n, E, \theta_i) = Y_n * cos^{-F}(\theta_i) * e^G, \tag{3.5}$$

where Y_n is the normal yield, E is the incident energy in eV, θ is the incident angle and F and G are given by,

$$F = -f\left(1 + 2.5\frac{aE^{-1/2}}{1 - aE^{-1/2}}\right),$$

$$G = -\Sigma\left(\frac{1}{cos(\theta_i)} - 1\right),$$

where f, a and Σ are fitting parameters that are tabulated in Table 3.3. Figure 3-11

shows the angular yield fits plotted against the experimental data for 250 and 350 eV.

Table 3.3: Fitting parameters for $Xe^{+}\rightarrow$ BN angular sputter yield formula.

f	5.97563
a	-3.63786
Σ	1.41355

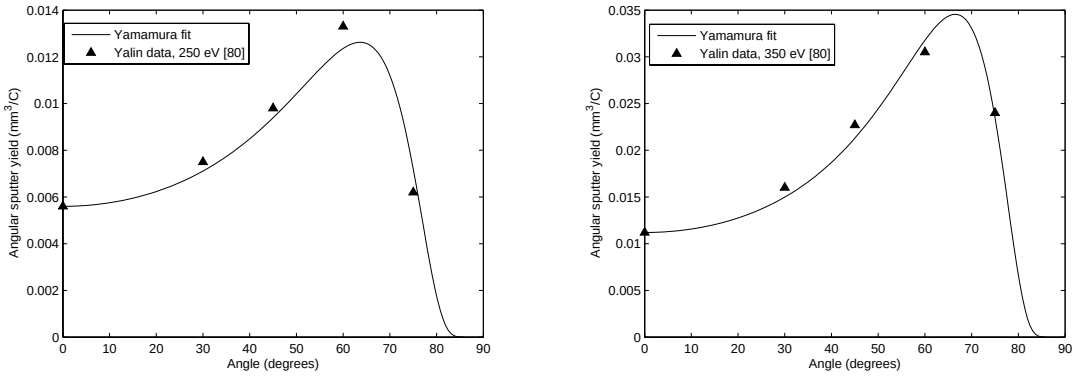

(a) 250 eV.

(b) 350 eV.

Figure 3-11: Yamamura-based angular sputter yield model.

Chapter 4

Computational method

Building on an existing well-proven Hall thruster simulation, the approach taken for lifetime prediction is to develop an erosion model within *HPHall*. In this chapter, a brief description of the *HPHall* simulation is provided. Then, improvements made to allow for erosion modeling are detailed.

4.1 *HPHall*

Originally developed by Fife [25, 26], *HPHall* is an axisymmetric hybrid-Particle-In-Cell (PIC) simulation that models the interior plasma of a Hall thruster. Because of its exhibited robustness and success, the model has remained at the forefront of Hall thruster numerical work and many groups have since developed similar codes [24, 38, 47]. Several groups use *HPHall* itself as the starting foundation of their research [3, 31, 60, 75]. Although the code has evolved since its inception, the fundamental structure remains untouched and serves as the basis of this research.

4.1.1 Overview of numerical model

HPHall is an axisymmetric model that simulates the plasma discharge of a Hall thruster between its anode and cathode. The primary inputs are a two-dimensional (2D) mesh of the simulation region as well as the thruster's magnetic field. Since

induced magnetic fields are ignored, this $\vec{B}$ field is considered static. In a balance between detailed physics and heavy computational burden, a hybrid-PIC approach is taken – namely, the heavy ion and neutral species are modeled as discrete particles while the light electrons are represented as a fluid. An assumption of quasineutrality, $n_i = n_e$, links the ion and electron submodels through their densities and further reduces required effort by allowing grid spacings larger than the Debye length. Because the non-neutral wall sheaths are not resolved, an analytic model is imposed at relevant grid boundaries to include their effect.

4.1.2 Heavy species submodel

The PIC method treats a physical system kinetically by tracking the motion of a representative number of particles, where each simulation particle represents a lumped number of real particles. The general procedure at each time step is to weight particles to grid nodes, thereby generating a continuum approximation for their distribution. This distribution is used to calculate self-induced fields that are then weighted back to the particles as forces. Finally, the applied forces are used to integrate the particle equations of motion, setting up the particle distribution for the next time step. Figures 4-1 and 4-2 illustrate the procedure. The sketches in 4-2 have only a single particle per cell for visual clarity – in general, for good statistics, ∼20-30 macroparticles per cell are needed.

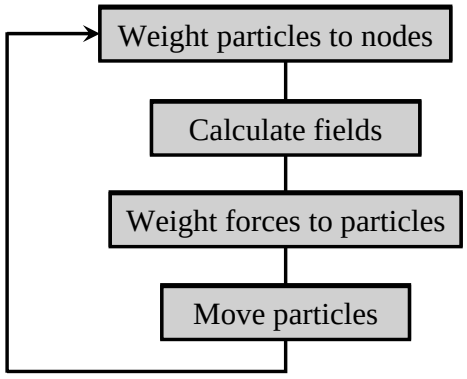

Figure 4-1: Particle-In-Cell loop.

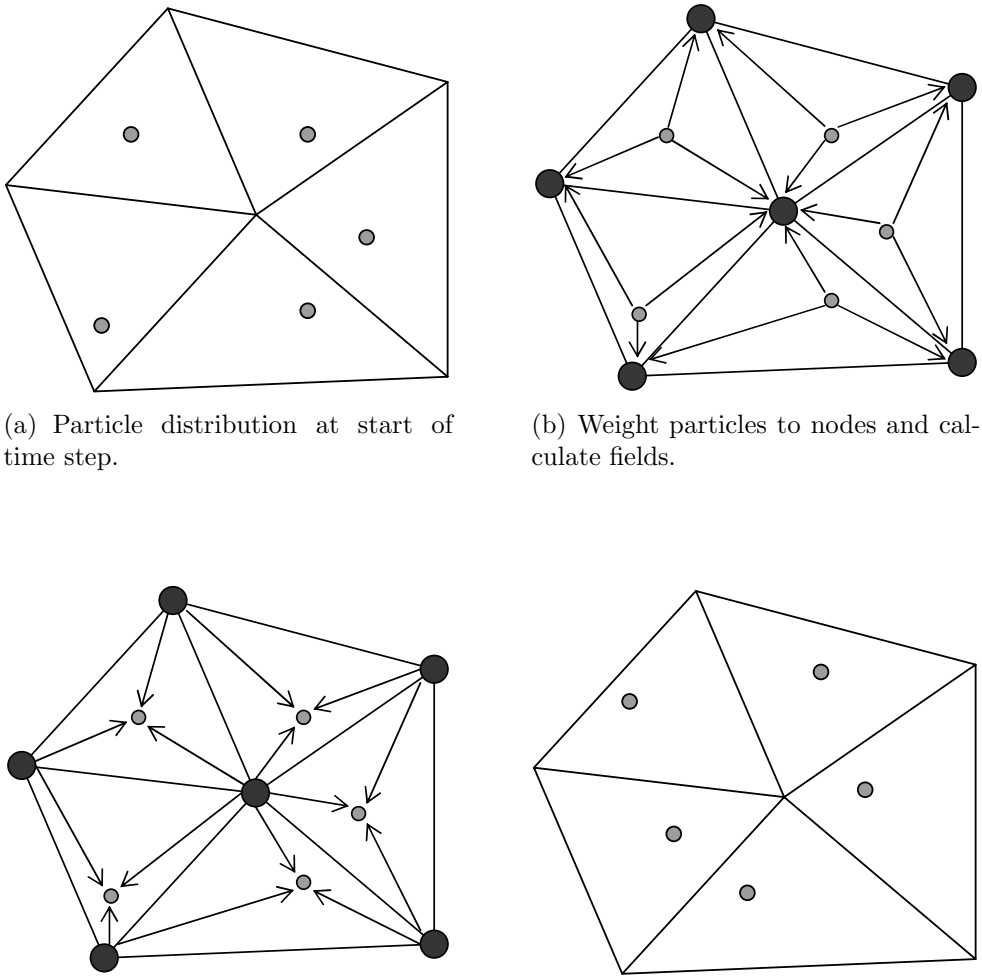

(a) Particle distribution at start of time step.

(b) Weight particles to nodes and calculate fields.

(c) Weight forces due to fields to particles.

(d) Move particles.

Figure 4-2: Illustration of Particle-In-Cell procedure.

In *HPHall*, charged ions are subject to the Lorentz force,

$$\vec{F} = q(\vec{E} + \vec{v} \times \vec{B}), \tag{4.1}$$

where q is the ion charge, $\vec{E}$ is the electric field, $\vec{v}$ is the ion velocity and $\vec{B}$ is the magnetic field. Neutrals are not affected by the fields and have no force acting on them. Ions and neutrals are moved on a structured, conformal mesh in computational coordinates (ξ, η) that represent the thruster geometry in real coordinates (z, r). Grid nodes have integer values of ξ and η that are denoted with j and k, respectively. In general, $\xi = 1$ corresponds to the anode and propellant injection boundary, while the

inner and outer lateral walls are $\eta = 1$ and $\eta = k_{max}$. The simulation time step is chosen such that a typical computational ion does not cross more than one cell per iteration. Single and double ionization are modeled using Monte Carlo methods.

4.1.3 Electron submodel

Electrons in a Hall thruster lie in the strongly magnetized, diffusive regime and are modeled as a continuum. Because the magnetic field creates a large anisotropy in electron motion parallel and perpendicular to the field lines, transport in each of these directions is decoupled and can be considered separately.

Electrons are free to move along magnetic streamlines and it is assumed they thermalize, giving rise to a constant electron temperature along each line. Applying this assumption to a balance between the pressure gradient and electric force, a constant thermalized electric potential can be derived for each line,

$$\phi^*(\lambda) = \phi - \frac{kT_e}{e} ln(n_e), \tag{4.2}$$

where ϕ is the potential, k is Boltzmann's constant, T_e is electron temperature, e is elementary charge and n_e is plasma density. λ is the magnetic streamfunction, given by,

$$\frac{\partial \lambda}{\partial z} = rB_r, \tag{4.3}$$

$$\frac{\partial \lambda}{\partial r} = -rB_z, \tag{4.4}$$

and provides a convenient way to find the magnetic streamline at a point. ϕ^* and T_e are constants for a given value of λ. Once T_e for each magnetic line is determined by integrating the electron energy equation, the values of ϕ^* can be computed. Details of this procedure can be found in Fife's thesis.

Diffusion across the magnetic field is governed by a generalized Ohm's law that incorporates effects of electron collisions into an effective electron mobility, $\mu_{e,\perp}$. It is experimentally observed that the classical description of diffusion is not adequate

to account for the observed transport across field lines and an additional term representing this anomalous Bohm diffusion is added,

$$\mu_{e,\perp} = \frac{\mu_e}{\beta_e^2} + K_B \frac{1}{16B}, \tag{4.5}$$

where $\mu_e = e/\nu_{en} m_e$ is the electron mobility, $\beta_e = \omega_c/\nu_{en}$ is the electron Hall parameter and K_B is the Bohm coefficient. K_B is a parameter adjustable between 0 and 1 and is used to tune the code.

An electron energy equation is formulated and solved on a magnetic mesh using finite volume methods to find the electron temperature. The mesh is comprised of a set of magnetic streamlines, λ_l, where λ_1 corresponds to the first magnetic streamline that intersects the thruster anode and $\lambda_{l_{max}}$ represents the cathode line. A Dirichlet boundary condition is imposed at the cathode that sets the electron temperature to 5 eV. Ground is represented by the furthest downstream magnetic streamline and set to a temperature of 0.1 eV. Linear interpolation between the cathode and ground is used to calculate electron temperatures in this region.

4.1.4 *HPHall-2*

The original *HPHall* was upgraded by Parra et. al [61] and dubbed *HPHall-2*. This version of the code is the starting point of this research. Of primary concern to lifetime prediction is the treatment of the Bohm condition at boundaries. Due to the quasineutrality assumption, the computational material boundaries represent the entrance to the plasma sheath rather than the physical wall. A well-known property of sheaths is that ions enter them at the Bohm velocity, but it was found that ions exiting the *HPHall* simulation domain did not necessarily satisfy this condition. This behavior was due to insufficient resolution of the steepening profiles near the sheath edge. Thus, several approaches were taken to treat this matter. The correct weighting algorithm fixes the calculation of density at the wall based on adjacent nodes, but requires very fine meshes to achieve the necessary resolution to capture the strong gradients present in the presheath approach to the sheath edge. Another scheme,

Bohm-condition forcing, calculates the wall density as,

$$n_e|_{wall} = \frac{g_{Ni}|_{wall}}{v_{Bohm}}, \tag{4.6}$$

where g_{Ni} is the normal ion flux to the wall and the Bohm velocity is,

$$v_{Bohm} = \sqrt{\frac{T_e|_{wall}}{m_i}}. \tag{4.7}$$

It is found that the Bohm-condition forcing approach yields good results even on coarse meshes so this strategy is used for computations in this thesis.

4.2 Method for lifetime prediction

In using *HPHall* to address the issue of lifetime prediction, care has been taken to inspect and improve parts of the simulation process that affect the capability to accurately capture the wall and its erosion.

4.2.1 Grid generation

The computational mesh represents the domain in which the thruster plasma is simulated. In the case of erosion modeling, the mesh boundaries delineate the sputterable walls and since their evolution over the thruster lifetime is the desired output, it is important to be meticulous in its definition. Because the grid is structured, an equal number of nodes must be placed on the top and bottom boundaries as well as on the left and right boundaries. The Mesh Generator add-on in Tecplot is used to create the boundaries and then the mesh is computed using its iterative Elliptic-Laplace solver. Figure 4-3(a) shows the definition of the boundary nodes for a new BHT-200 thruster and Figure 4-3(b) shows the corresponding computed mesh. The actual thruster geometry is followed as closely as possible.

As the lifetime of the thruster is simulated, the mesh is updated at intervals to reflect the regression of the ceramic components. The eroded wall profile of the thruster

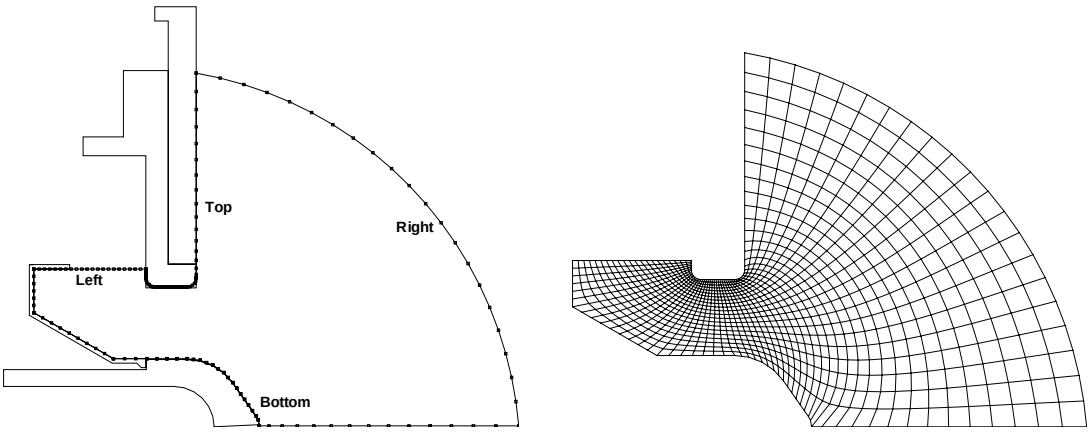

(a) Definition of boundary nodes. (b) Computational mesh.

Figure 4-3: Generation of BHT-200 simulation grid in Tecplot Mesh Generator.

is used to refresh the boundary nodes and the corresponding mesh is generated as input to the next operation period. An example of an evolved mesh is presented later.

4.2.2 Magnetic field interpolation

In addition to the computational grid, the thruster's magnetic field is needed for the problem definition. The Maxwell project used in the engine's design outputs the $\vec{B}$ field on a Cartesian mesh larger than the simulation domain. A utility then interpolates values from the rectangular to the computational grid. For use in lifetime modeling, this utility is upgraded to also have Maxwell directly output the $\vec{B}$ field at the boundary nodes and assign these magnetic field values to the mesh perimeter. The need for this addition arises because the computational domain may lie adjacent to thruster components that contain higher fields than the free space of the acceleration channel. During the original interpolation scheme, an elevated interior value could contribute to the edge nodes, resulting in the assignment of an artificially high field. Previously, this issue had been dealt with by slightly offsetting the computational boundary from the true boundary. However, since the aim is to accurately predict erosion at the wall, the grid should represent the geometry as closely as possible.

As with the grid generation, each time the thruster geometry is updated, a new magnetic field input file is created based on the new computational mesh. Though

the erosion of the ceramic does not change the magnetic field, it does expand the acceleration channel and the field in this new area is necessary for the next calculation.

4.2.3 Wall definition

In preparing *HPHall* for use in lifetime prediction, a data structure to track wall properties at panels instead of nodes is implemented. This method simplifies handling of domain corners and eliminates ambiguities in recording quantities such as fluxes and wall normals. Definition of boundary conditions for different wall regions is also improved as confusion about the material represented by a node between two distinct areas is removed.

4.2.4 Particle mover

As described in Section 4.1.2, particles are moved according to the PIC method at each iteration. In the original particle mover, after all particles have been moved, those falling outside the computational domain based on their (ξ, η) coordinates get passed into the boundary condition handling routine. If a top or bottom edge is crossed, the final ξ coordinate is taken as the boundary crossing location. Similarly, if a left or right edge is crossed, the final η coordinate represents the perimeter intersection. However, as pictured in Figure 4-4, the actual and simulated boundary crossings may be quite different. Again, because the aim is to predict the wall erosion as accurately as possible, improvement of the particle mover to register boundary crossings at the correct location is undertaken.

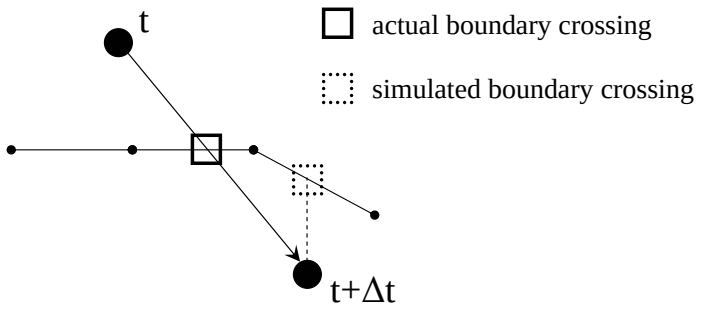

Figure 4-4: Particle crossing grid boundary.

Another issue with the previous particle mover is that the functions to map particle positions from real (z, r) to computational (ξ, η) coordinates have an associated error that occasionally assigns particles to the incorrect cell. Thus, to prevent lost particles, the strategy taken is to rigorously track particles as they cross any cell boundaries, edge or interior. Then, if calculated (ξ, η) coordinates do not fall in the correct cell, corrective measures are taken to properly locate the particle. Figure 4-5 shows how this cell crossing bookkeeping is performed. During the iteration, the particle moves from its initial to its final location as seen in Figure 4-5(a). The particle mover knows the original cell from the previous time step and begins checking for crossing of its edges. As drawn in Figure 4-5(b), lines can be defined for the particle trajectory and the cell edge being checked. If P_A is the line defining the particle path and P_B the cell edge, they can be expressed as,

$$P_A = P_1 + u_a(P_2 - P_1), \tag{4.8}$$

$$P_B = P_3 + u_b(P_4 - P_3), \tag{4.9}$$

where $P_1 = (z_1, r_1)$ and $P_2 = (z_2, r_2)$ are the endpoints of the particle trajectory and $P_3 = (z_3, r_3)$ and $P_4 = (z_4, r_4)$ are the endpoints of the cell edge. To find the intersection between the two lines, their equations are set equal to each other, $P_A = P_B$, or,

$$\begin{aligned} z_1 + u_a(z_2 - z_1) &= z_3 + u_b(z_4 - z_3), & (4.10)\\ r_1 + u_a(r_2 - r_1) &= r_3 + u_b(r_4 - r_3). & (4.11) \end{aligned}$$

Rearranging Equations 4.10 and 4.11,

$$u_a = \frac{(z_4 - z_3)(r_1 - r_3) - (r_4 - r_3)(z_1 - z_3)}{(r_4 - r_3)(z_2 - z_1) - (z_4 - z_3)(r_2 - r_1)}, \tag{4.12}$$

$$u_b = \frac{(z_2 - z_1)(r_1 - r_3) - (r_2 - r_1)(z_1 - z_3)}{(r_4 - r_3)(z_2 - z_1) - (z_4 - z_3)(r_2 - r_1)}, \tag{4.13}$$

where u_a gives the position along the particle trajectory of the intersection and u_b gives the position along the cell edge of the intersection. Values of u_a and u_b between 0 and 1 correspond to positions between the two endpoints used to define the lines. Thus, the condition for an intersection to happen is,

$$\begin{cases} 0 \leq u_a \leq 1, \\ 0 \leq u_b \leq 1. \end{cases} \tag{4.14}$$

In the case of Figure 4-5(b), the intersection condition is satisfied and the next cell is then inspected for crossings, the edge just crossed being omitted from the checking. Eventually, the exit of the intermediate cell is found as sketched in Figure 4-5(c). In general, this procedure continues until the particle either crosses a grid boundary or reaches its final destination cell. Figure 4-5(d) displays the search path followed in the example. With the rigorous particle-moving scheme, the exact locations of particles leaving the simulation domain are now available for use in the erosion model.

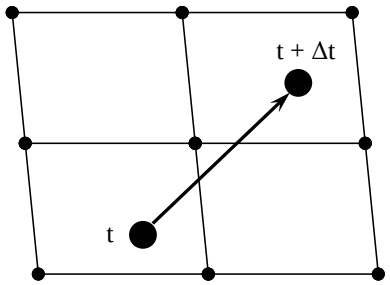

(a) Particle moves during iteration.

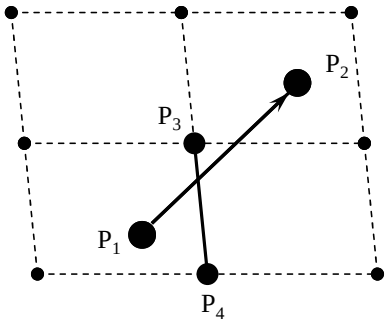

(b) Check for crossing out of original cell.

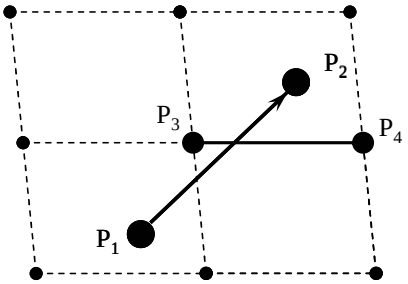

(c) Check for crossing out of intermediate cell.

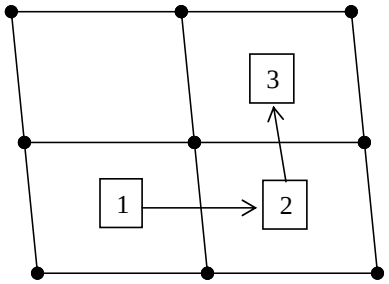

(d) Search path for particle location.

Figure 4-5: Procedure for tracking particle grid crossings.

4.2.5 Erosion model

Ions that cross the grid boundary where ceramic is located cause sputtering and contribute to the thruster's erosion. Figure 4-6 sketches the steps the ion undergoes after exiting the simulation domain. As drawn in Figure 4-6(a), the grid edge represents the sheath boundary rather than the physical wall. In Figure 4-6(b), the ion's incident energy is calculated as the sum of its kinetic and potential energies,

$$E_i = \frac{1}{2} m_i v^2 + q\Delta\phi, \tag{4.15}$$

where m_i is the ion mass, v is the ion speed, q is the ion charge and $\Delta\phi$ is the sheath potential drop. Next, as shown in Figure 4-6(c), the incident angle is computed. As the ion falls through the sheath, the potential drop increases its normal velocity component by an amount,

$$\Delta v_n = \sqrt{v^2 + \frac{2e\Delta\phi}{m_i}} - v. \tag{4.16}$$

This change in the velocity vector leads to an effective incident angle given by,

$$\theta_i^* = tan^{-1}\left(\frac{v_t}{v_n + \Delta v_n}\right), \tag{4.17}$$

where v_t and v_n are the pre-sheath tangential and normal velocity components. The sheath tends to make the particle trajectories more normally incident with the surface. Finally, as depicted in Figure 4-6(d), the sputter yield can be calculated,

$$Y = f(E_i, \theta_i^*). \tag{4.18}$$

The sputter yield's dependence on incident energy and angle is that described in Section 3.3. The units of Y are mm^3/ion as given by the experimentalist – volumetric sputter yield measurements are often used when studying multicomponent materials to avoid the ambiguity of which component is being removed.

The conversion of the sputter yield to an equivalent erosion depth is illustrated in Figure 4-7. The first step is to convert the sputter yield into a total yield as each

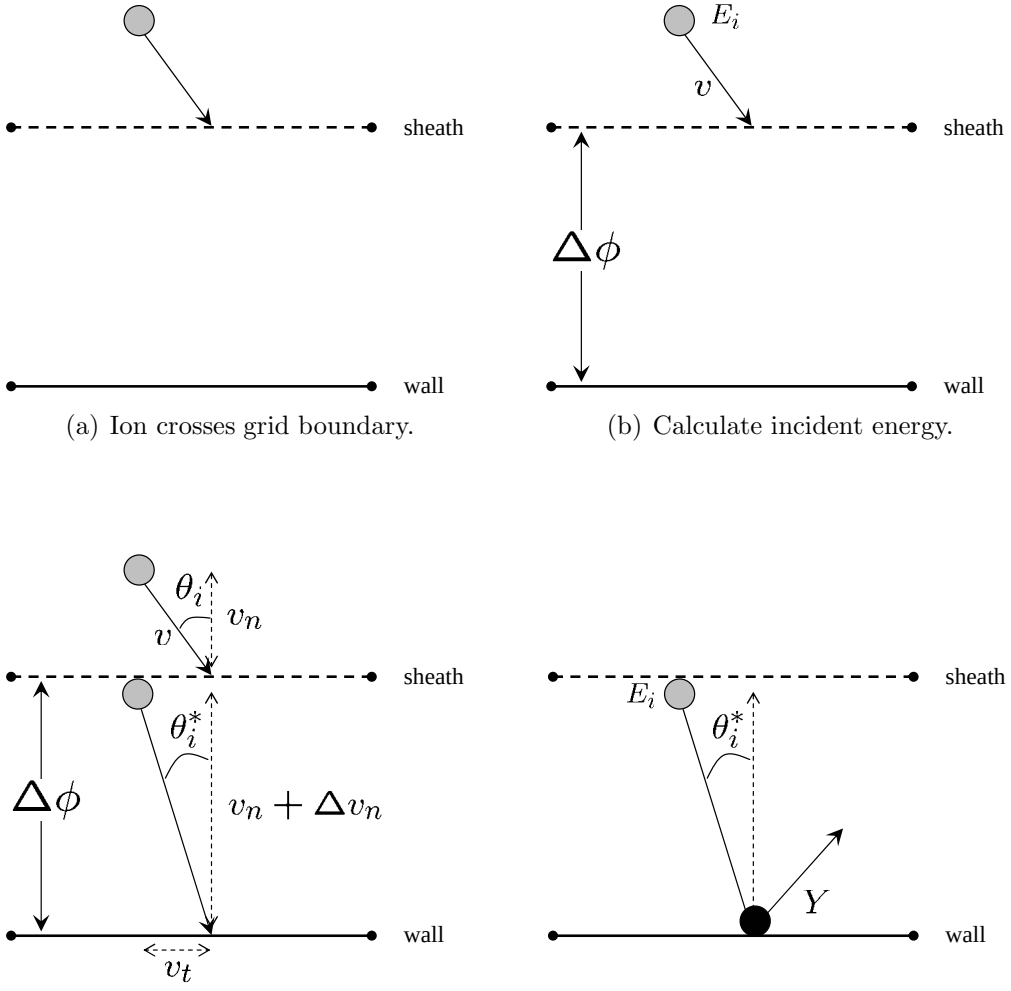

(a) Ion crosses grid boundary.

(b) Calculate incident energy.

(c) Calculate incident angle.

(d) Calculate sputter yield.

Figure 4-6: Sputtering calculation as ion crosses grid boundary.

simulated particle is actually a macroparticle that represents many real particles. The total yield is given by,

$$Y_{tot} = wt * Y, \tag{4.19}$$

where wt is the macroparticle weighting, or the number of real particles it stands for. Next, the total volumetric yield is translated into an erosion depth by considering the conical frustum created by revolving the wall panel about the thruster centerline. The surface area of this body is,

$$A = 2\pi r_m l_p, \tag{4.20}$$

where r_m is the mean radius and l_p is the panel length. The erosion depth is then given by,

$$d_{erode} = \frac{Y_{tot}}{A}, \tag{4.21}$$

and is weighted to the panel nodes by considering the location along the panel where the impact happens. If x is the fractional panel distance of the sputtering event from the left node, $(1 - x) * d_{erode}$ will be the contribution to node L while node R will receive $x * d_{erode}$. The scenario drawn in Figure 4-7(c) corresponds to a x of $\frac{1}{3}$. Finally, the erosion depths at panel nodes are used to move the corresponding global nodes normal to the panel. The cumulative axial and radial erosion depths of the relevant boundary nodes are tracked at each iteration and used in post-processing to determine nodal erosion rates. Figure 4-8 shows the radial erosion depth as a function of time for an upstream and downstream node of the BHT-200. The erosion rate is then found as the slope of the best-fit line. Once the erosion rates are calculated, the thruster geometry is altered by choosing a sputter time step and moving the affected wall nodes by the corresponding distance. Selection of this time step is thruster-dependent and will be discussed in the results chapters. Figure 4-9 shows the procedural flow chart for modeling the thruster erosion. The process is repeated until the desired number of hours of thruster operation is achieved. Figure 4-10 shows a grid geometry as it

evolves over 500 hours with a sputter time step of 100 hours.

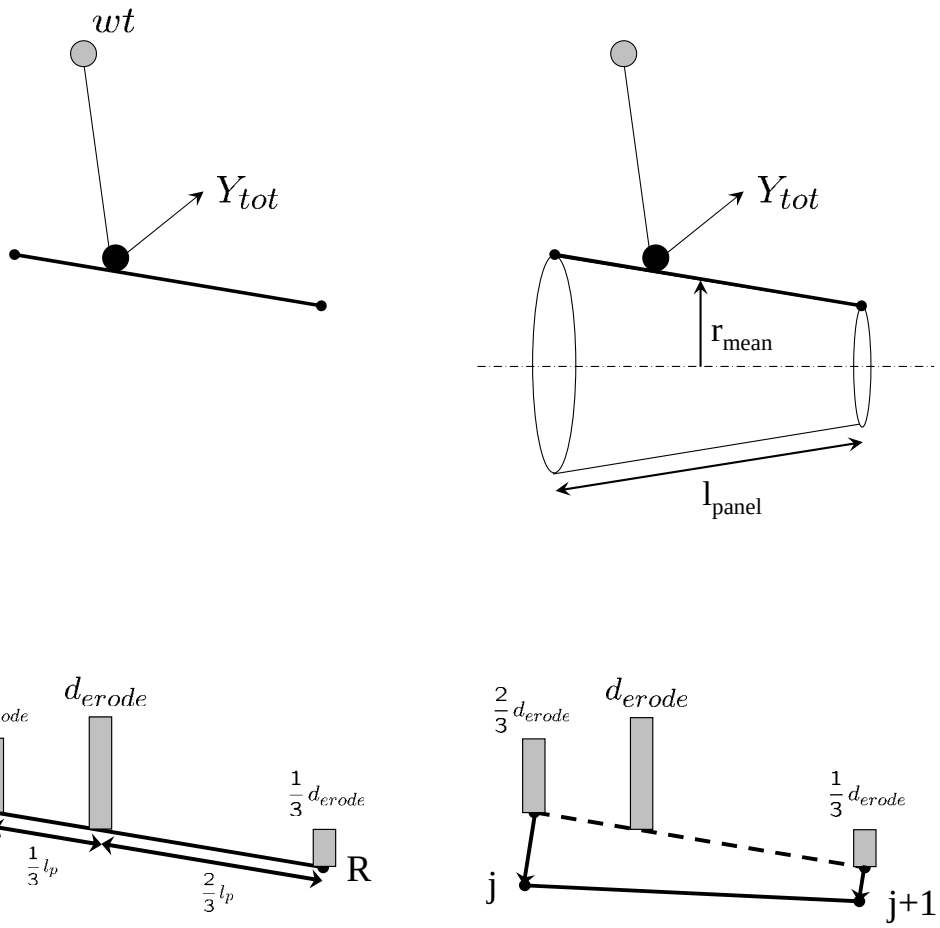

(c) Weight erosion depth to panel nodes.

(d) Move global nodes normal to panel.

Figure 4-7: Conversion of sputter yield to erosion depth.

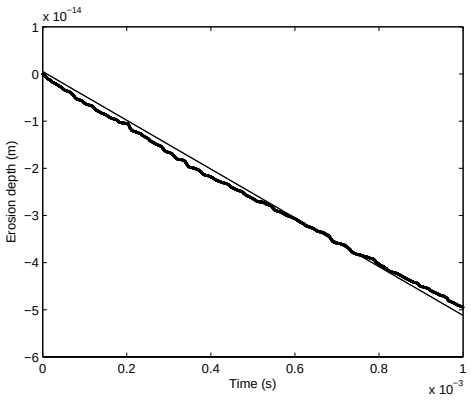

(a) Upstream node, $\frac{dr}{dt} = -5.17 \times 10^{-11}$ m/s.

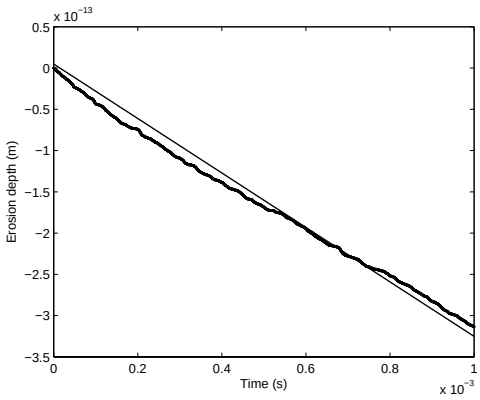

(b) Downstream node, $\frac{dr}{dt} = -3.30 \times 10^{-10}$ m/s.

Figure 4-8: Panel radial erosion depth as function of run iteration.

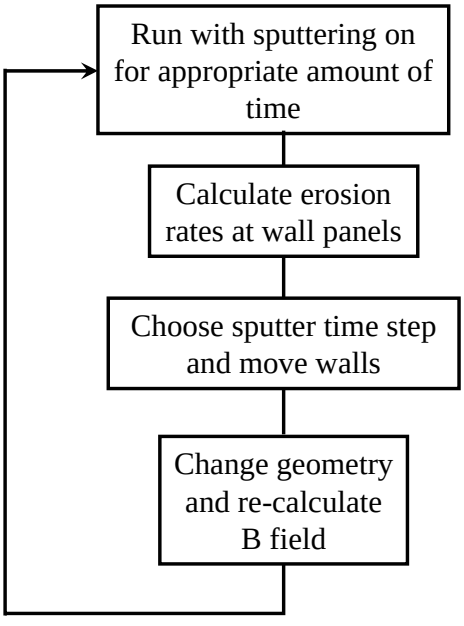

Figure 4-9: Erosion model flow chart.

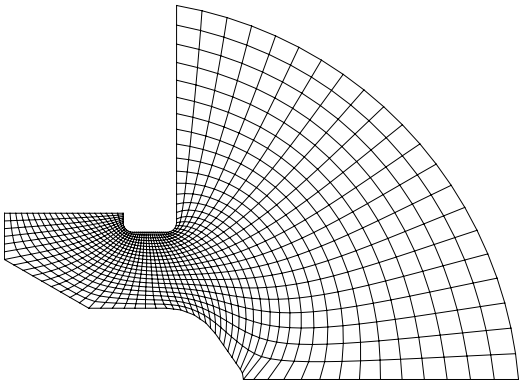

(a) Baseline.

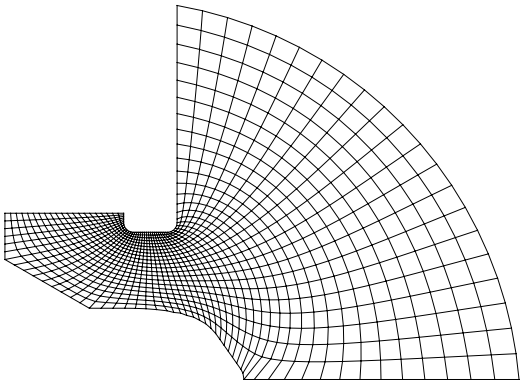

(b) 100 hours.

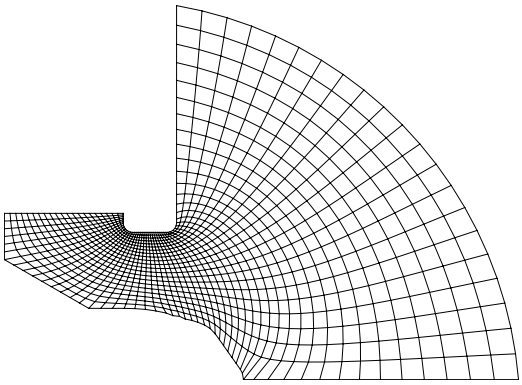

(c) 200 hours.

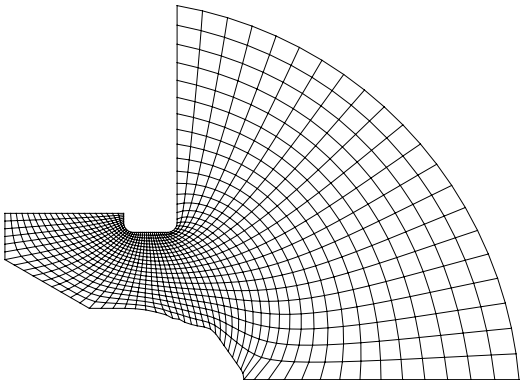

(d) 300 hours.

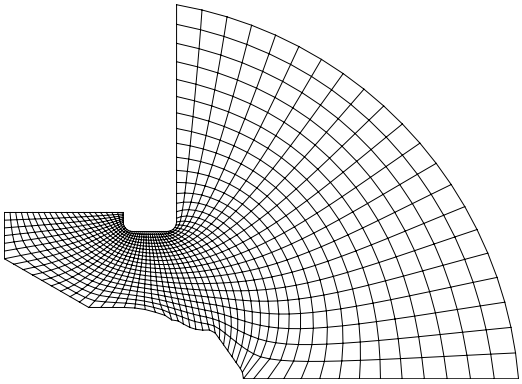

(e) 400 hours.

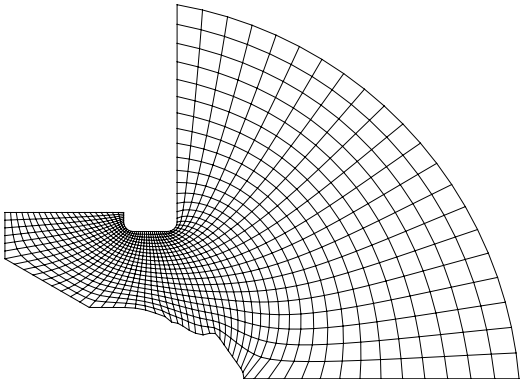

(f) 500 hours.

Figure 4-10: Evolution of computational mesh.

4.2.6 Anomalous transport model

As described in Section 4.1.3, *HPHall* models anomalous transport by applying a constant Bohm coefficient across the domain. However, experimental evidence shows that the anomalous electron mobility is highly correlated with the $E \times B$ drift velocity shear, giving rise to a transport barrier near the exit channel of the thruster [12]. The exact definition of the physics describing this behavior is a topic still under investigation [5, 28], but is beyond the scope of this work to explore. Nevertheless, the effect exists and is important in determining the nature of the plasma discharge and subsequently its erosion of the channel walls. Thus, a method is implemented to manually impose a transport barrier in an educated manner, a technique that has been successful with other thruster models [4, 27, 48].

The imposed transport barrier is specified by prescribing a range of axial coordinates in which the anomalous Bohm diffusion is quenched, or where only classical transport is applied. Outside of the barrier, the usual method of adding the constant Bohm coefficient to the classical contribution for the electron mobility is followed. Figure 4-11 shows the weighting used by a representative transport barrier imposed between $z = 0.015 - 0.0175m$. The effective Bohm coefficient is given by,

$$K_{B_{eff}} = [1 - w_b(z)]\, K_B. \tag{4.22}$$

Thus, inside the barrier, $K_{B_{eff}} = 0$ and only classical diffusion is accounted for. Outside the barrier, $K_{B_{eff}} = K_B$ and both classical and anomalous diffusion are present. The exact location and thickness of the barrier is thruster-dependent and the selection process of these inputs will be discussed during presentation of the simulation results in Chapters 5 and 6.

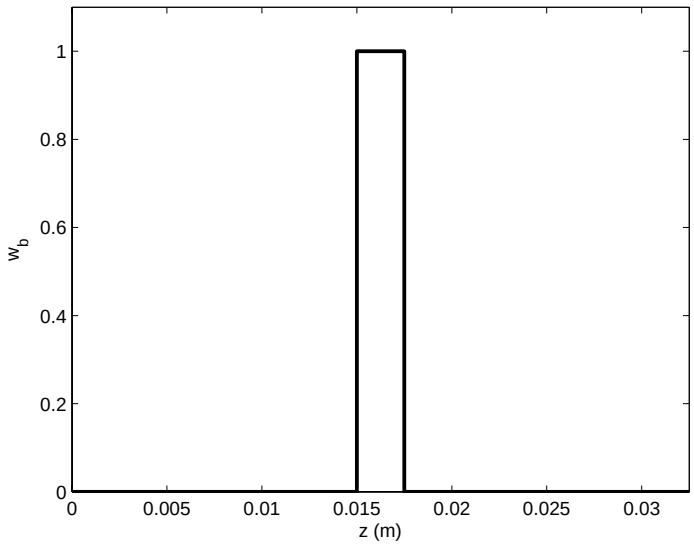

Figure 4-11: Representative imposed transport barrier weighting.

Chapter 5

BHT-200 results

Modeling of the lifetime and erosion of the BHT-200 are the subject of this chapter. First, the thruster and its simulation inputs are described. Then, tuning of the code to provide estimates of erosion profiles for the first 500 hours of thruster operation is presented. Finally, the tuned code is used to predict the overall lifetime of the engine.

5.1 BHT-200

The BHT-200, pictured in Figure 5-1, is a low power Hall thruster developed by Busek Co. Inc. Its nominal specifications are summarized in Table 5.1. A series of experimental nose cone profiles taken in 100 hour increments during the first 500 hours of thruster life is available for comparison to simulation results. These measurements were taken with an optical comparator and have an estimated error of ± 0.127 mm. After the initial 500 hours of operation, the thruster was sent to Edwards Air Force Base to complete its life testing and fired for long duration for an additional 1,200+ hours.

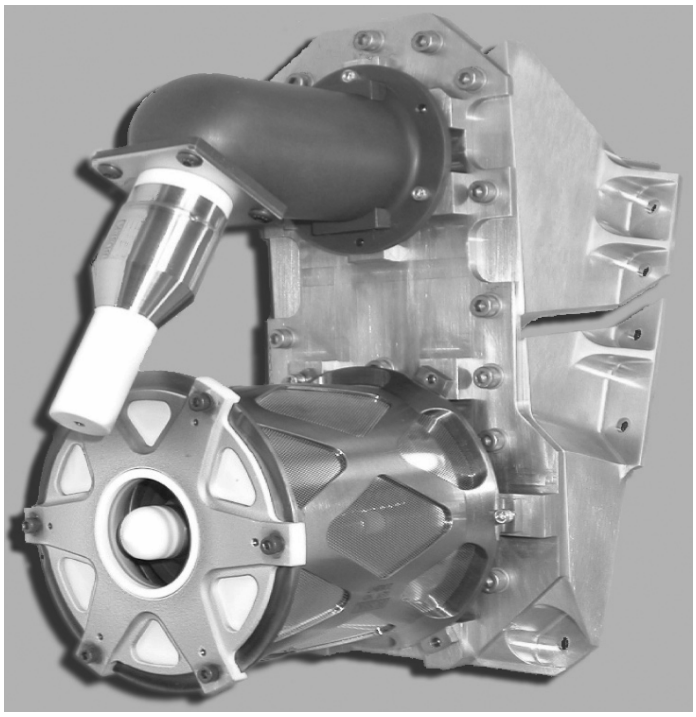

Figure 5-1: BHT-200 thruster [39].

Table 5.1: BHT-200 nominal specifications [39].

Discharge input power	200 W
Discharge voltage	250 V
Discharge current	0.8 A
Propellant mass flowrate	0.94 mg/s
Thrust	12.8 mN
Specific Impulse	1390 s
Propulsive efficiency	43.5%

5.2 Simulation procedure

In this section, the baseline setup for modeling of the BHT-200 is described as well as the process followed to advance the simulated thruster through its virtual life test.

5.2.1 Baseline mesh

The 53×22 computational mesh is based on the thruster geometry depicted in Figure 5-2. The inner nose cone is made of HBC grade BN and its erosion is the lifetime-limiting factor of the engine. Figure 5-3 shows a detail of the mesh near the nose cone – the numbered panels are those subject to sputtering and will move as the ceramic erodes.

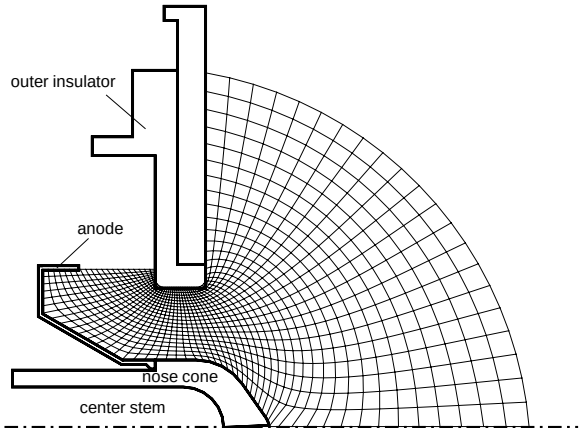

Figure 5-2: BHT-200: Initial geometry.

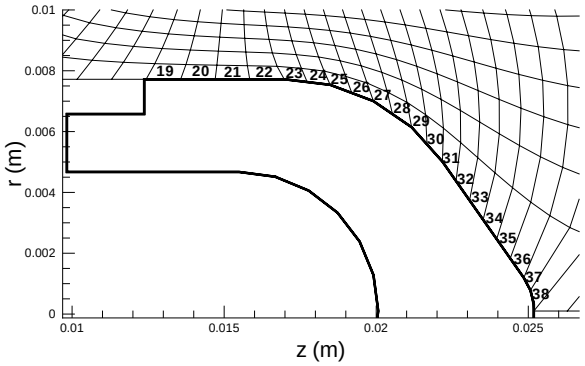

Figure 5-3: BHT-200: Detail of nose cone panels.

5.2.2 Baseline magnetic field

The magnetic field extracted from the thruster's Maxwell project is pictured in Figure 5-4 and the corresponding magnetic streamline mesh in Figure 5-5. As the thruster geometry evolves, the magnetic field and mesh are re-computed to account for the additional space created by the expansion of the acceleration channel.

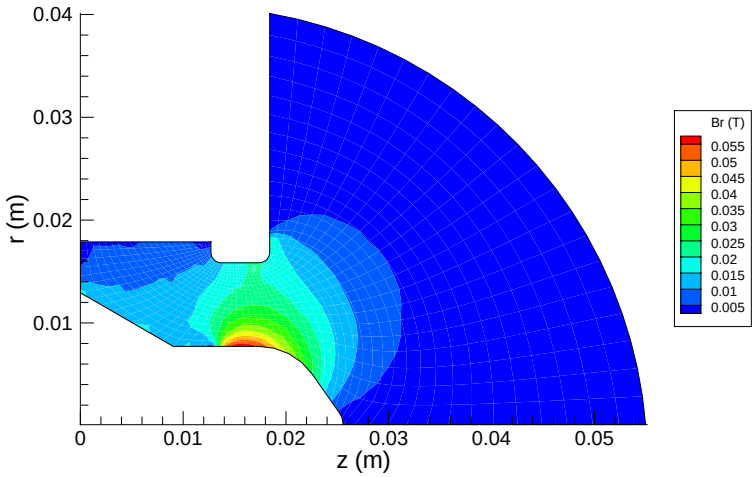

Figure 5-4: BHT-200: Initial magnetic field.

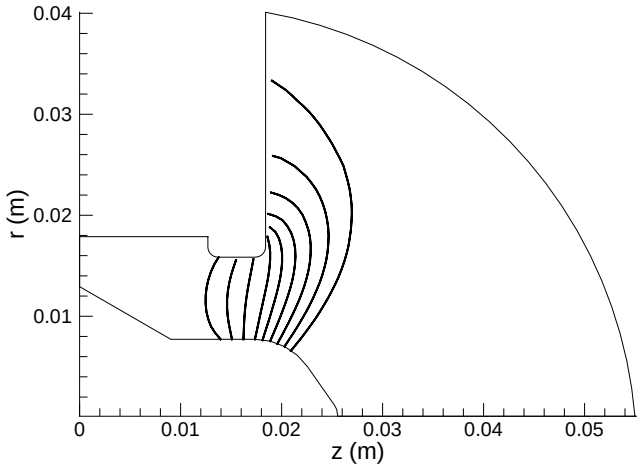

Figure 5-5: BHT-200: Initial magnetic mesh.

5.2.3 Input parameters

Table 5.2 lists the key *HPHall* inputs that specify the simulated thruster operation. Note that the mass flow rate is less than that given in Table 5.1, which reports the

Table 5.2: BHT-200 simulation parameters.

M_DOT	0.884×10^{-6} kg/s
V_DISCHARGE	250.3 V
P_CHAMBER	$2.2e\times10^{-6}$ Torr
T_CHAMBER	300 K
T_WALL	700 K
BOHM_K	0.15
(Z_ANODE, R_ANODE)	(0.0115715, 0.00911707)
(Z_CATHODE, R_CATHODE)	(0.0389636, 0.030)

total mass flow to the anode and cathode. Because *HPHall* does not directly simulate the cathode, only mass flow to the anode is injected. Discharge voltage and chamber conditions are those used during the 500 hour life test and wall temperature is set at ∼400°C. Previous experience simulating an earlier thruster configuration [14], aided in setting the value of the Bohm coefficient, K_B. The anode location is selected to lie on the magnetic line that first intersects a metal component as one moves upstream. For the baseline configuration, this streamline begins at the node shared by Panels 18 and 19, the point where the anode and nose cone meet. The cathode position corresponds to its physical location.

5.2.4 Execution sequence

Each simulated lifetime increment requires three *HPHall* runs. To fill the grid with neutrals, 20,000 iterations of NEUTRALS_ONLY mode are performed. Next, 1,400 iterations in NORMAL (all plasma species simulated) mode are used to bypass an initial transient the code exhibits before settling into steady thruster operation. Finally, a longer run in NORMAL mode is done to establish wall erosion rates at this point in the thruster's life. For the BHT-200 geometry, these runs are performed for 20,000 iterations. Figure 5-6 shows the calculated erosion rate as a function of run iteration for both an upstream and downstream location. The dashed line denotes the 20,000 iteration mark and shows that its choice is a good compromise between reaching the steady-state erosion rate and having reasonable run times. All runs use an iteration time step of 5×10^{-8} s.

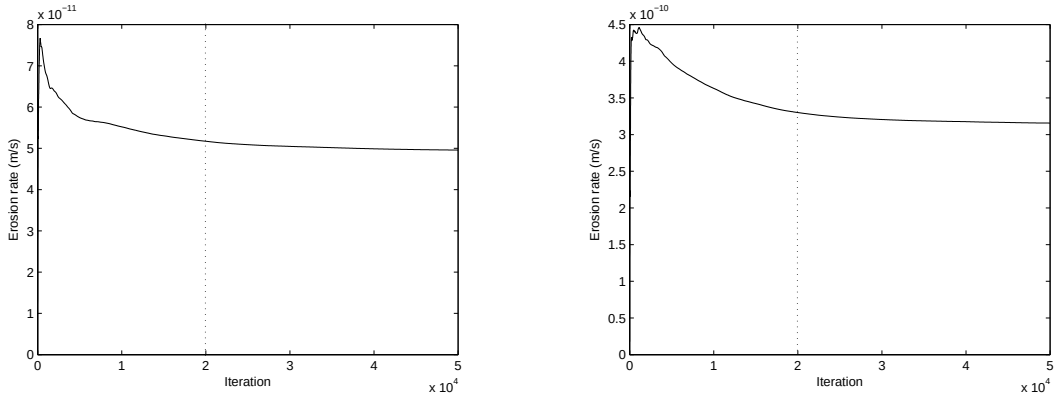

(a) Upstream location. (b) Downstream location.

Figure 5-6: BHT-200: Wall erosion rate as function of run iteration.

The wall erosion rates are then used to step the wall profile forward in its lifetime. Since the BHT-200 experimental nose cone profiles have been taken in steps of 100 hours, the wall profiles are advanced 100 hours between lifetime runs. To test that 100 hours is a reasonable increment to take, two cases are performed with identical input parameters. Figure 5-7 shows the wall profiles after 500 hours of operation for the two cases. Case 1 takes steps of 100 hours and represents the ending wall profile after 5 lifetime runs. Case 2 takes steps of 50 hours and represents the final wall profile after 10 lifetime runs. The two cases are virtually identical meaning 100 hour time steps are reasonable.

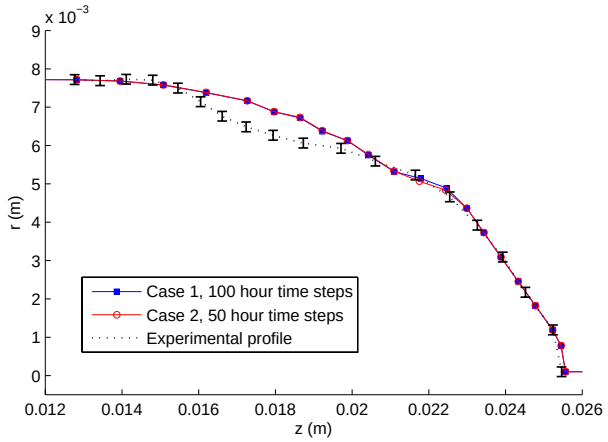

Figure 5-7: BHT-200: Comparison of sputter time steps at 500 hours of operation.

5.3 Erosion profile results

The next sections describe highlights of the process followed in tuning the simulation to model the BHT-200. Figure 5-8 shows the experimentally measured erosion profiles of the thruster nose cone. The erosion is primarily concentrated just before the nose cone bends away from the channel's centerline axis.

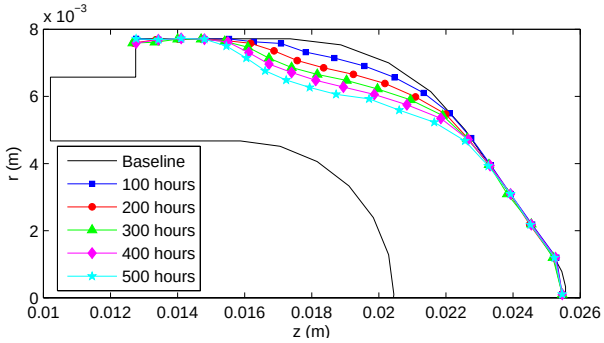

Figure 5-8: BHT-200: Experimental erosion profiles.

5.3.1 Effect of sputter threshold

The first parameter adjusted is the sputter threshold, E_{th}, that determines the energy cutoff below which an incoming ion cannot cause any erosion. Figure 5-9 shows the evolution of the wall profiles over the first 500 hours of thruster operation for different threshold levels. As seen at each lifetime step, wall profiles representing lower E_{th} exhibit greater erosion. The effect of the sputter threshold becomes more pronounced as the simulated life test continues and the case profiles diverge from one another. Figure 5-10 plots the deviation of the simulated wall profiles from those measured experimentally. Positive deviations correspond to regions where erosion is under-predicted, while negative deviations mean erosion is overestimated. The divergence of the case profiles from one another is clearly apparent again and most cases have worse agreement with the experimental data as time progresses. To get an overall picture of the wall regression, an integration of the material removed at each panel is performed along the nose cone. The volumetric erosion during each 100 hour increment is plotted in Figure 5-11. From the erosion profiles, profile deviations and the net erosion, it appears that an E_{th} of 50 eV is too high, resulting in inadequate

sputtering, while 0 eV results in too much material removal. Although 10 eV gives closer profile matching in the mid-region of the acceleration channel, erosion of the upstream section and where the nose cone begins to bend toward the centerline is overpredicted. Hence, a conservative 30 eV threshold is used for the rest of the simulation cases since additional physics is yet to be added.

Averaged wall distributions from the run representing 400-500 hours can be seen in Figure 5-12. In this and following plots, energy denotes the total energy an ion strikes the wall with – it is this energy that is passed into the sputter model. The total energy has both kinetic and potential contributions. Kinetic energy is that with which the particle arrives at the sheath. Potential energy is the amount added to account for falling through the sheath. In the case of single ions, this distribution directly corresponds to the sheath voltage. Little wear of the initial upstream panels is explained by the combination of low incident flux, energy and angle to this area. Evidence of the plasma's acceleration as it streams out of the channel is clear in the energy and kinetic energy distributions. Finally, as suggested by the sharp drop in flux, the downstream region where the nose cone has turned towards the centerline remains effectively untouched by the ions as the wall bends away from the flow. Figure 5-13 displays the computed recession rates along the wall during the same run – rates are reported in terms of axial and radial components. The net erosion rate would be the magnitude of the vector defined by the two components. It is apparent that the erosion is primarily radial and tracks the energy closely – high energy is equivalent to high erosion rate. While flux to the wall is necessary for sputtering, its importance is clearly overshadowed by that of the energy. These observations further reinforce the idea that low-energy sputtering behavior plays a critical role in the issue. As seen in Figure 5-12(b), the energies considered fall well within this poorly understood sputtering regime. As demonstrated in Figure 3-10(b), selection of E_{th} alters the level of the near-threshold yield curve considerably and as the simulation indicates, this in turn determines the erosion rates. Therefore, accurately reproducing the spatial energy distribution and choosing the proper sputter threshold are paramount in correctly predicting evolution of the thruster geometry.

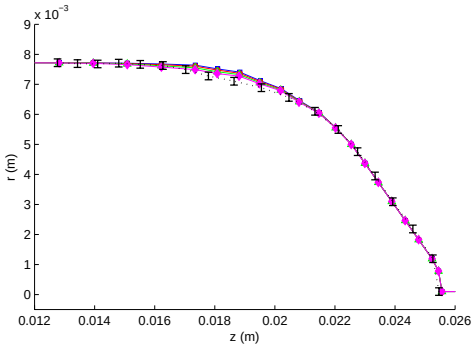

(a) 100 hours.

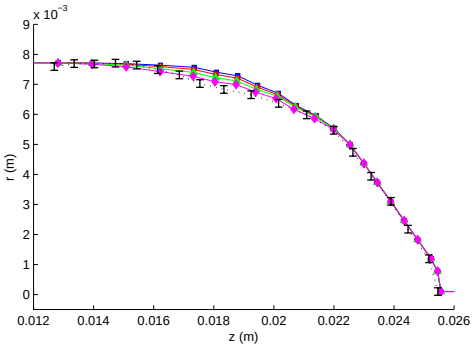

(b) 200 hours.

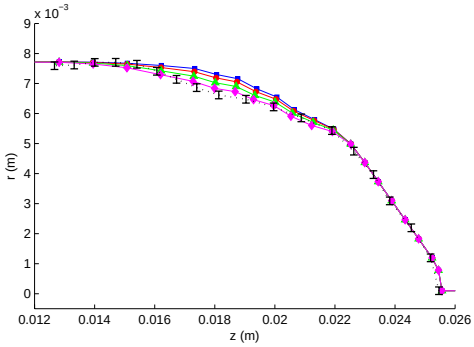

(c) 300 hours.

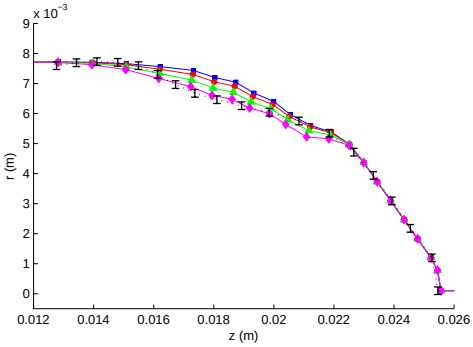

(d) 400 hours.

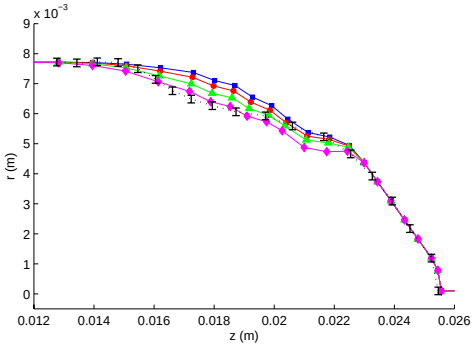

(e) 500 hours.

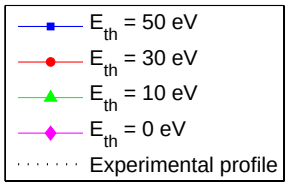

Figure 5-9: BHT-200: Erosion profile evolution – effect of sputter threshold.

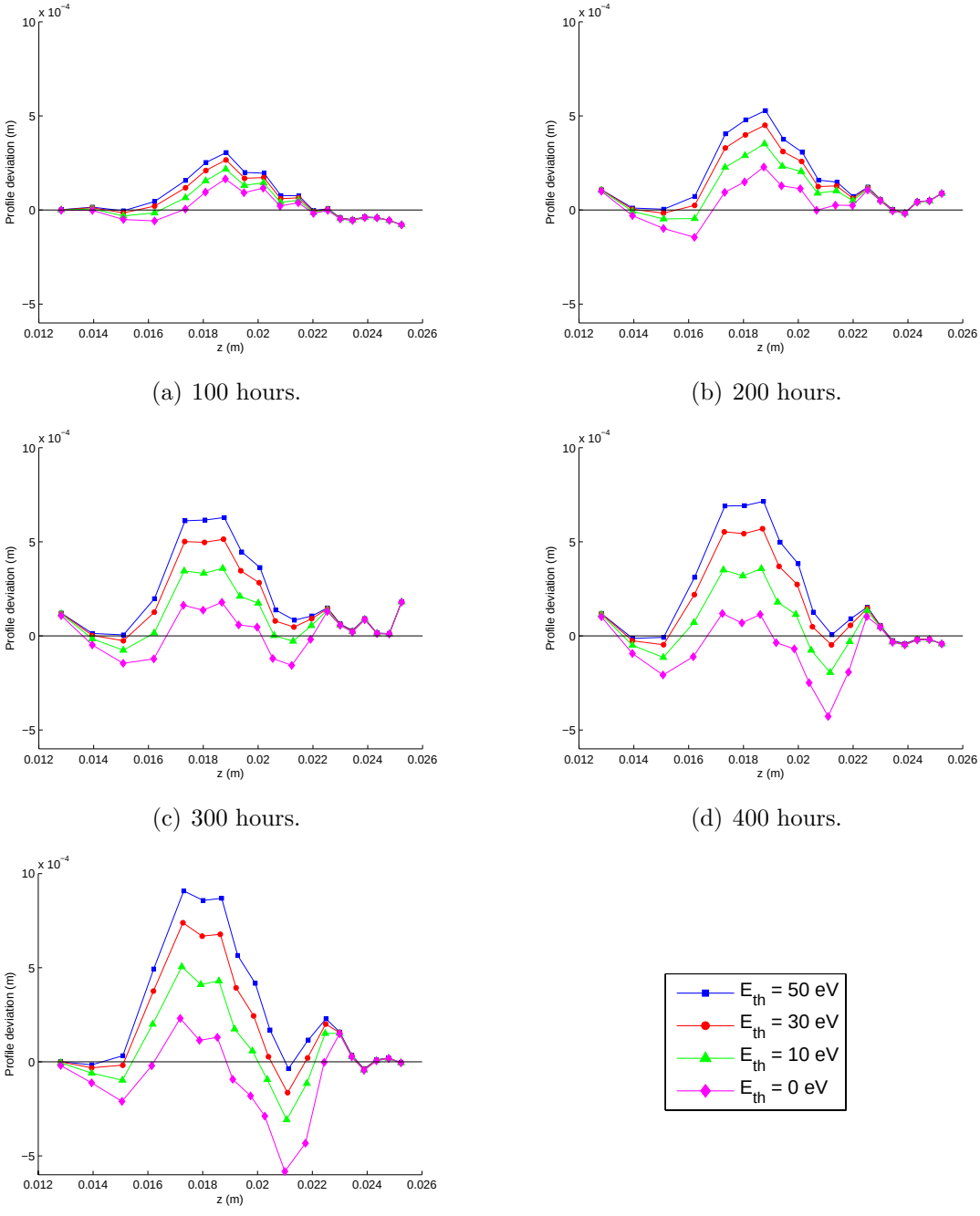

(a) 100 hours.

(b) 200 hours.

(c) 300 hours.

(d) 400 hours.

(e) 500 hours.

Figure 5-10: BHT-200: Erosion profile deviation – effect of sputter threshold.

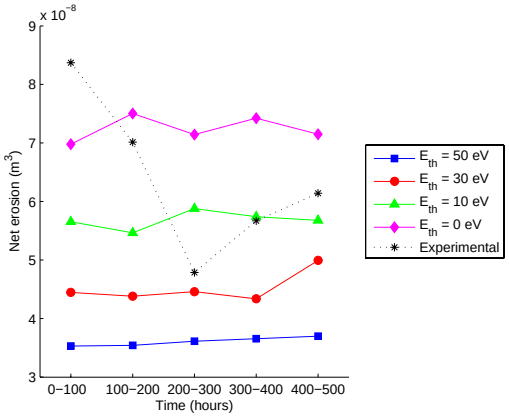

Figure 5-11: BHT-200: Net erosion – effect of sputter threshold.

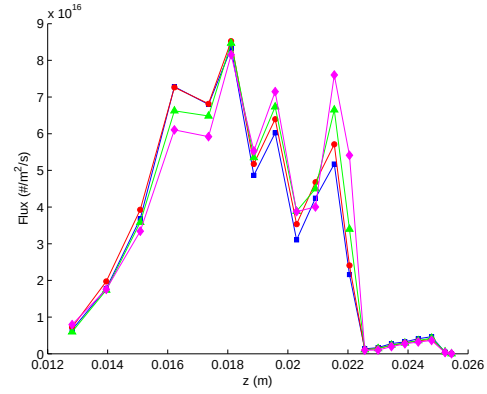

(a) Flux.

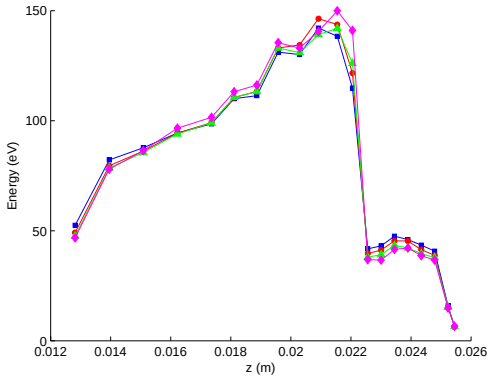

(b) Energy.

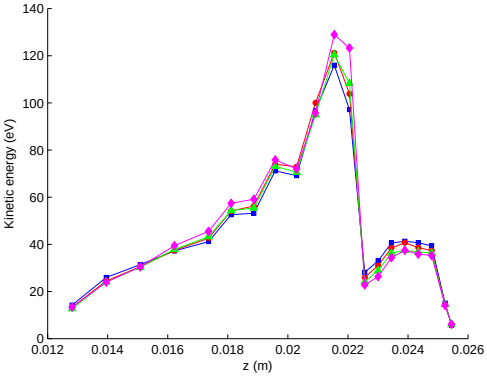

(c) Kinetic energy.

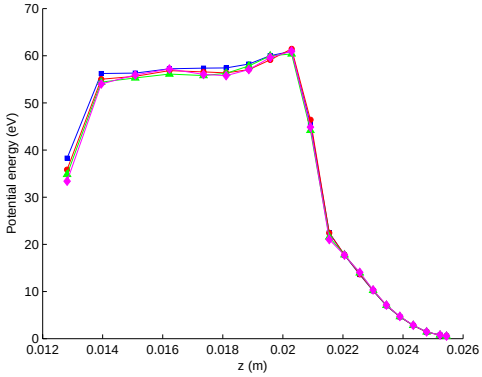

(d) Potential energy.

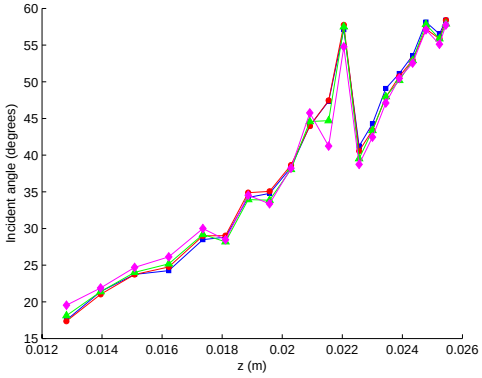

(e) Incident angle.

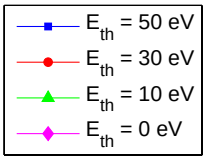

Figure 5-12: BHT-200: Averaged wall distributions during 400-500 hour run – effect of sputter threshold.

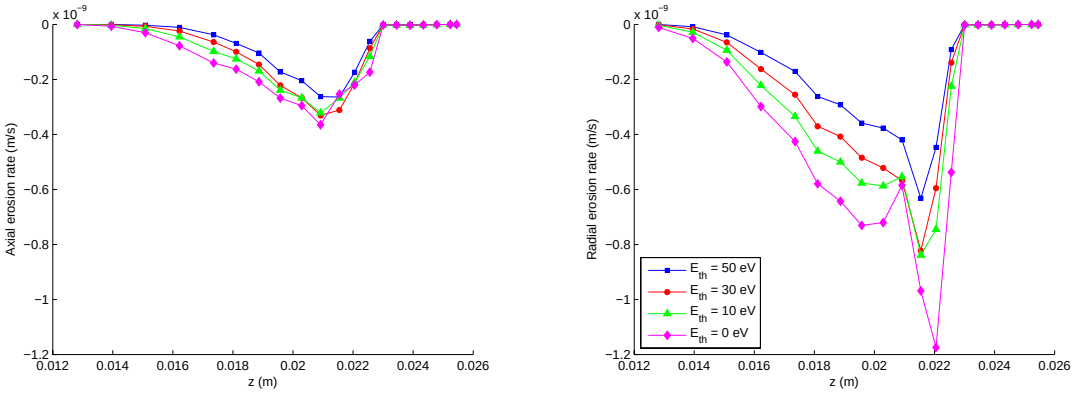

(a) Axial erosion rate.

(b) Radial erosion rate.

Figure 5-13: BHT-200: Wall erosion rates during 400-500 hour run – effect of sputter threshold.

Table 5.3: BHT-200: Simulated discharge current [A] – effect of sputter threshold. Nominal=0.8.

Run (hours)	E_{th}=50 eV	E_{th}=30 eV	E_{th}=10 eV	E_{th}=0 eV
0-100	0.794101	0.794101	0.794101	0.794101
100-200	0.789752	0.787871	0.785406	0.835736
200-300	0.787092	0.778351	0.799028	0.799475
300-400	0.780184	0.764635	0.776702	0.805050
400-500	0.769833	0.783355	0.773602	0.773833
Average	0.784192	0.781663	0.785768	0.801639

Table 5.4: BHT-200: Simulated thrust [mN] – effect of sputter threshold. Nominal=12.8.

Run (hours)	E_{th}=50 eV	E_{th}=30 eV	E_{th}=10 eV	E_{th}=0 eV
0-100	8.930	8.930	8.930	8.930
100-200	8.926	8.937	8.924	9.540
200-300	8.959	8.887	9.157	9.253
300-400	8.922	8.806	8.972	9.406
400-500	8.850	9.055	8.973	9.117
Average	8.917	8.923	8.991	9.249

In addition to matching the erosion profiles, it is also desirable to predict the nominal performance parameters. This study focuses on the discharge current, I_D, and thrust, T, which are averaged and summarized in Tables 5.3 and 5.4. Discharge current is matched fairly well while thrust is below nominal. Thrust tends to increase as sputter threshold decreases. This effect could be due to the widening of the thruster channel, allowing for a less constricted flow to expand more efficiently.

5.3.2 Effect of double ions

The next issue investigated is the effect of double ions – though composing only a small fraction of the plasma, their higher energies elevate their damaging potential and could contribute strongly to wall erosion. Figures 5-14 to 5-16 give the wall profile, profile deviation and net erosion history for cases with and without double ions. *HPHall* maintains the prescribed input voltage and mass flow rate – the addition of double ions is partially compensated by fewer single ions as ionizable neutrals and single ions now have the possibility of doubly ionizing. The effect of the double

ions is readily apparent in the increased amount of sputtering, particularly further downstream. By the time this zone is reached, ions have been accelerated through most of the thruster's potential gradient and arrive at the nose cone with maximum energy as confirmed by the 400-500 hour wall distributions of Figure 5-17. Again, as shown in Figure 5-18, the erosion rates track the energy distribution. To get a better sense of how detrimental double ions are, Figure 5-19 compares total ion with solely double ion flux. Double ions account for less than 10% of the wall particle flux, yet net erosion increases by a factor of $\sim$1.5-2 due to their presence. Thus, the influence of double ions is quite important and they are included in the remainder of the cases.

Discharge current and thrust comparisons are given in Tables 5.5 and 5.6. Addition of double ions leads to a general increase in both parameters.

Table 5.5: BHT-200: Simulated discharge current [A] – effect of double ions. Nominal=0.8.

Run (hours)	no double ions	with double ions
0-100	0.794101	0.866783
100-200	0.787871	0.865399
200-300	0.778351	0.861129
300-400	0.764635	0.803992
400-500	0.783355	0.811209
Average	0.781663	0.841702

Table 5.6: BHT-200: Simulated thrust [mN] – effect of double ions. Nominal=12.8.

Run (hours)	no double ions	with double ions
0-100	8.930	9.734
100-200	8.937	9.868
200-300	8.887	9.927
300-400	8.806	9.315
400-500	9.055	9.460
Average	8.923	9.661

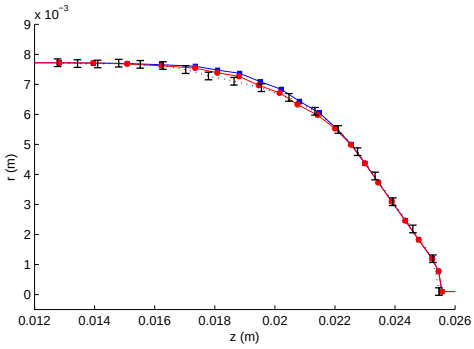

(a) 100 hours.

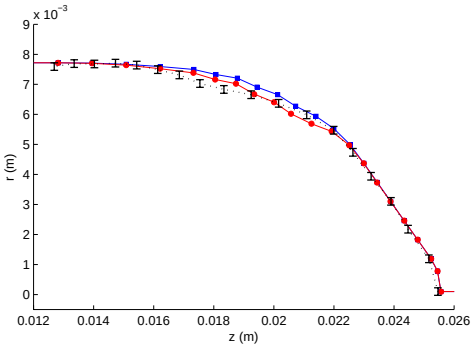

(b) 200 hours.

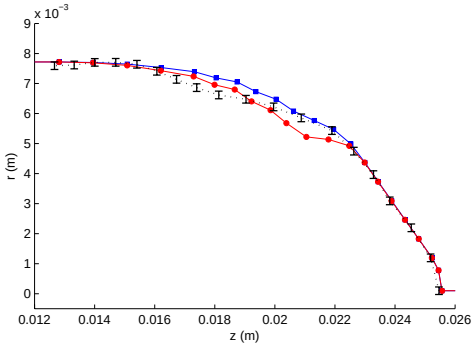

(c) 300 hours.

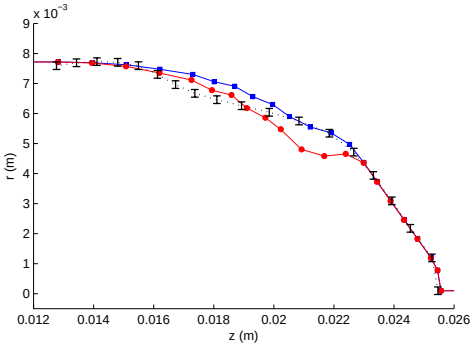

(d) 400 hours.

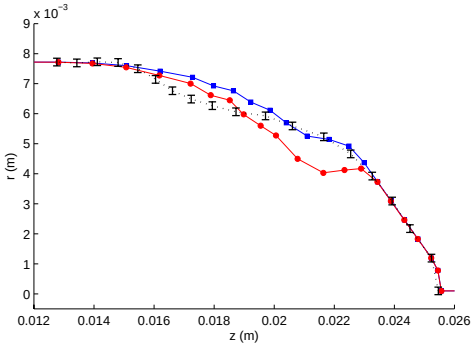

(e) 500 hours.

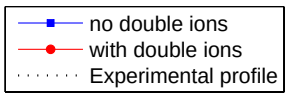

Figure 5-14: BHT-200: Erosion profile evolution – effect of double ions.

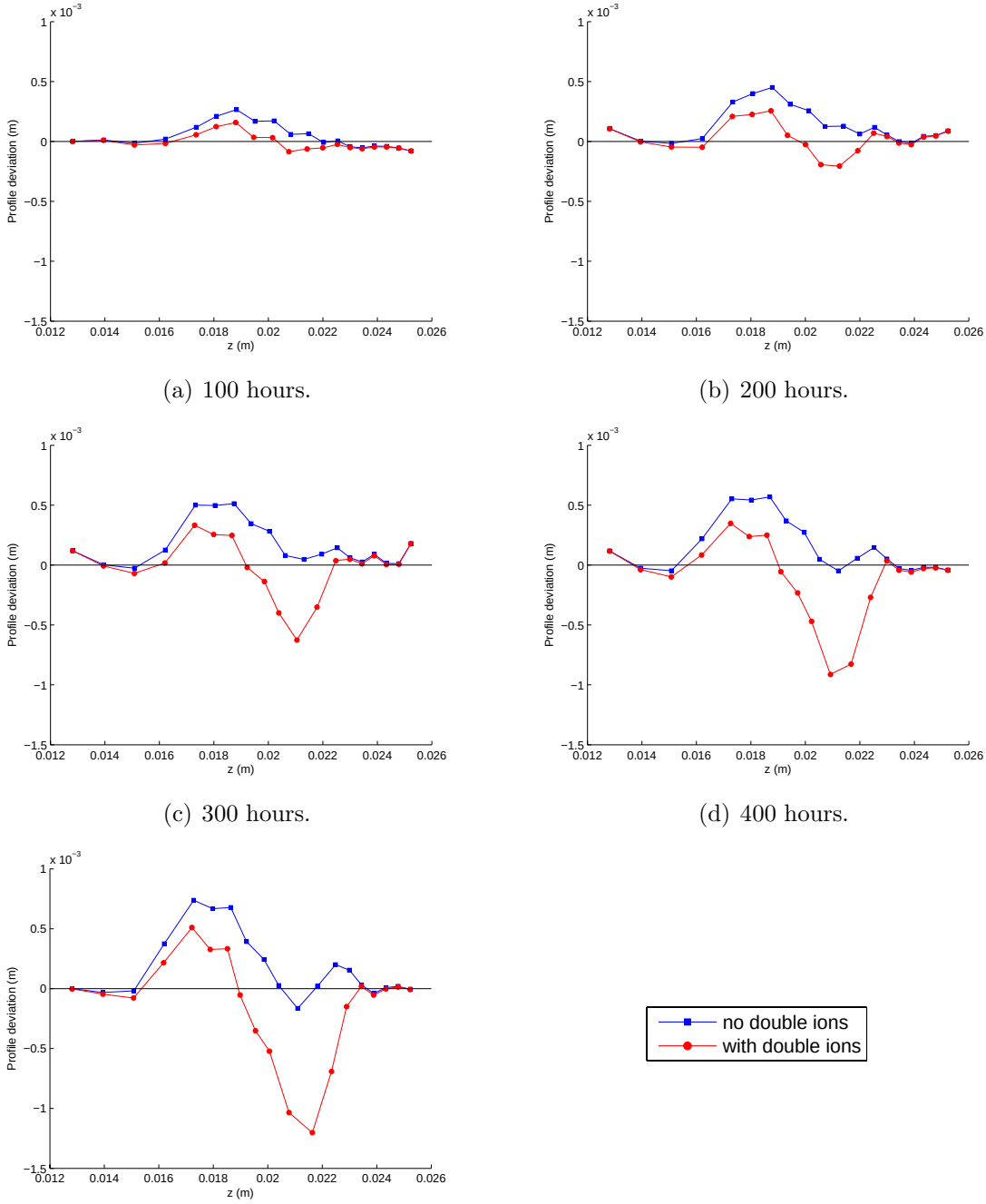

(a) 100 hours.

(b) 200 hours.

(c) 300 hours.

(d) 400 hours.

(e) 500 hours.

Figure 5-15: BHT-200: Erosion profile deviation – effect of double ions.

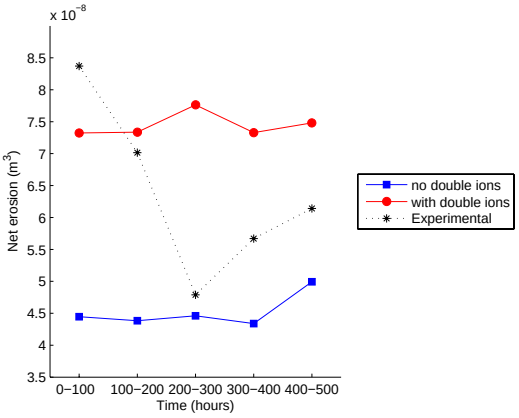

Figure 5-16: BHT-200: Net erosion – effect of double ions.

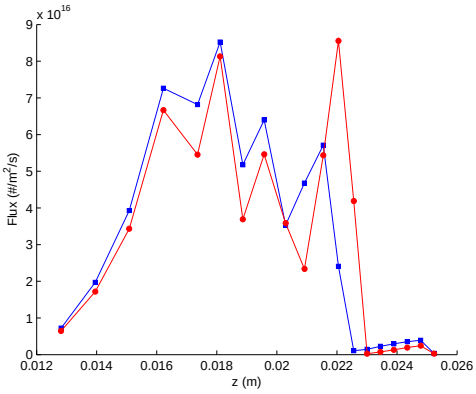

(a) Flux.

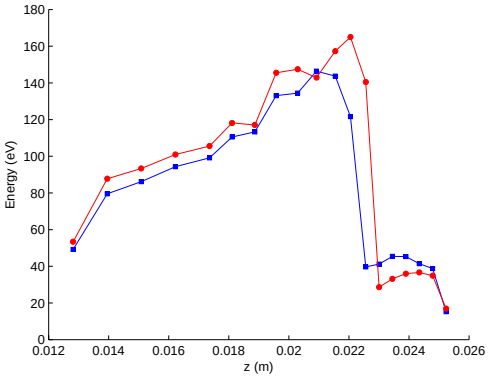

(b) Energy.

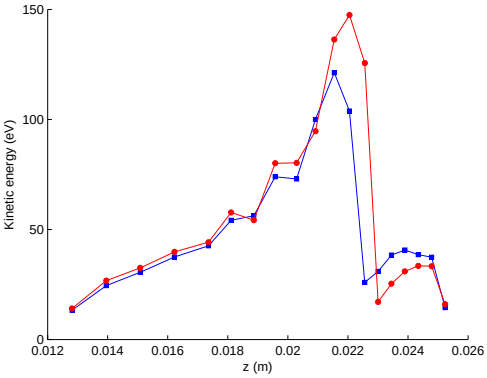

(c) Kinetic energy.

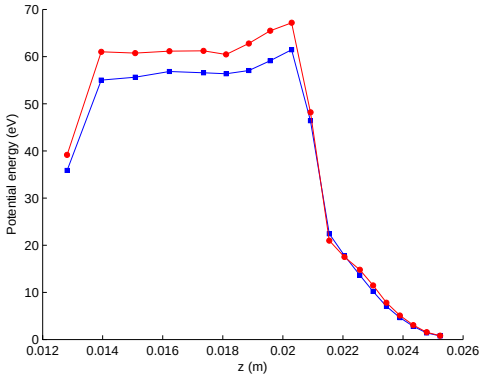

(d) Potential energy.

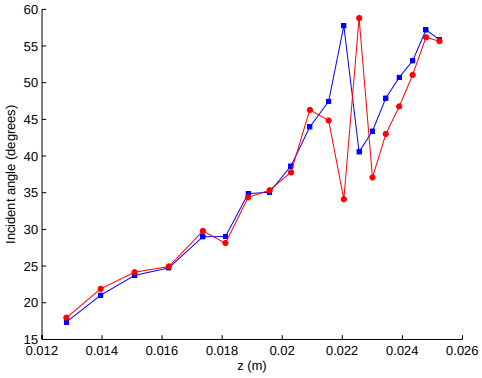

(e) Incident angle.

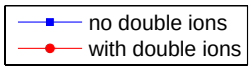

Figure 5-17: BHT-200: Averaged wall distributions during 400-500 hour run – effect of double ions.

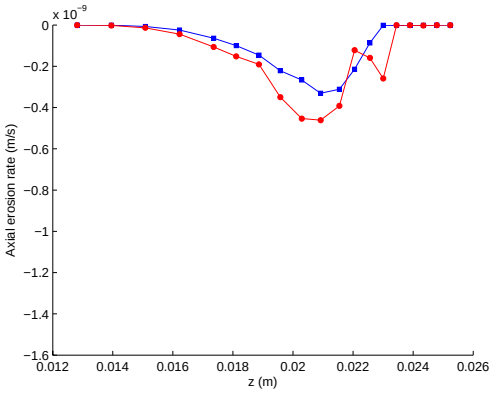

(a) Axial erosion rate.

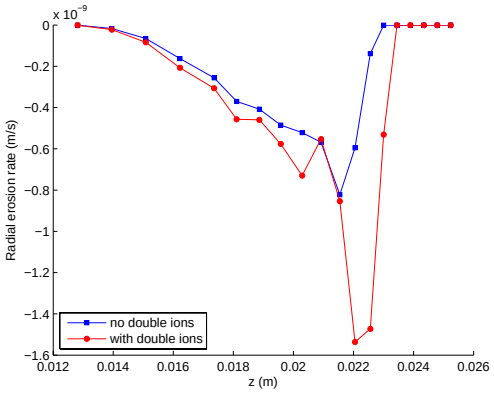

(b) Radial erosion rate.

Figure 5-18: BHT-200: Wall erosion rates during 400-500 hour run – effect of double ions.

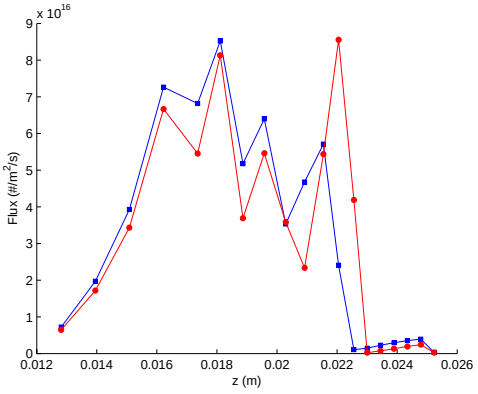

(a) Total ion flux.

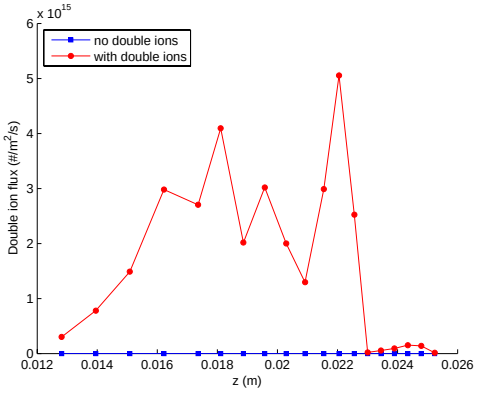

(b) Double ion flux.

Figure 5-19: BHT-200: Flux comparison – effect of double ions.

5.3.3 Effect of anomalous transport model

The anomalous transport model and its effect on the erosion profiles is the next matter studied. The double ion profiles portrayed in Figure 5-14 exhibit erosion of the correct order of magnitude, but the exact placement of the wear needs work as it is underpredicted in the mid-region and overpredicted in the downstream region. This discrepancy between the model and reality indicates that the plasma transport may not be captured properly.

Imposed transport barrier

As discussed in Section 4.2.6, imposing a transport barrier to affect the location of the simulated discharge has physical grounding and preliminary tests are run. The potential contour plots from a case with and without a transport barrier are compared in Figure 5-20. In the case with the transport barrier, the potential contours are narrower and pushed back into the acceleration channel. This behavior seems promising as the potential gradient is steepened further upstream, meaning ions will have gained more energy and thereby cause more erosion earlier.

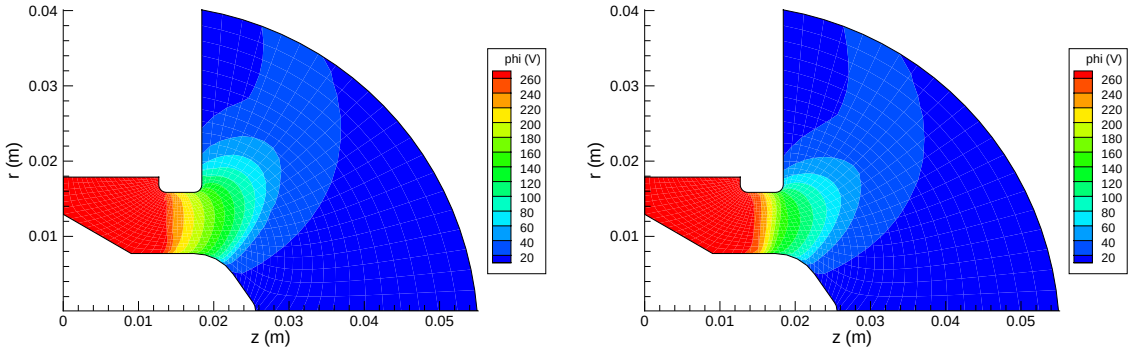

(a) Baseline case.

(b) With imposed transport barrier.

Figure 5-20: BHT-200: Potential comparison – effect of imposed transport barrier.

The exact positioning and thickness of the transport barrier is determined through trial and error. Following procedures taken by Fox [27] in using the same approach, a barrier is set at about 3/4 of the distance to the channel exit. Figure 5-21 shows the axial range of three test barriers.

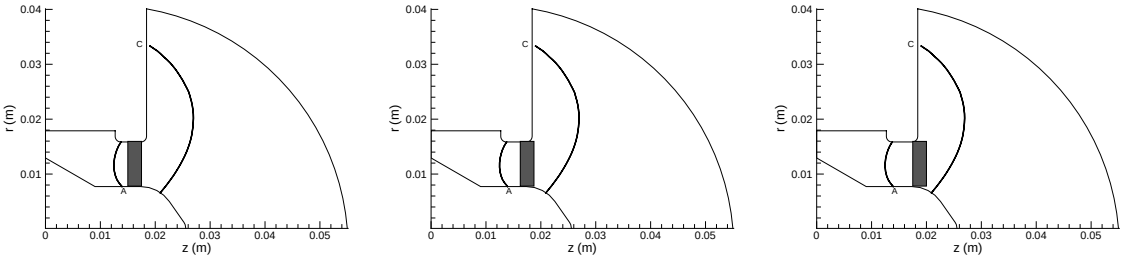

(a) Left, z = 0.015-0.0175 m. (b) Middle, z = 0.01625-0.01875 m. (c) Right, z = 0.0175-0.020 m.

Figure 5-21: BHT-200: Imposed transport barrier locations.

Figure 5-22 gives the erosion history for a baseline case with no barrier and for each of the transport barrier locations. In all cases with a barrier, the double ion effect is spread more evenly across the channel, bringing the simulated profiles to closer agreement with the experimental ones in the downstream region. The profile deviations of Figure 5-23 provide further proof of this improvement and as exhibited in Figure 5-24, the transport barriers further downstream reduce the net erosion. These observations are further corroborated in Figure 5-25 which shows that addition of a transport barrier shifts the peak erosion upstream while the overall wear rate level is lowered. The wall distributions plotted in Figure 5-26 again display a strong correlation between energy and erosion rate, though kinetic energy might provide a better match. The transport barriers also serve to flatten and decrease wall flux as well as push the potential energy peak further upstream.

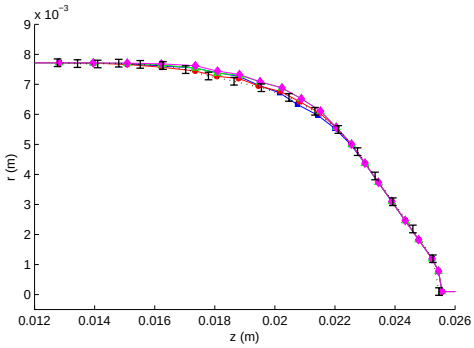

(a) 100 hours.

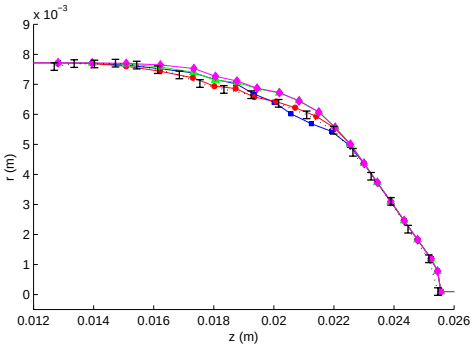

(b) 200 hours.

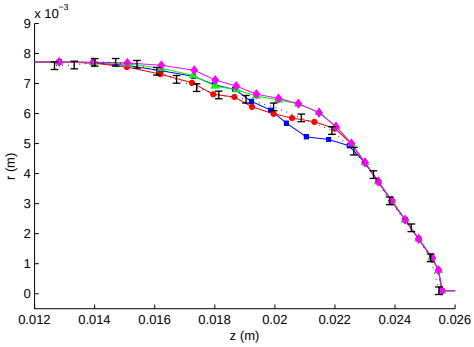

(c) 300 hours.

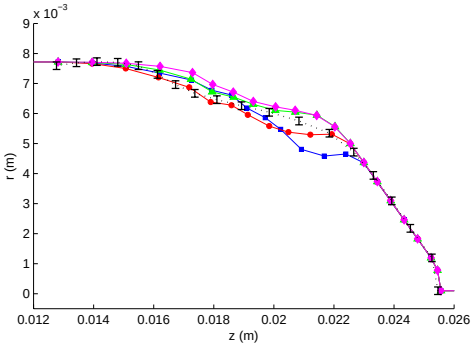

(d) 400 hours.

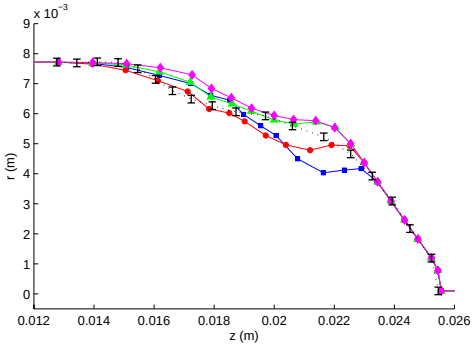

(e) 500 hours.

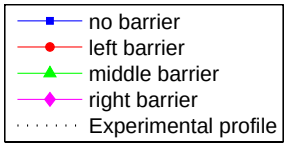

Figure 5-22: BHT-200: Erosion profile evolution – effect of transport barrier.

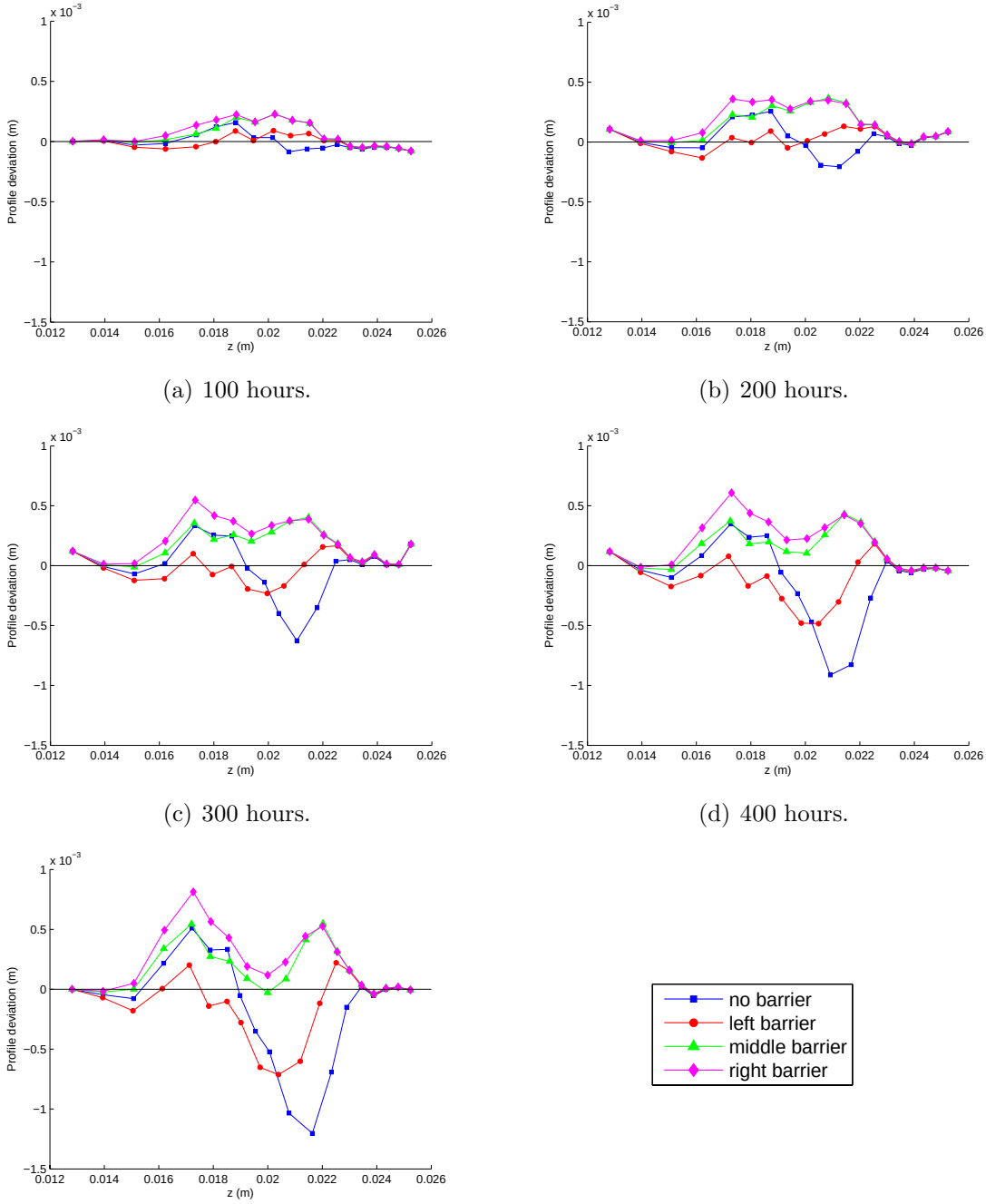

(a) 100 hours.

(b) 200 hours.

(c) 300 hours.

(d) 400 hours.

(e) 500 hours.

Figure 5-23: BHT-200: Erosion profile deviation – effect of transport barrier.

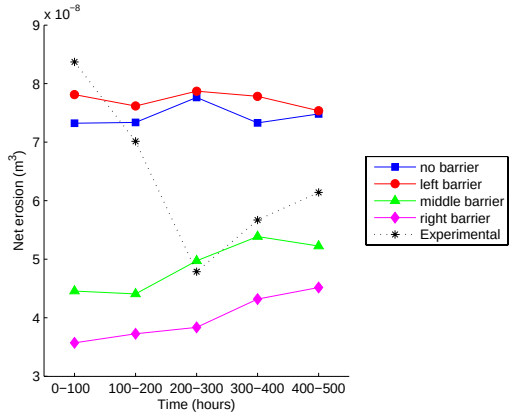

Figure 5-24: BHT-200: Net erosion – effect of transport barrier.

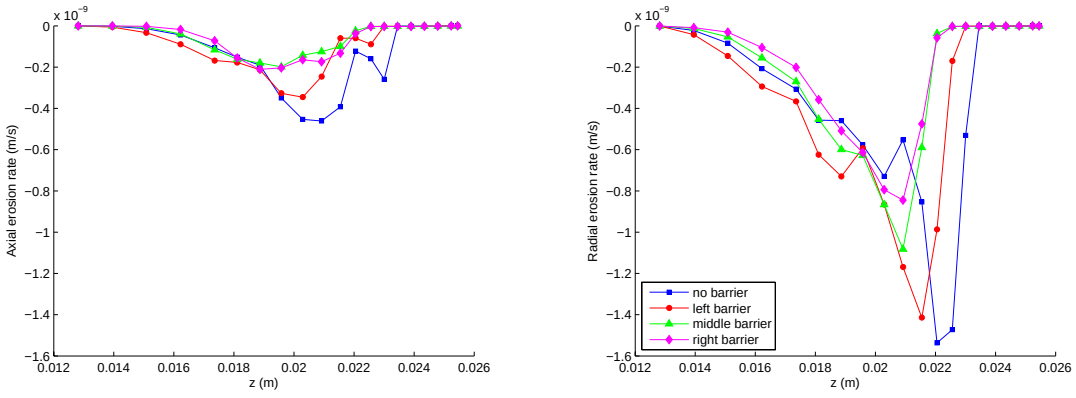

(a) Axial erosion rate.

(b) Radial erosion rate.

Figure 5-25: BHT-200: Wall erosion rates during 400-500 hour run – effect of transport barrier.

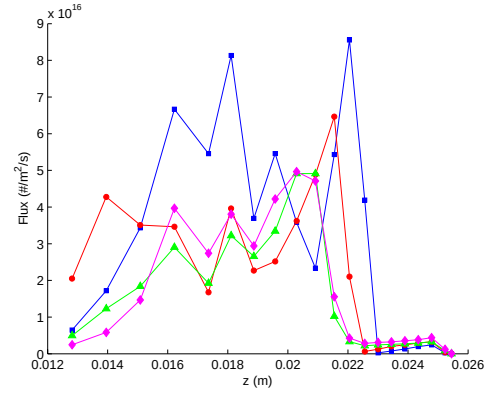

(a) Flux.

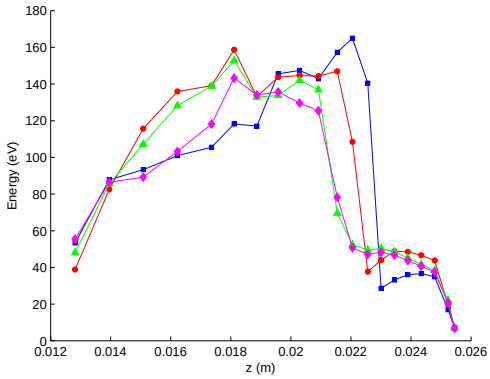

(b) Energy.

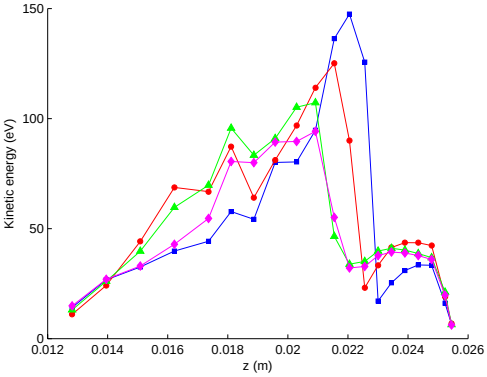

(c) Kinetic energy.

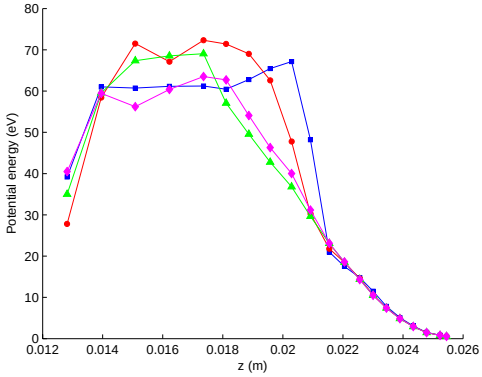

(d) Potential energy.

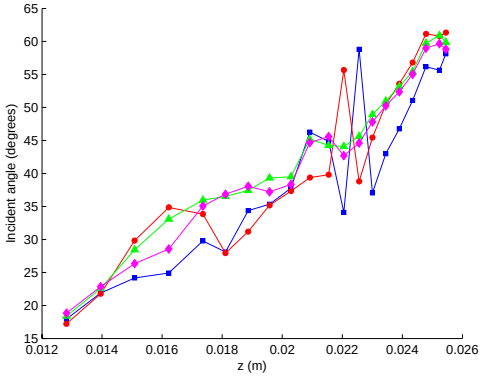

(e) Incident angle.

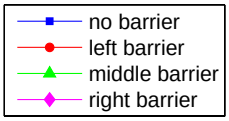

Figure 5-26: BHT-200: Averaged wall distributions during 400-500 hour run – effect of transport barrier.

Table 5.7: BHT-200: Simulated discharge current [A] – effect of transport barrier location. Nominal=0.8.

Run (hours)	none	left	middle	right
0-100	0.866783	0.731245	0.559663	0.500753
100-200	0.865399	0.715180	0.557753	0.513355
200-300	0.861129	0.707718	0.571630	0.501524
300-400	0.803992	0.689918	0.591512	0.524042
400-500	0.811209	0.689006	0.574120	0.524684
Average	0.841702	0.706613	0.570936	0.512872

Table 5.8: BHT-200: Simulated thrust [mN] – effect of transport barrier location. Nominal=12.8.

Run (hours)	none	left	middle	right
0-100	9.734	10.944	8.854	7.518
100-200	9.868	10.923	8.904	7.706
200-300	9.927	11.072	9.279	7.563
300-400	9.315	10.908	9.534	7.808
400-500	9.460	10.825	9.475	7.891
Average	9.661	10.934	9.209	7.697

Tables 5.7 and 5.8 give the performance parameters for each case. The position of the transport barrier greatly affects the simulated values – decreases in both discharge current and thrust are seen as the barrier is moved downstream. The left barrier provides results closest to nominal by suppressing discharge current while increasing thrust from the baseline no barrier case.

To understand better how the transport barrier affects the plasma discharge, Figure 5-27 compares the plasma density contour maps for all the cases. Addition of a barrier alters the shape and distribution of the plasma, but it is difficult to deduce how the nose cone will erode based on this bulk property. Figure 5-28 compares the electron temperature contour maps for all the cases. Addition of a barrier narrows the region of high electron temperature. The position of the barrier shifts the location and width of the region of peak temperature slightly. In Figure 5-29, the centerline plasma potential is plotted. As expected, the transport barrier drives the potential gradient upstream and ions approach their final velocity earlier in the channel. The flattened erosion profile may be the consequence of this shift. Because the residence

time of ions inside the thruster is decreased, less opportunity exists for ions to gain enough radial momentum to be driven into the walls and cause damage.

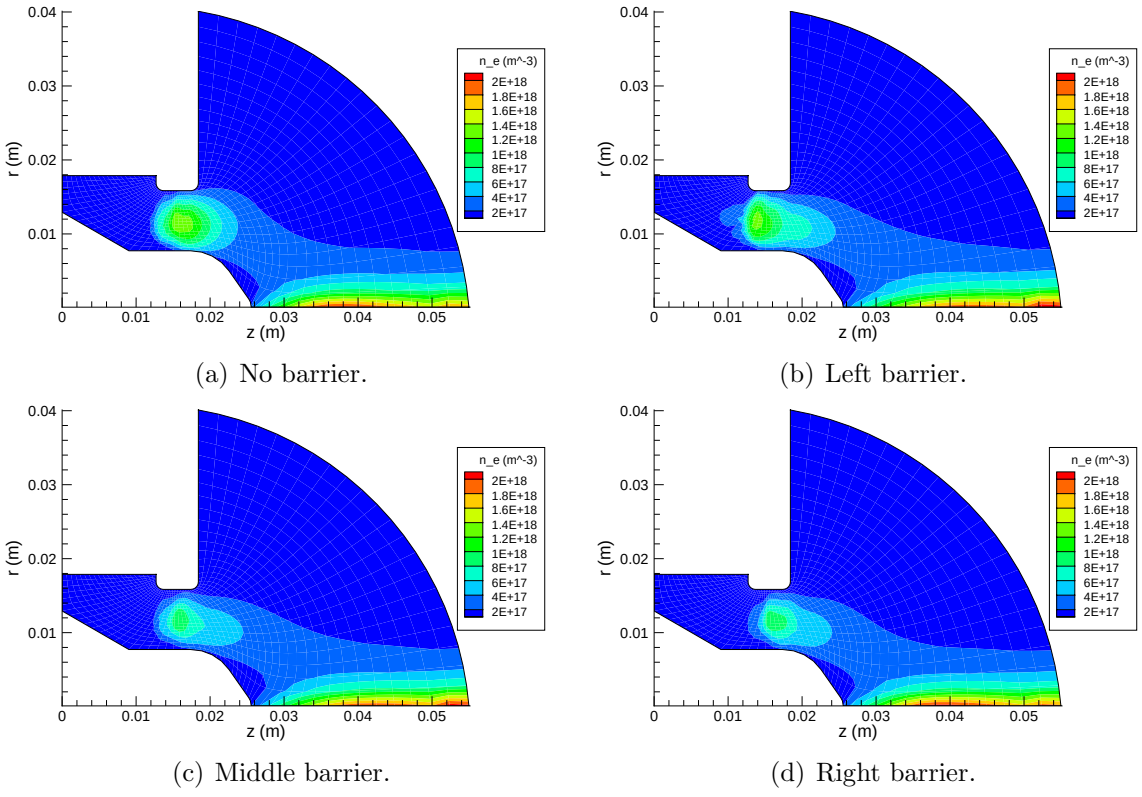

(a) No barrier.

(b) Left barrier.

(c) Middle barrier.

(d) Right barrier.

Figure 5-27: BHT-200: Plasma density – effect of transport barrier.

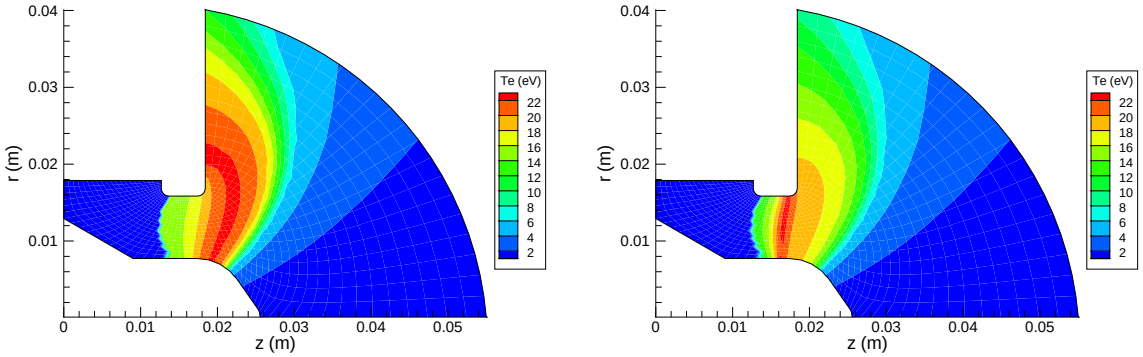

(a) No barrier.

(b) Left barrier.

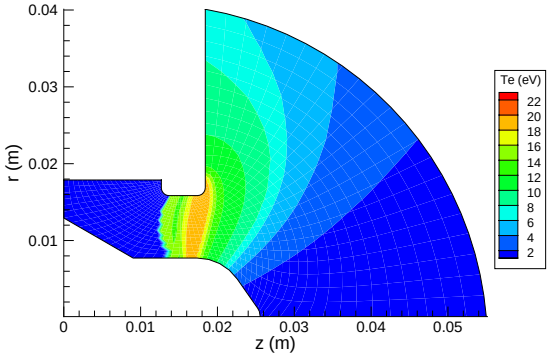

(c) Middle barrier.

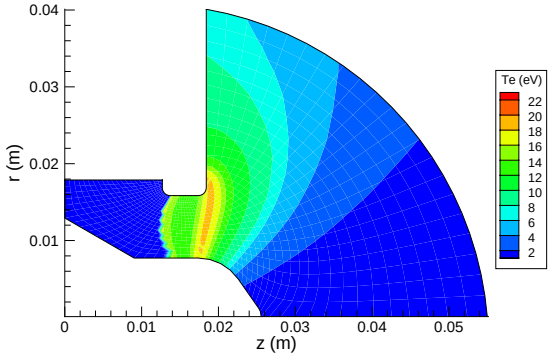

(d) Right barrier.

Figure 5-28: BHT-200: Electron temperature – effect of transport barrier.

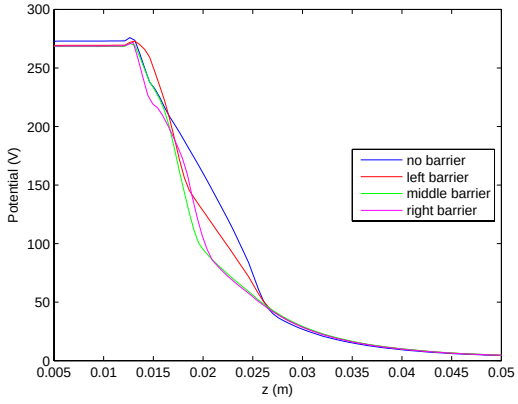

Figure 5-29: BHT-200: Centerline potential – effect of transport barrier.

Bohm coefficient

In an attempt to better match performance parameters, the Bohm coefficient is adjusted on the left transport barrier case. By increasing K_B from the baseline 0.15, transport outside the barrier is greater and should lead to a higher discharge current. Tables 5.9 and 5.10 summarize the performance parameter results. As expected, raising the value of K_B leads to higher discharge current as well as thrust. Based on performance alone, a K_B of 0.20 seems optimal. However, as seen in Figures 5-30 through 5-32, a greater Bohm coefficient leads to larger deviation from the experimentally measured erosion. Figure 5-33 shows higher peak erosion rates for increased K_B values while the wall distributions in Figure 5-34 exhibit slight increases in both flux and energy. Clearly, anomalous transport has a profound effect on the plasma and better understanding of the mechanisms that give rise to it is crucial for accurately simulating thruster performance and lifetime.

Table 5.9: BHT-200: Simulated discharge current [A] – effect of Bohm coefficient. Nominal=0.8.

Run (hours)	K_B=0.15	K_B=0.20	K_B=0.30
0-100	0.731245	0.791651	0.916661
100-200	0.715180	0.776927	0.884312
200-300	0.707718	0.761216	0.854324
300-400	0.689918	0.724370	0.840780
400-500	0.689006	0.744842	0.837817
Average	0.706613	0.759801	0.866771

Table 5.10: BHT-200: Simulated thrust [mN] – effect of Bohm coefficient. Nominal=12.8.

Run (hours)	K_B=0.15	K_B=0.20	K_B=0.30
0-100	10.944	11.183	11.715
100-200	10.923	11.310	11.869
200-300	11.072	11.218	11.870
300-400	10.908	11.008	11.747
400-500	10.825	11.108	11.669
Average	10.934	11.165	11.774

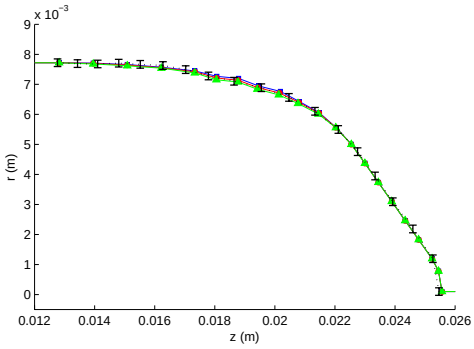

(a) 100 hours.

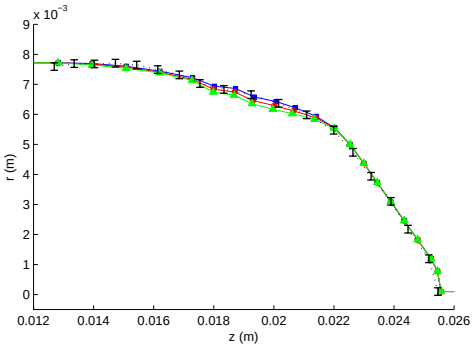

(b) 200 hours.

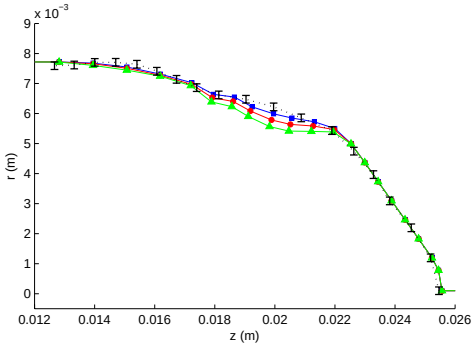

(c) 300 hours.

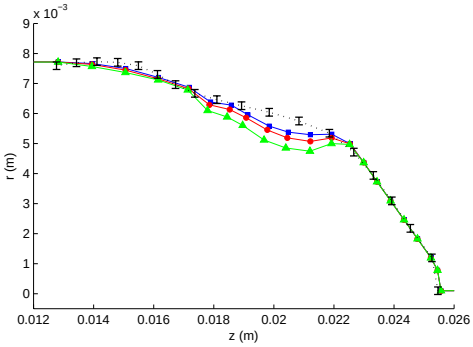

(d) 400 hours.

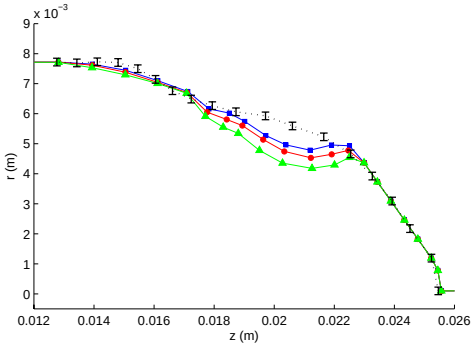

(e) 500 hours.

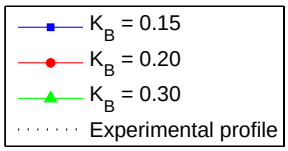

Figure 5-30: BHT-200: Erosion profile evolution – effect of Bohm coefficient.

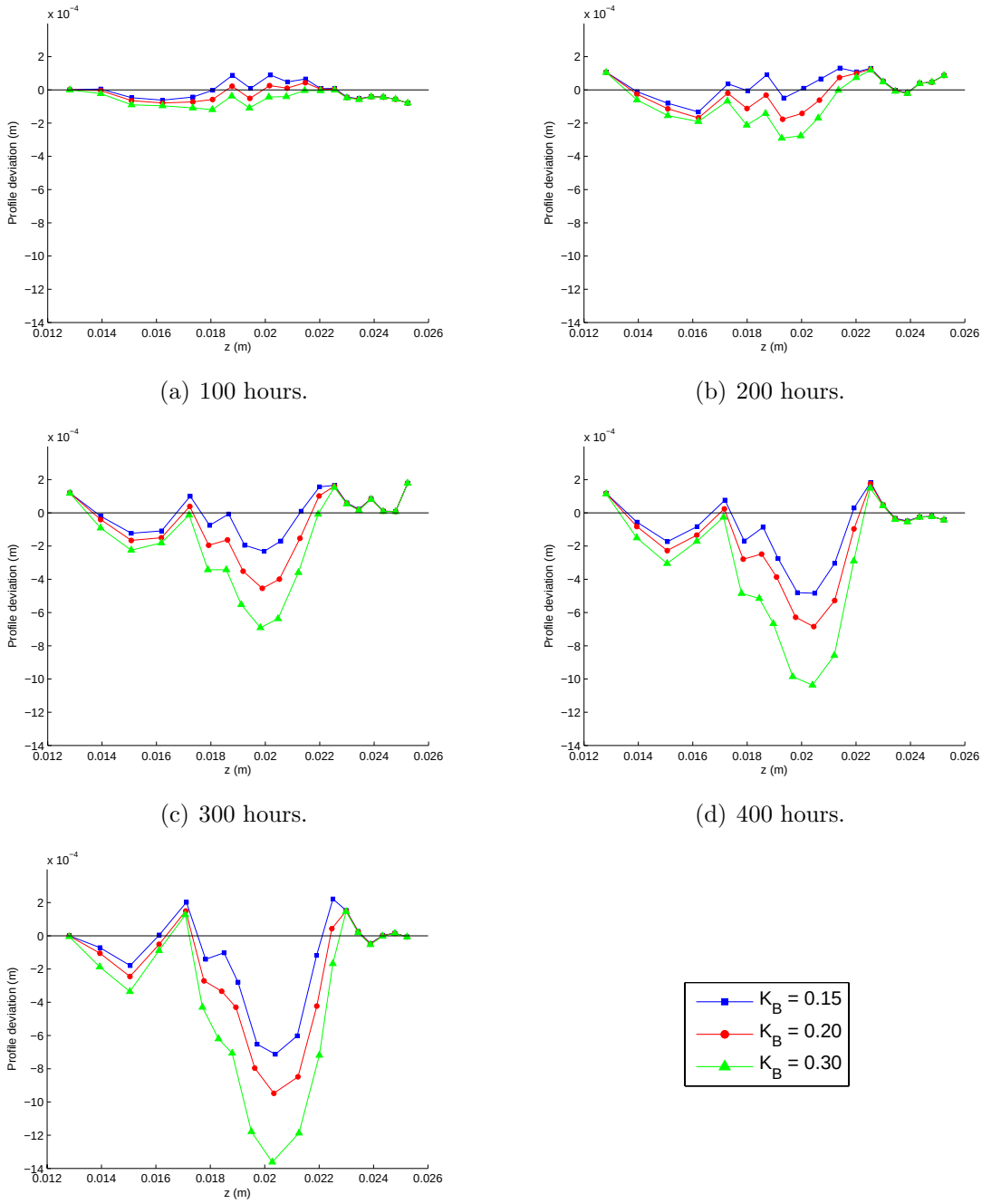

(a) 100 hours.

(b) 200 hours.

(c) 300 hours.

(d) 400 hours.

(e) 500 hours.

Figure 5-31: BHT-200: Erosion profile deviation – effect of Bohm coefficient.

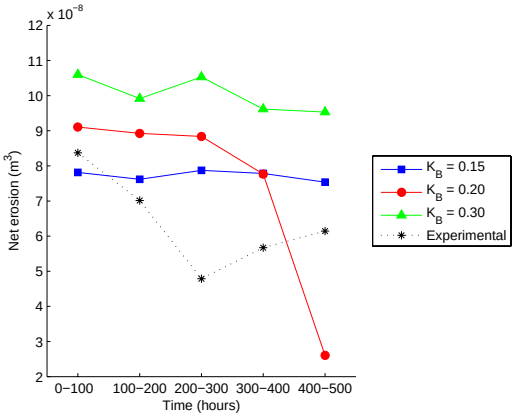

Figure 5-32: BHT-200: Net erosion – effect of Bohm coefficient.

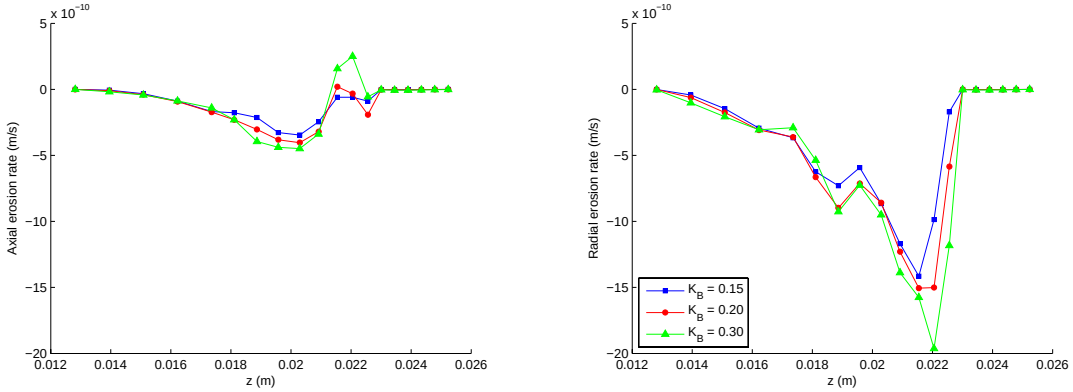

(a) Axial erosion rate.

(b) Radial erosion rate.

Figure 5-33: BHT-200: Wall erosion rates during 400-500 hour run – effect of Bohm coefficient.

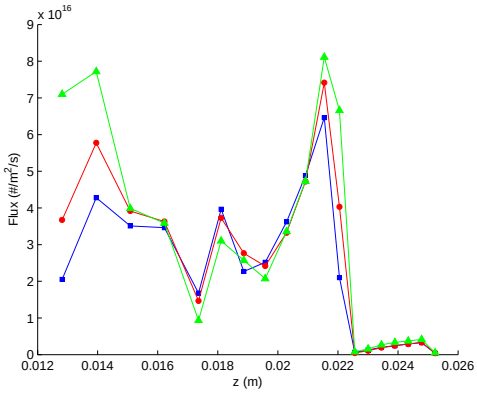

(a) Flux.

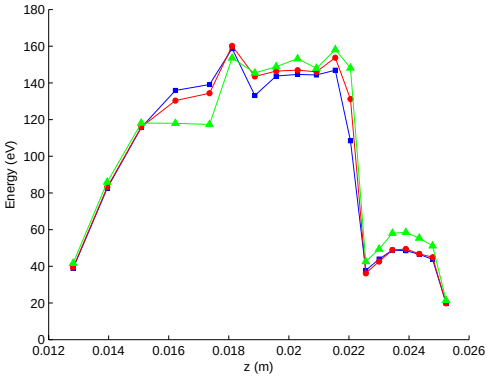

(b) Energy.

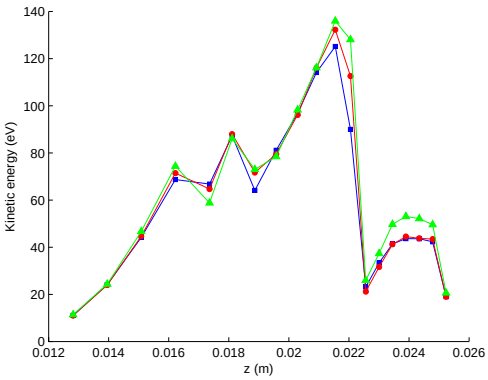

(c) Kinetic energy.

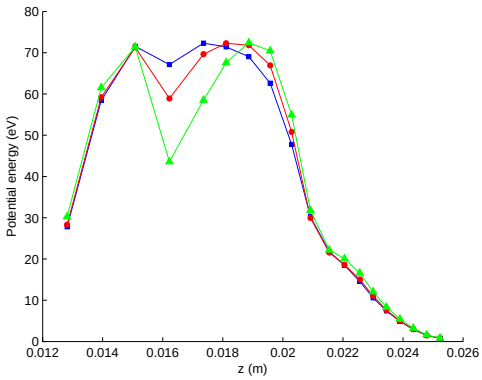

(d) Potential energy.

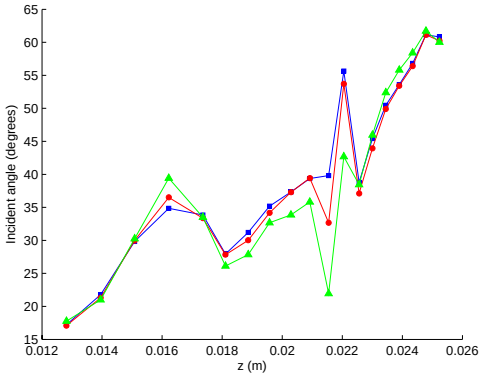

(e) Incident angle.

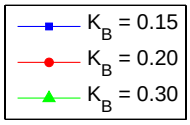

Figure 5-34: BHT-200: Averaged wall distributions during 400-500 hour run – effect of Bohm coefficient.

5.3.4 Note on cathode lambda line position

The cathode position is chosen to represent the physical location of the cathode. *HPHall* then integrates the electron equations between lambda lines representing the anode and the cathode. A requirement of the numerical scheme for solving the electron equations is that lines of the magnetic mesh must start on the bottom grid boundary and terminate at the upper one. Lambda lines begin at nodes along the bottom boundary and are traced through the domain until another grid boundary is reached. Those that end on the top edge are entered into consideration for the anode and cathode lines. From these candidates, the nearest lambda line to the specified anode or cathode location is selected to represent that component. In the grid generated to model the BHT-200, a lambda line of full span does not directly intersect the physical cathode position. Figure 5-35 shows the cathode location and the rightmost three lambda lines that satisfy the selection criteria. Thus, with the physical cathode location as input, the C1 lambda line is chosen as the cathode line and lies significantly closer to the acceleration region than the actual cathode. In this section, the role played by the cathode line position is explored – with the current mesh, the actual cathode cannot be approached any closer. Instead, the result of moving the cathode line further upstream is studied.

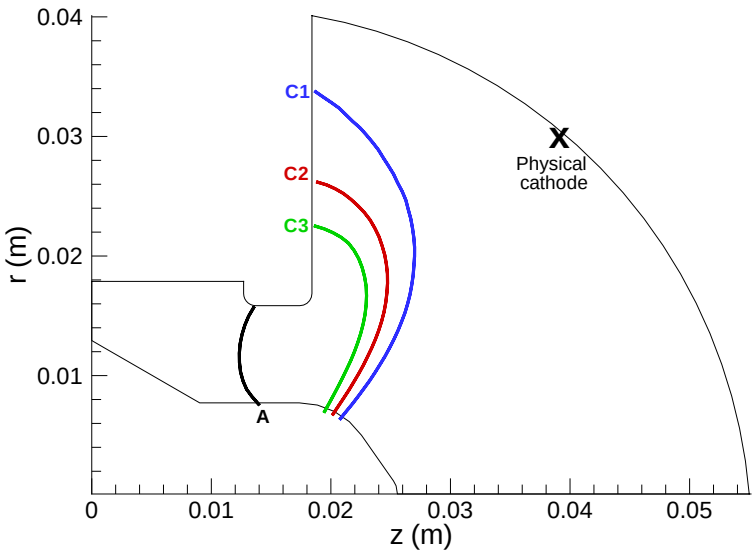

Figure 5-35: BHT-200 lambda lines.

Figures 5-36 to 5-38 give the erosion history for the different cathode line positions. The effect of bringing the cathode line nearer to the anode is similar to that witnessed by increasing the Bohm coefficient. This similarity in trend is also reflected in the erosion rates and wall distributions of Figures 5-39 and 5-40. It seems the cathode line location affects the plasma transport in a manner similar to the Bohm coefficient. If the mesh is regenerated such that the upper boundary is canted towards the cathode, it could be possible to obtain a valid magnetic line that passes through the physical cathode location. Based on the trends observed, a higher K_B would probably be needed to achieve similar results.

Tables 5.11 and 5.12 give the performance parameters for each of the cathode line cases. Bringing the cathode line closer to the acceleration channel increases the discharge current while no clear effect is witnessed in the thrust.

Table 5.11: BHT-200: Simulated discharge current [A] – effect of cathode line position. Nominal=0.8.

Run (hours)	C1	C2	C3
0-100	0.731245	0.737943	0.771178
100-200	0.715180	0.719525	0.748088
200-300	0.707718	0.732941	0.775992
300-400	0.689918	0.721764	0.756428
400-500	0.689006	0.720118	0.772237
Average	0.706613	0.726458	0.764785

Table 5.12: BHT-200: Simulated thrust [mN] – effect of cathode line position. Nominal=12.8.

Run (hours)	C1	C2	C3
0-100	10.944	10.850	10.932
100-200	10.923	10.824	10.897
200-300	11.072	10.841	10.844
300-400	10.908	10.820	10.776
400-500	10.825	10.928	10.883
Average	10.934	10.853	10.866

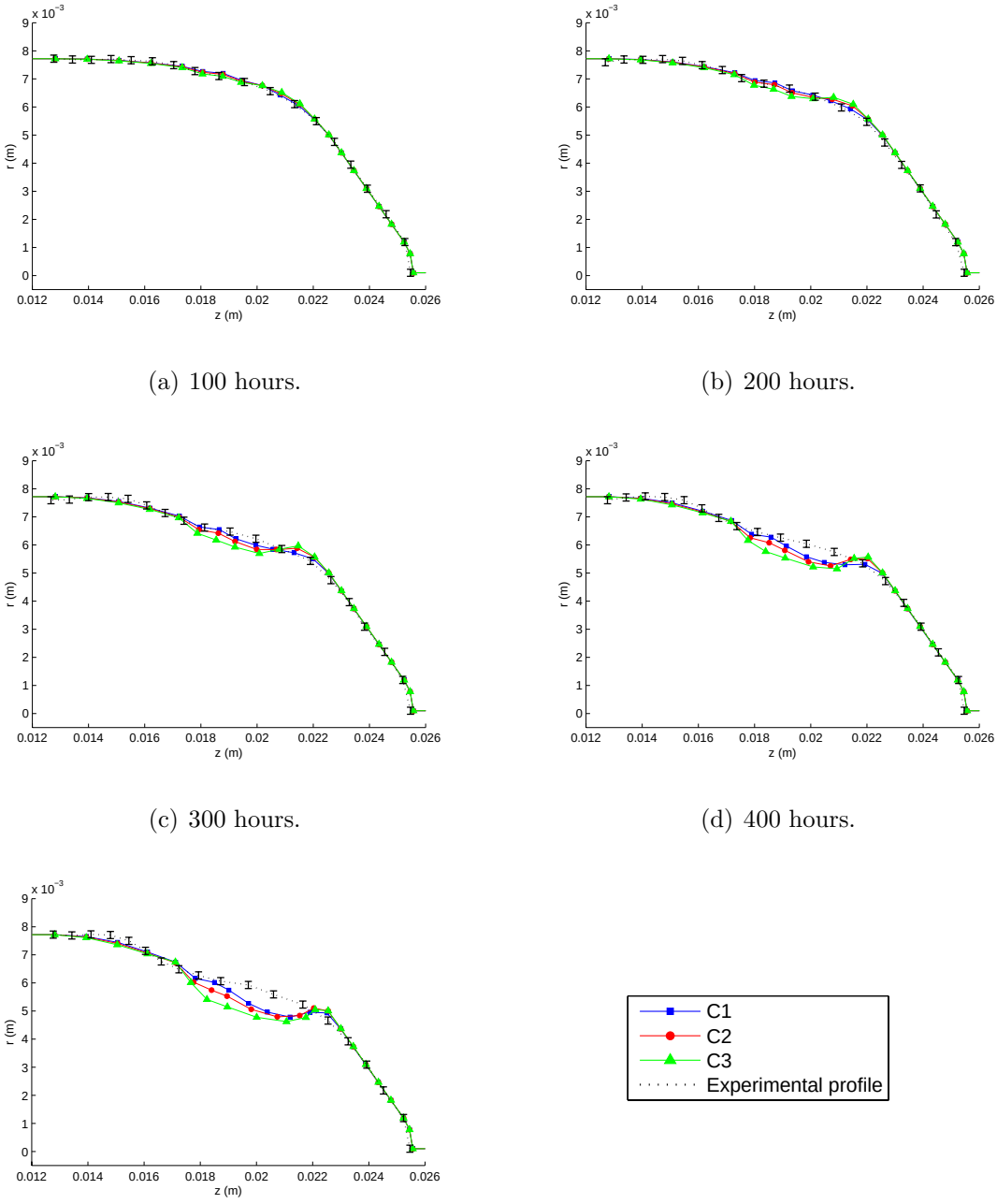

(a) 100 hours.

(b) 200 hours.

(c) 300 hours.

(d) 400 hours.

(e) 500 hours.

Figure 5-36: BHT-200: Erosion profile evolution – effect of cathode line position.

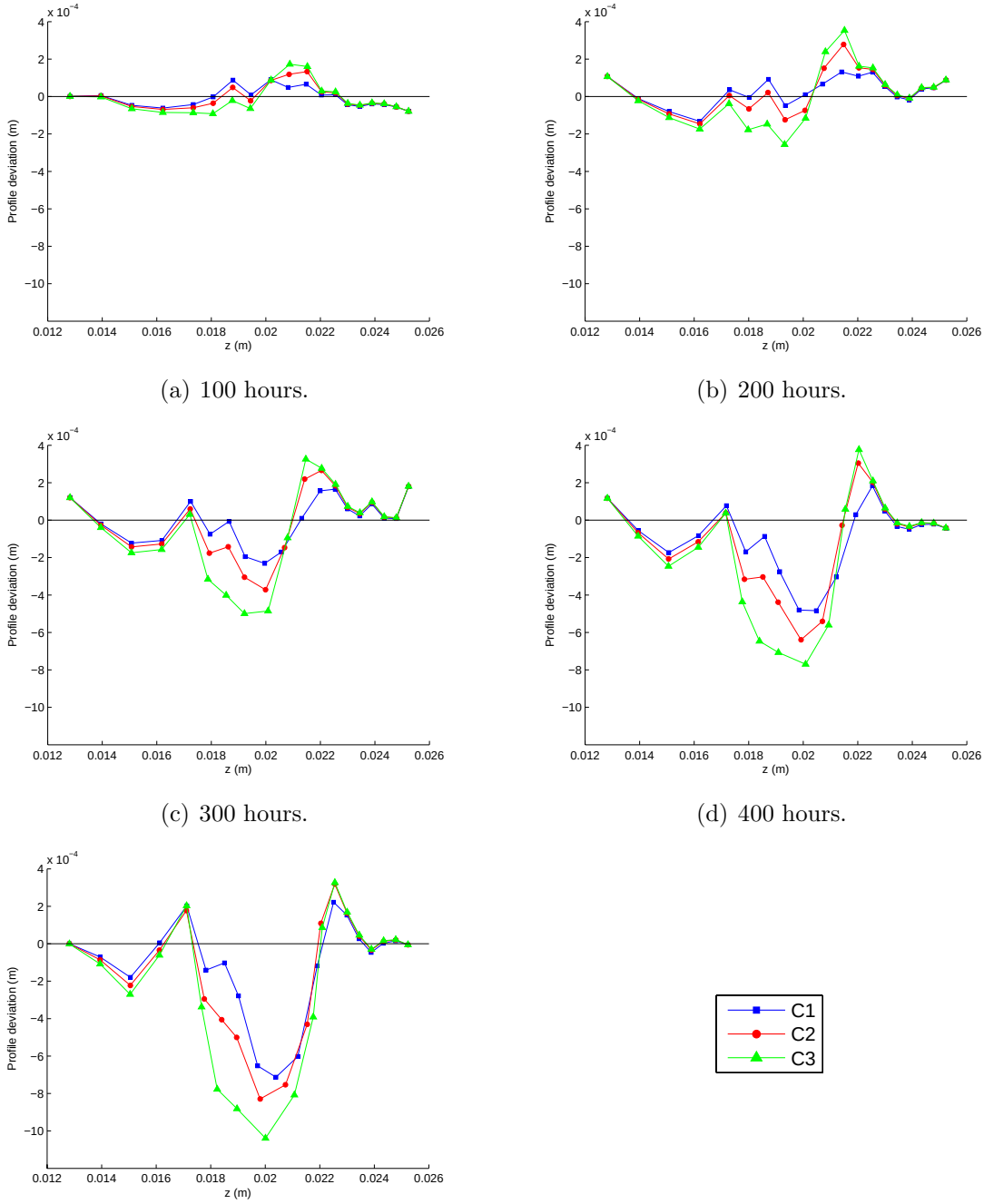

(a) 100 hours.

(b) 200 hours.

(c) 300 hours.

(d) 400 hours.

(e) 500 hours.

Figure 5-37: BHT-200: Erosion profile deviation – effect of cathode line position.

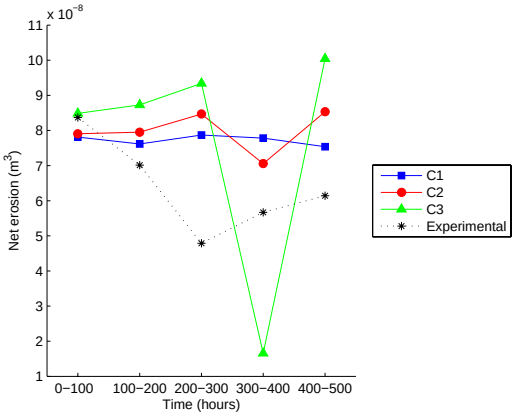

Figure 5-38: BHT-200: Net erosion – effect of cathode line position.

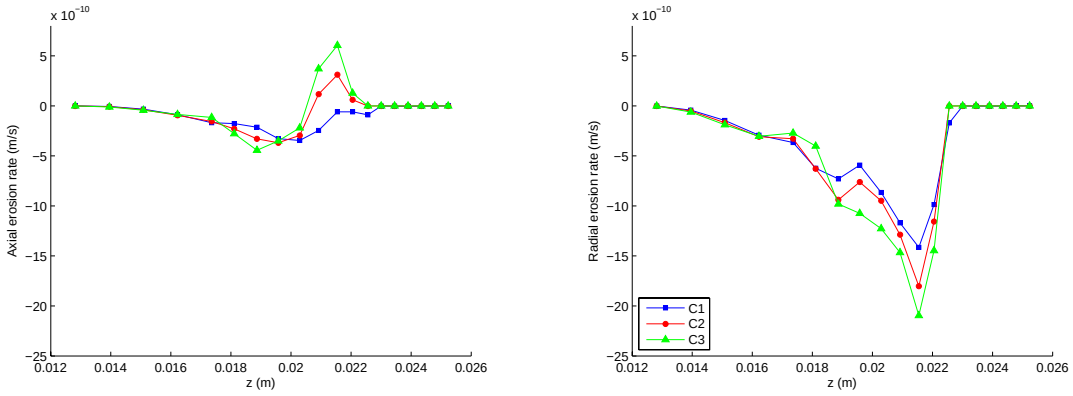

(a) Axial erosion rate.

(b) Radial erosion rate.

Figure 5-39: BHT-200: Wall erosion rates during 400-500 hour run – effect of cathode line position.

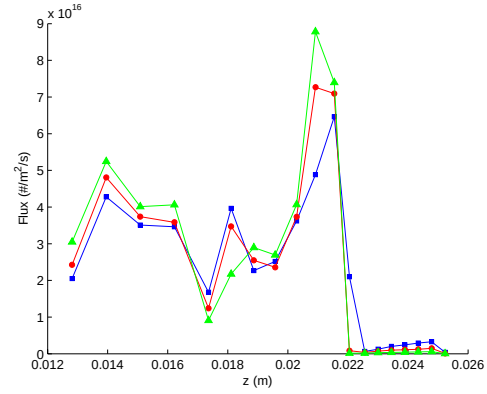

(a) Flux.

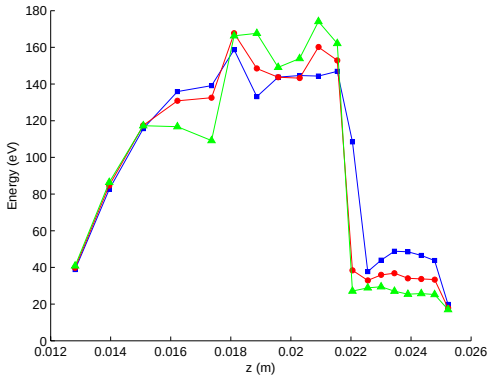

(b) Energy.

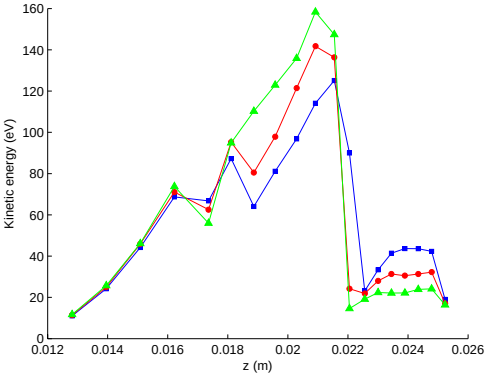

(c) Kinetic energy.

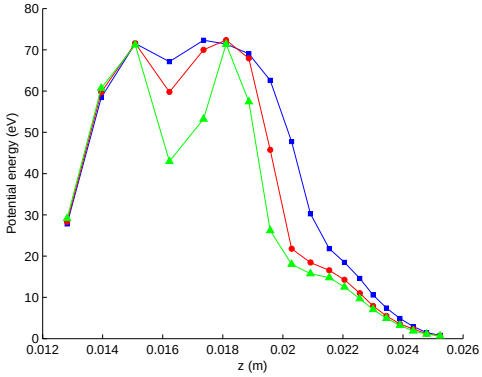

(d) Potential energy.

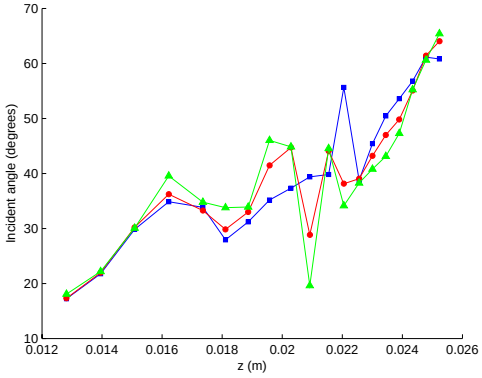

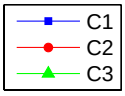

(e) Incident angle.

Figure 5-40: BHT-200: Averaged wall distributions during 400-500 hour run – effect of cathode line position.

Table 5.13: BHT-200 case parameters for long lifetime run.

E_{th}	30 eV
Double ions	Yes
Transport barrier	Left
K_B	0.15
Cathode line	C1

5.4 Lifetime prediction

The ultimate goal of being able to predict how the wall geometry evolves is to forecast when the thruster will fail. For the BHT-200, lifetime is declared over once the nose cone insulator is breached, exposing the center stem. Choosing a representative case to run past the 500 hours is difficult as a decision between good matching of erosion profiles or performance parameters needs to be made. The case that best matches the erosion profiles is selected and its attributes are summarized in Table 5.13.

Continuing from the accumulated 500 hours of simulated operation, the thruster is stepped in 100 hour increments until 900 cumulative hours are reached. Beyond 900 hours, the time step between runs is selected on a case-by-case basis to better capture the wall evolution, but never exceeds 100 hours. In total, 15 runs are carried out and the thruster first breaks through to the center stem at a time of 1,330 hours and at an axial location of $z \sim 0.01825$ m. Figure 5-41 shows the end of life profile.

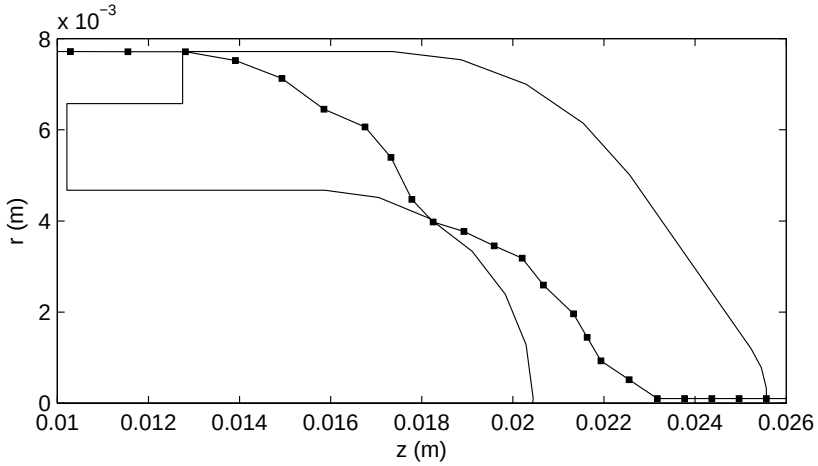

Figure 5-41: BHT-200 end of life profile (1,330 h).

The BHT-200 that underwent 500 hours of experimental life testing at Busek was subsequently sent to AFRL at Edwards for completion of the long duration test. In total, the thruster was run for 1700+ hours before the test was voluntarily terminated. Unfortunately, the experiment was not interrupted to take erosion profiles at intermediate times and there is no further data to compare to. However, visual observations made of the nose cone tip falling off brackets the insulator breach as occuring between 1,287 and 1,519 hours of thruster firing, putting the simulated lifetime of 1,330 hours in the correct range.

The simulated evolution of the thruster's wall profile over time is given in Figure 5-42. During the first 500 hours of operation, the erosion is concentrated in the mid-region of the nose cone which is also observed experimentally. As time continues, the disappearance of this material gradually exposes more of the nose cone tip to the plasma and this area begins to show evidence of wear. By the time it reaches end of life, the thruster's nose cone has receded significantly.

Figures 5-43 and 5-44 show how the distributions of flux and energy to the wall evolve over the thruster's life. Again, the eventual exposure of the nose cone tip to the plasma is recognized as the flux goes from virtually nothing to heavy bombardment in this region over the course of the test. The energy maps show that initially, the occasional ion to reach the downstream section comes from the low tail of the energy distribution. As the tip comes into greater view of the discharge, energies representative of the bulk plasma are witnessed, contributing to the greater erosion in this locale. The result of these observations is reflected in Figures 5-45 and 5-46 which display the evolution of the wall erosion rates. As time elapses, the peak erosion for both components of the rate moves downstream. The magnitude of the erosion peak is also seen to increase as it travels towards the exit – this phenomenon is an indicator of the plasma's energy gain as it accelerates out of the channel. It should be noted that though erosion rates in the upstream section of the channel remain relatively constant throughout the thruster's operation, those downstream undergo drastic changes from beginning to end of life.

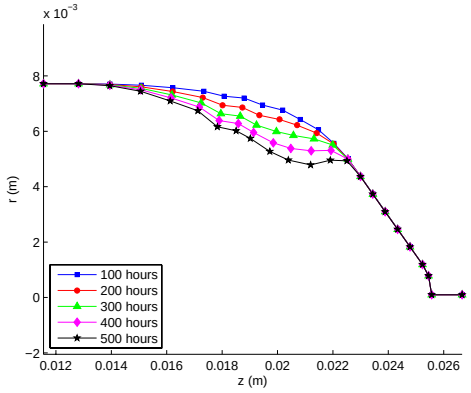

(a) 0-500 hours.

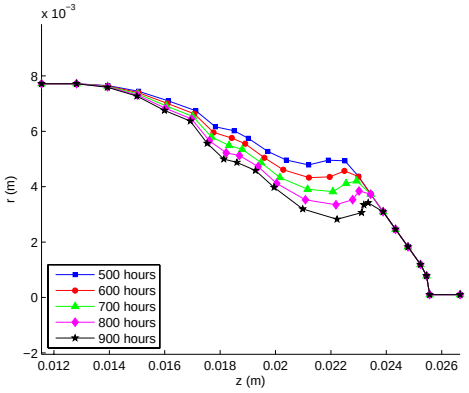

(b) 500-900 hours.

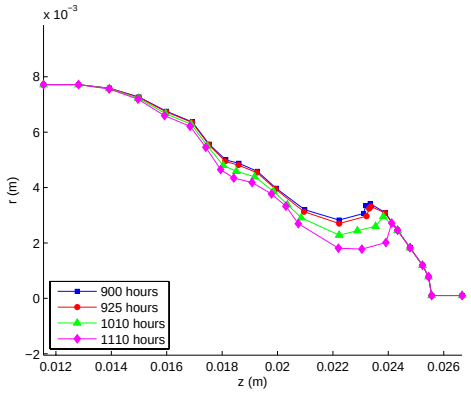

(c) 900-1,110 hours.

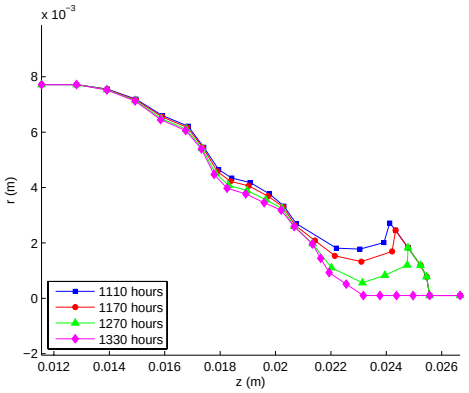

(d) 1,110-1,330 hours.

Figure 5-42: BHT-200: Erosion profile evolution.

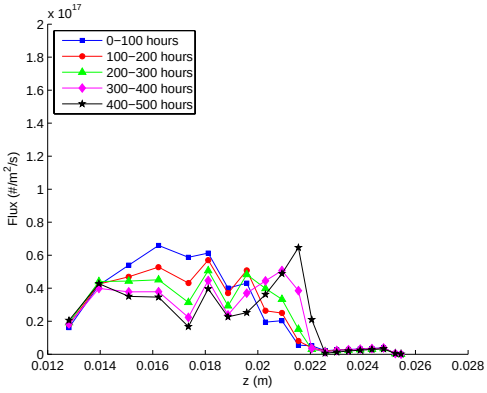

(a) 0-500 hours.

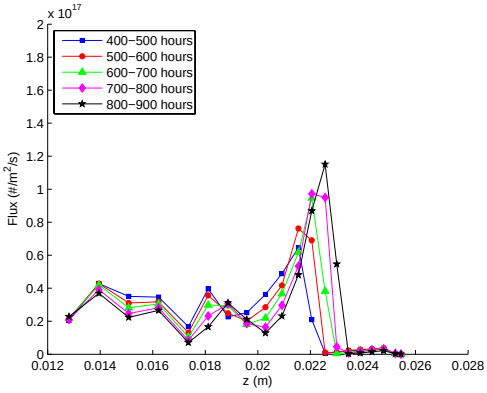

(b) 400-900 hours.

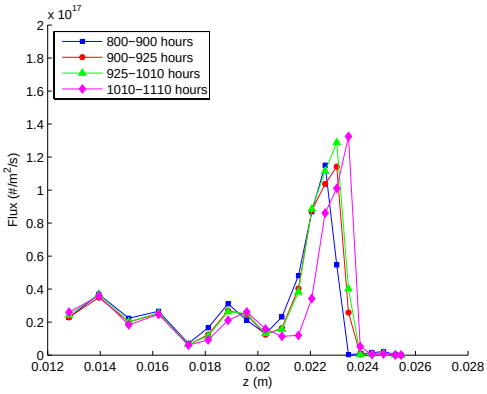

(c) 800-1,110 hours.

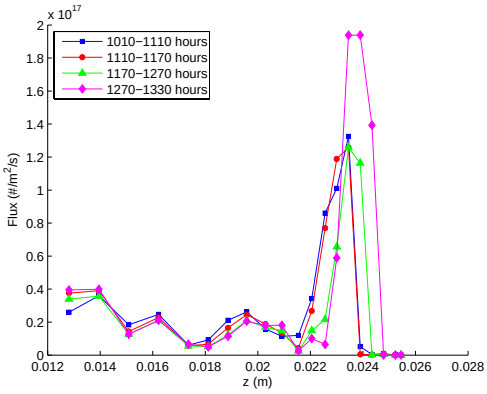

(d) 1,010-1,330 hours.

Figure 5-43: BHT-200: Flux evolution.

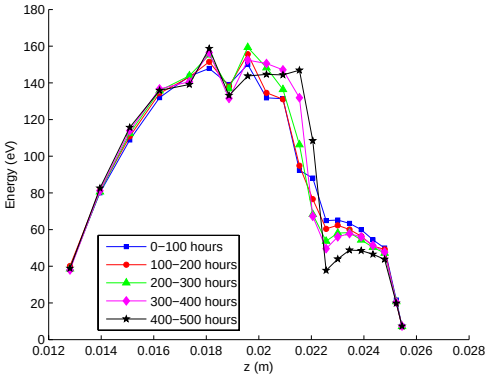

(a) 0-500 hours.

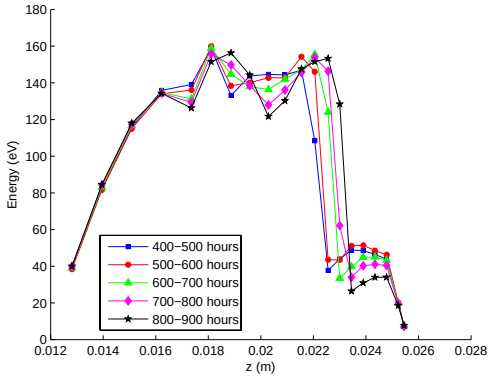

(b) 400-900 hours.

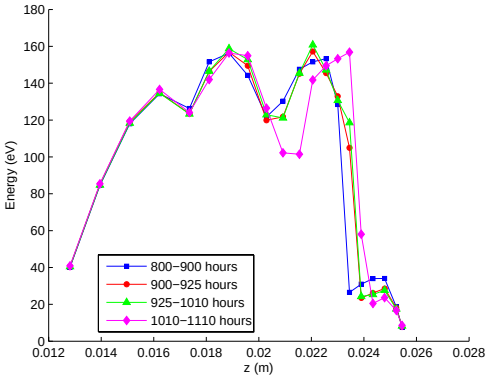

(c) 800-1,110 hours.

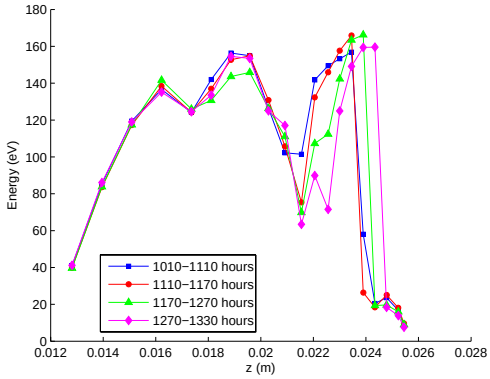

(d) 1,010-1,330 hours.

Figure 5-44: BHT-200: Energy evolution.

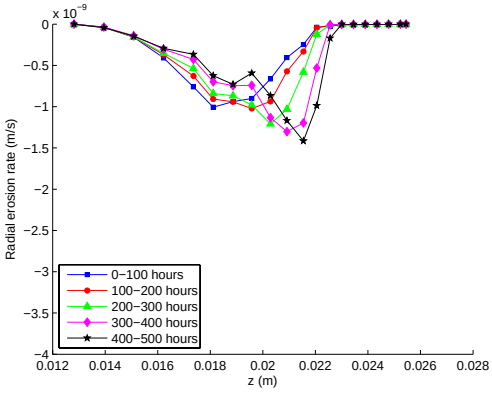

(a) 0-500 hours.

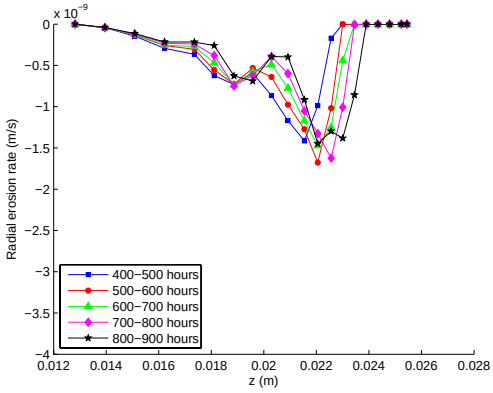

(b) 400-900 hours.

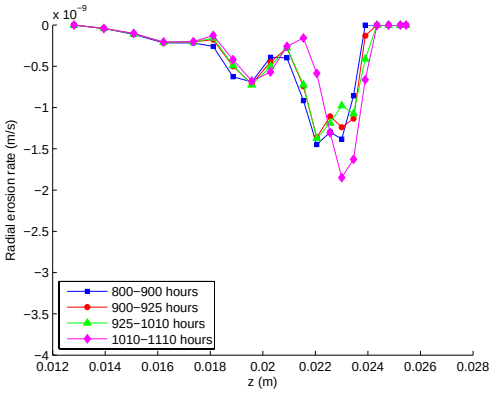

(c) 800-1,110 hours.

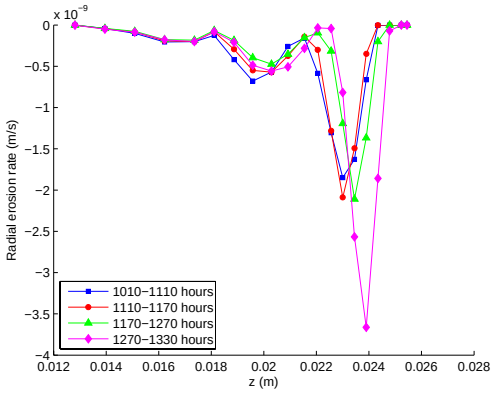

(d) 1,010-1,330 hours.

Figure 5-45: BHT-200: Radial erosion rate evolution.

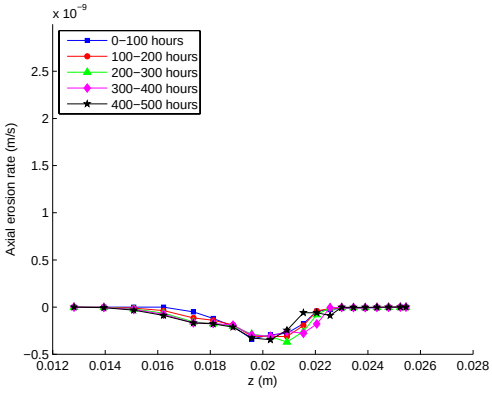

(a) 0-500 hours.

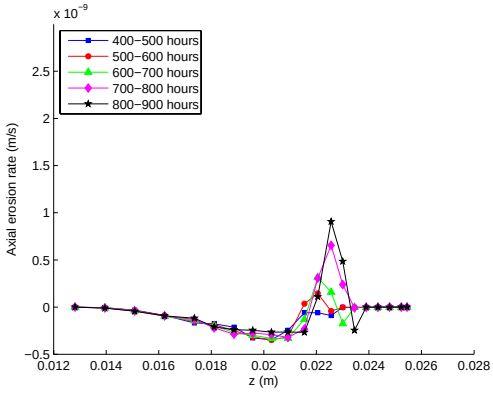

(b) 400-900 hours.

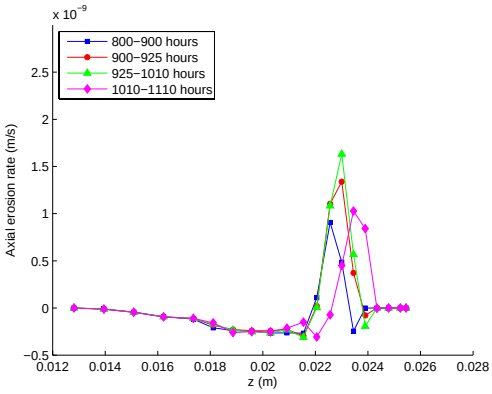

(c) 800-1,110 hours.

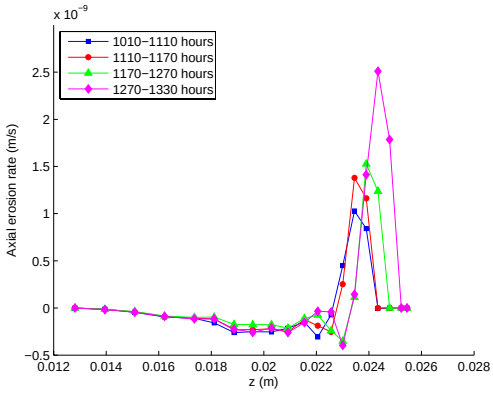

(d) 1,010-1,330 hours.

Figure 5-46: BHT-200: Axial erosion rate evolution.

The observation that the wall erosion rates are time-dependent has the implication that predicting the terminal profile based on rate measurements from the start of thruster life may not give correct extrapolations across the entire channel. Figure 5-47 compares projected wall profiles at 1,330 h when erosion rates used from 500 h and 1,270 h are used. The two projections give quite different views on the thruster state at this point. At 1,330 hours, the projection from 500 h has already broken through the nose cone to the center stem and the thruster end of life (EOL) would have been earlier. Furthermore, the location of the breach would have been further downstream and the effect of gradually exposing the tip to the plasma is not captured as it remains uneroded. Thus, caution should be taken when using data from beginning of life (BOL) to make future predictions. The specific thruster geometry undoubtedly plays an important role in this complex issue. However, it appears that use of a properly tuned code to BOL erosion profiles can predict the EOL geometry with reasonable confidence.

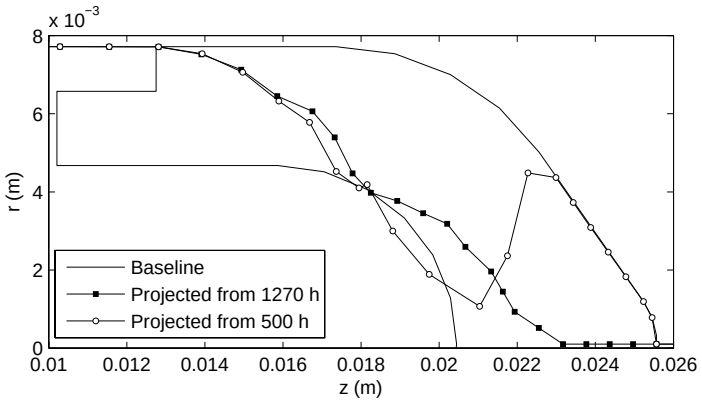

Figure 5-47: BHT-200 projected end of life profiles (1,330 h).

Figure 5-48 plots the simulated performance over the thruster's life. The discharge current is seen to decrease initially and then stabilize whereas the thrust exhibits no obvious trend. Both parameters are below the experimentally-measured values – this case was chosen for the virtual life test because of its good erosion profile agreement rather than performance.

Figure 5-49 shows energy distributions for selected wall panels during the first 100 hours of the virtual life test. The average energy of ions striking the panel at

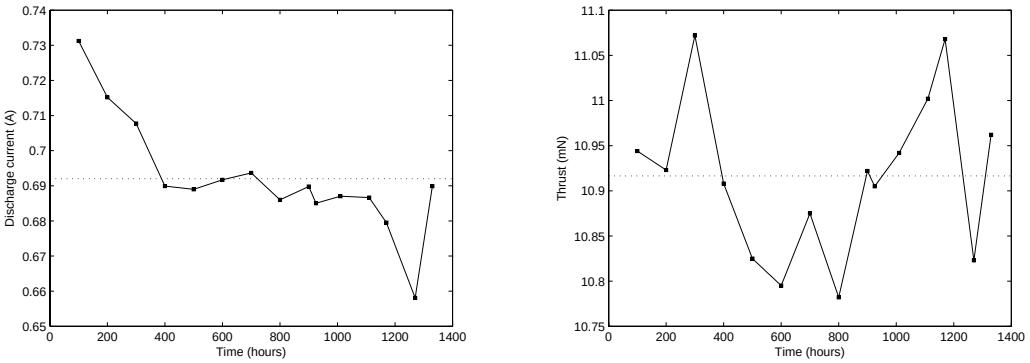

(a) Discharge current, nominal=0.8 A. (b) Thrust, nominal=12.8 mN.

Figure 5-48: BHT-200 simulated performance over lifetime. Average marked with dashed line.

each iteration is tracked and these values from the 20,000 iteration run are then used to generate the energy histograms. Regardless of location, all distributions exhibit a non-Maxwellian structure with a high-energy tail. The consequence of these non-equilibrated distributions is that information is lost if averaged descriptions of wall energies are used. Thus, tracking particles and their individual contribution to the wall erosion is needed for accurate description of the phenomenon. Figure 5-50 shows the energy distribution over time of Panel 26, located on the nose cone's mid-region. The distribution remains similar during the course of the thruster's life and one would be tempted to take an average one to represent the plasma as temporally constant. However, as Figure 5-51 shows, the energy distribution at Panel 35, located on the nose cone tip, exhibits a different character as this region is gradually exposed to the bulk plasma. These observations reinforce the idea that assuming initial erosion behavior will not change is dangerous and the full life span of the thruster should be modeled.

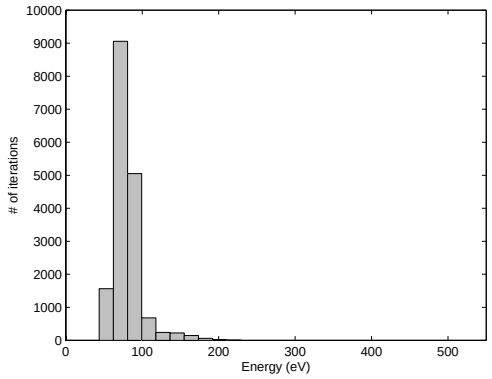

(a) Panel 20.

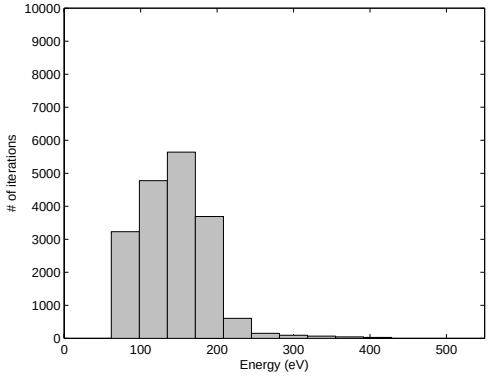

(b) Panel 23.

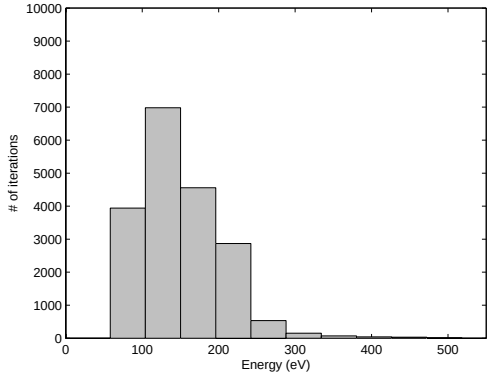

(c) Panel 26.

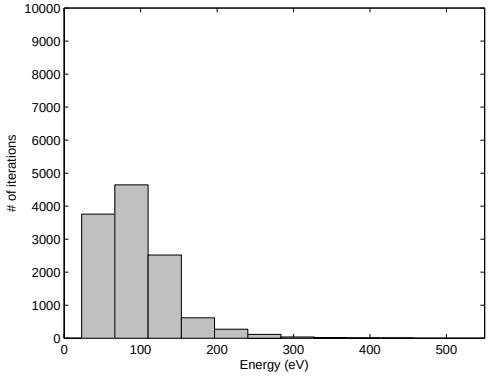

(d) Panel 29.

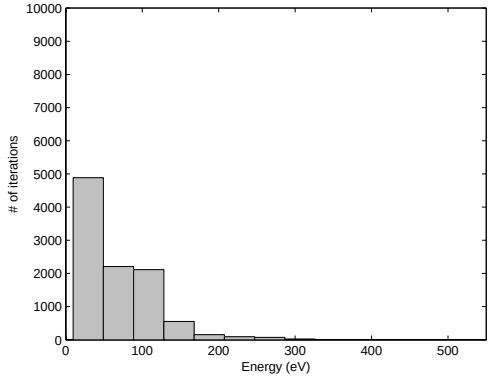

(e) Panel 32.

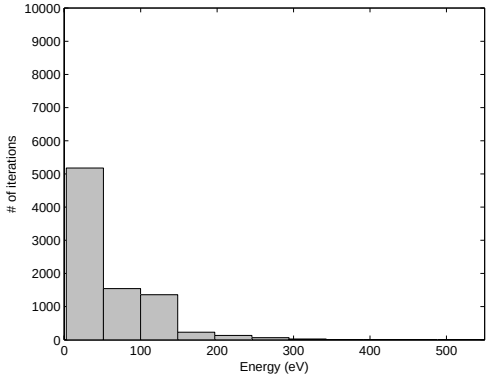

(f) Panel 35.

Figure 5-49: BHT-200: Panel energy distributions for 0-100 hours.

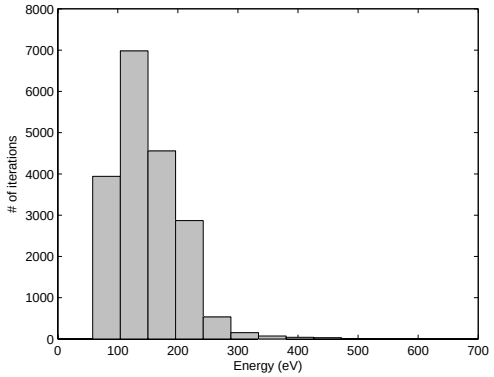

(a) 0-100 hours.

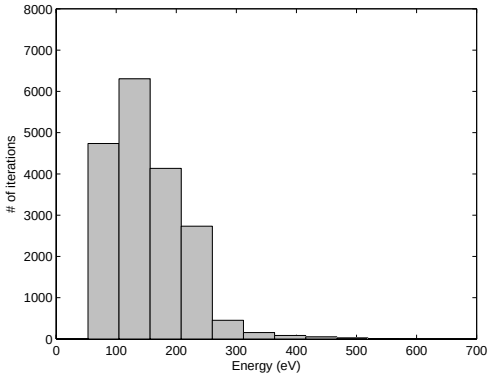

(b) 300-400 hours.

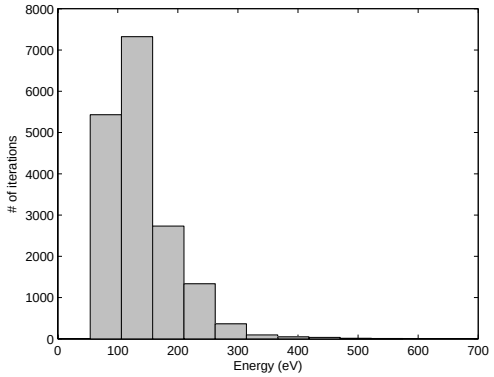

(c) 600-700 hours.

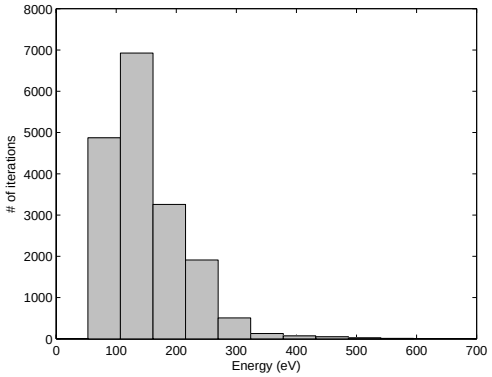

(d) 900-925 hours.

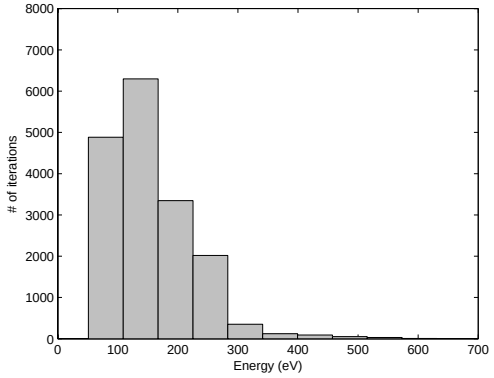

(e) 1110-1170 hours.

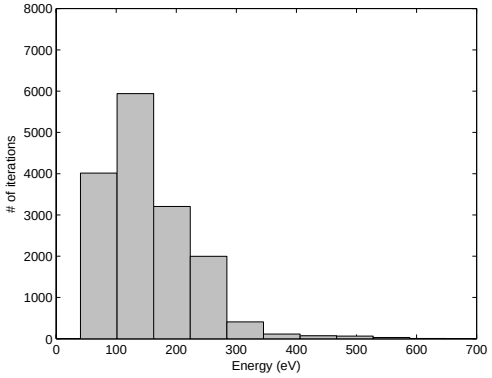

(f) 1270-1330 hours.

Figure 5-50: BHT-200: Energy distributions for Panel 26.

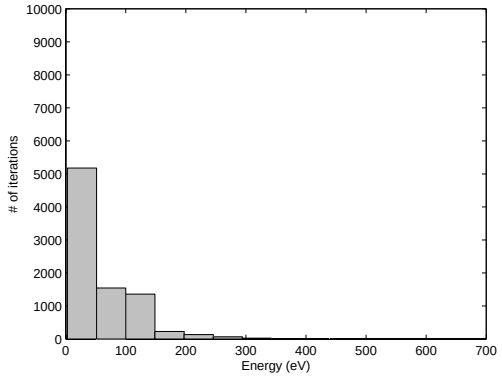

(a) 0-100 hours.

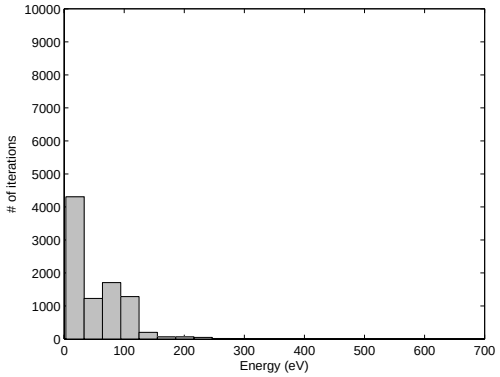

(b) 300-400 hours.

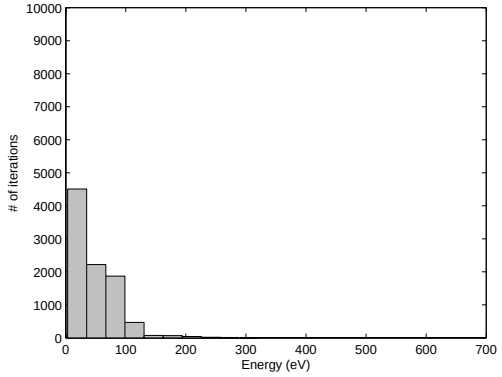

(c) 600-700 hours.

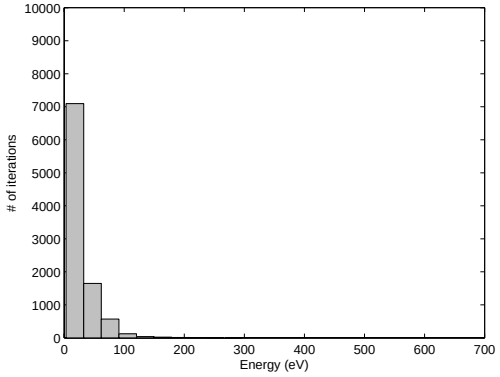

(d) 900-925 hours.

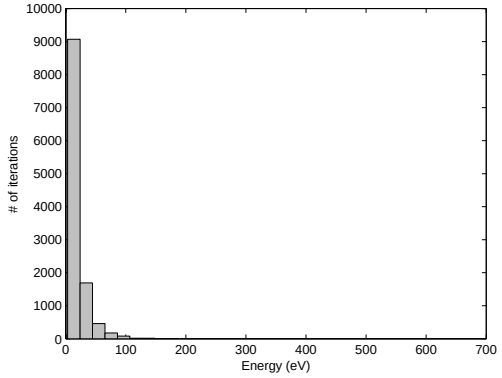

(e) 1110-1170 hours.

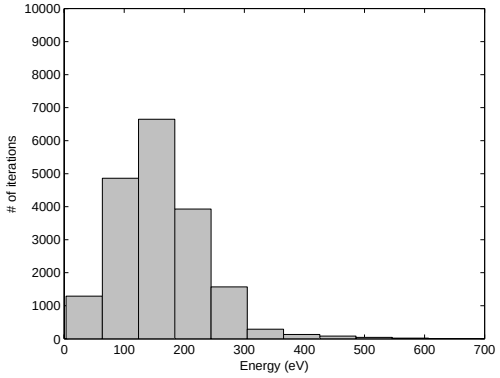

(f) 1270-1330 hours.

Figure 5-51: BHT-200: Energy distributions for Panel 35.

Chapter 6

BHT-600 results

Modeling of the erosion of the BHT-600 is the subject of this chapter. As with the 200W, a summary of the thruster specifications and its simulation inputs will be given, followed by a description of the tuning process to match experimental erosion profiles.

6.1 BHT-600

The BHT-600 is another member of the low-power Hall thruster family developed at Busek Co. Inc. Its nominal specifications are summarized in Table 6.1 and it is pictured in Figure 6-1. Being larger in size, the BHT-600 forgoes a nose cone in favor of the more traditional exit ring configuration. Wall erosion profiles taken during life testing at Edwards Air Force Base are available for tuning of the code. Experimental profiles are from 80, 225, 368, 494, 665 and 932 hours of thruster operation.

Table 6.1: BHT-600 nominal specifications [39].

Discharge input power	600 W
Discharge voltage	300 V
Discharge current	2.05 A
Propellant mass flowrate	2.6 mg/s
Thrust	39.1 mN
Specific Impulse	1530 s
Propulsive efficiency	49.0%

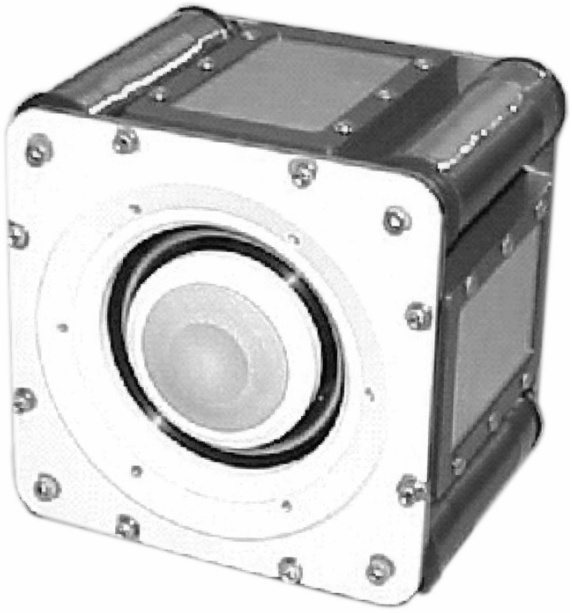

Figure 6-1: BHT-600 thruster [39].

6.2 Simulation procedure

In this section, the baseline setup for modeling of the BHT-600 is outlined as well as the process taken to step the simulated thruster through its virtual life test.

6.2.1 Baseline mesh

The 63×27 computational mesh is based on the thruster geometry depicted in Figure 6-2. Both the inner and outer exit rings are made of HBC grade BN, the same ceramic used for the BHT-200 nose cone. The BHT-600 thruster used for the life test arrived at Edwards having already been operated for 80 hours. During this initial period, a variety of operating conditions were used as well as the cathode being moved further from the discharge chamber. All these changes undoubtedly have an effect on the erosion. Accordingly, the baseline mesh is generated instead from the 80 hour erosion profile since the thruster operating parameters were kept constant from this point on in the life test. Figure 6-3 shows the already-rounded exit rings of the new initial condition.

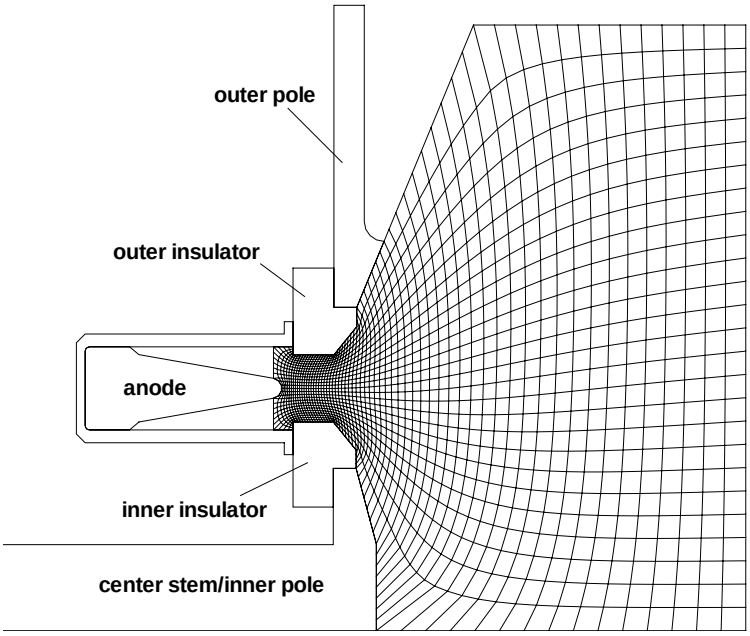

Figure 6-2: BHT-600 geometry.

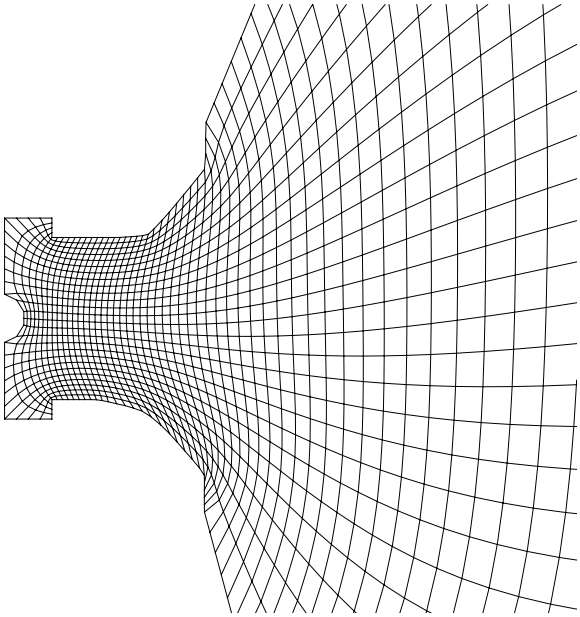

Figure 6-3: BHT-600: Detail of initial mesh after 80 hours of operation.

6.2.2 Baseline magnetic field

The magnetic field extracted from the thruster's Maxwell project is pictured in Figure 6-4 and the corresponding magnetic streamline mesh in Figure 6-5.

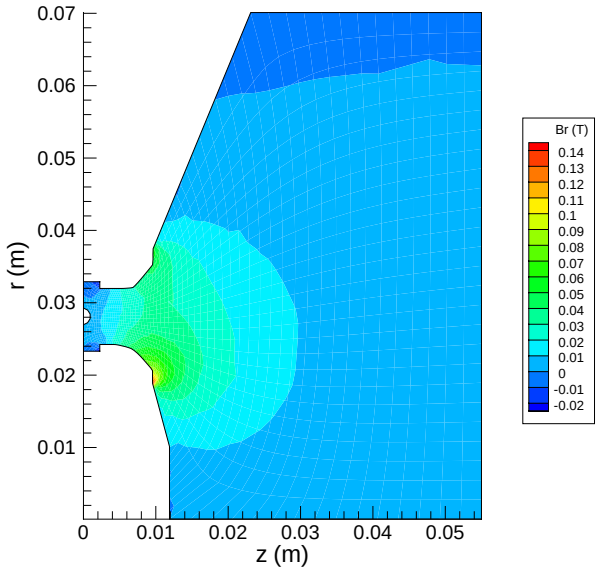

Figure 6-4: BHT-600: Initial magnetic field.

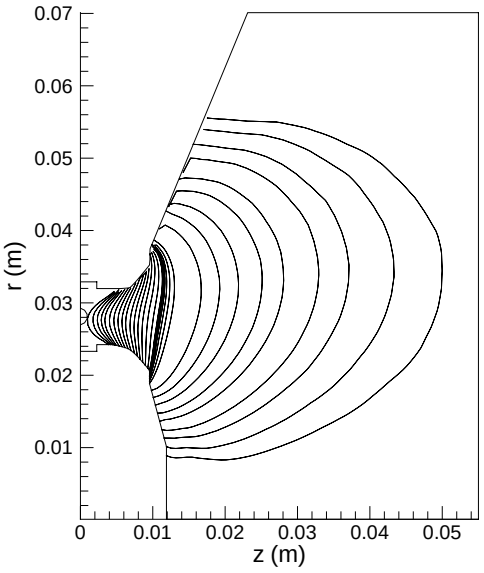

Figure 6-5: BHT-600: Initial magnetic mesh.

Table 6.2: BHT-600 simulation parameters.

M_DOT	2.5×10^{-6} kg/s
V_DISCHARGE	300 V
P_CHAMBER	$5.25e\times10^{-6}$ Torr
T_CHAMBER	300 K
T_WALL	700 K
BOHM_K	0.20
(Z_ANODE, R_ANODE)	(0.000924712, 0.0281865)
(Z_CATHODE, R_CATHODE)	(0.024602802, 0.062215909)

6.2.3 Input parameters

Table 6.2 lists the key *HPHall* inputs that specify the simulated thruster operation. Mass flow rate, discharge voltage and chamber conditions are those used during the long life test and wall temperature is again set at ∼400°C. The anode location is selected to lie on the magnetic line that first intersects a metal component as one moves upstream. For the baseline configuration, this streamline is the leftmost full magnetic line that just brushes the anode tip. The cathode position corresponds to its physical location.

6.2.4 Execution sequence

As before, each simulated lifetime increment requires three *HPHall* runs. The initial sequence is identical to that of the BHT-200 – 20,000 iterations of NEUTRALS_ONLY mode are followed by 1,400 iterations in NORMAL mode. The long NORMAL mode runs to establish wall erosion rates are performed for 10,000 iterations. Figures 6-7 and 6-6 show the calculated erosion rates as a function of run iteration for both an upstream and downstream location on the outer and inner walls. The dashed line denotes the 10,000 iteration mark and shows that its choice is a good compromise between reaching the steady-state erosion rate and having reasonable run times. Less iterations are required for the BHT-600 geometry since it is less complex than that of the BHT-200 and reaches its final state sooner. All runs use an iteration time step of 5×10^{-8} s.

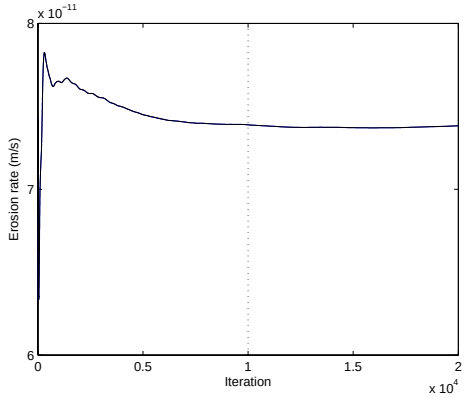

(a) Upstream location.

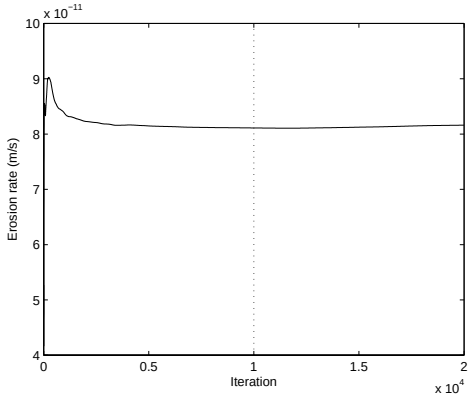

(b) Downstream location.

Figure 6-6: BHT-600: Outer wall erosion rate as function of run iteration.

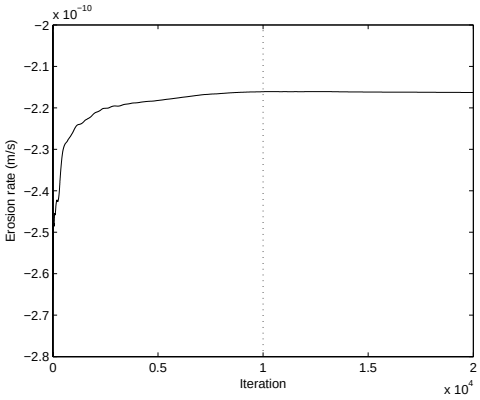

(a) Upstream location.

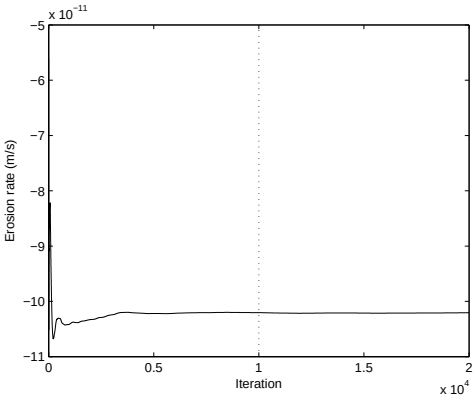

(b) Downstream location.

Figure 6-7: BHT-600: Inner wall erosion rate as function of run iteration.

Table 6.3: BHT-600 erosion time steps.

Case	Erosion Δt (h)	Cumulative Time (h)	Notes
0	–	80	Initial profile
1	73	153	
2	72	225	Experimental profile
3	72	297	
4	71	368	Experimental profile
5	63	431	
6	63	494	Experimental profile
7	86	580	
8	85	665	Experimental profile
9	89	754	
10	89	843	
11	89	932	Experimental profile

The erosion time steps taken to advance the wall profile are summarized in Table 6.3. As with the BHT-200, steps less than 100 hours are used.

6.3 Erosion profile results

Drawing from experience with the BHT-200, a similar tuning process is followed for the BHT-600. Because the exit rings of the 600W and the nose cone of the 200W are both made of HBC grade BN, the sputter model implemented for the smaller thruster is applicable for the larger one and the sputter threshold is set at E_{th}=30 eV. Double ions are also included in all simulation cases. Following the strategy used with the BHT-200, matching of wall profiles from the first several hundred hours of thruster operation is used to choose cases to run for the full simulated life test.

Figure 6-8 shows the experimentally measured erosion profiles. These measurements were taken at Edwards Air Force Base using an optical profilometry system and represent the exit rings along a radial line 90° clockwise from the cathode. Data were also taken at seven other locations evenly spaced about the acceleration channel. As the thruster lifetime progresses, azimuthal asymmetry in the wear pattern is observed as both annular and radial ridges form. At 932 hours of operation, the difference between the least and most eroded profiles is ∼0.5 mm. In general, more

erosion is seen at locations nearer to the cathode. The 90° data are used for comparison since they are indicative of normal erosion, meaning they are representative of an azimuthally-averaged profile. Erosion of the inner insulator is approximately double of that seen on the outer insulator. Unlike the BHT-200, the majority of the erosion appears on the chamfer, where the geometry has bent away from the channel's centerline axis.

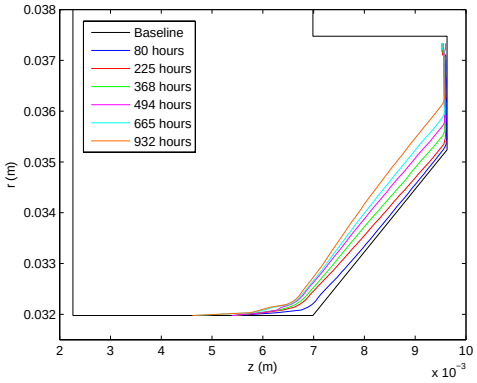

(a) Experimental profiles, outer insulator.

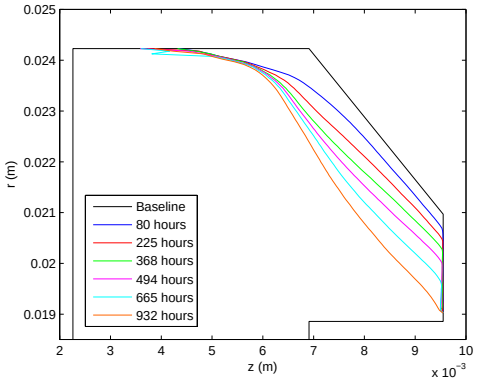

(b) Experimental profiles, inner insulator.

Figure 6-8: BHT-600: Experimental erosion profiles.

6.3.1 Effect of cathode lambda line position

The first parameter to be selected is the cathode lambda line. Figure 6-9 shows the physical cathode location as well as lambda lines for the anode and possible cathode line positions. Unlike in the 200W thruster mesh, the rightmost cathode line, C1,

comes quite close to the actual cathode location. The remaining lines, C2 and C3, lie nearer to the acceleration channel.

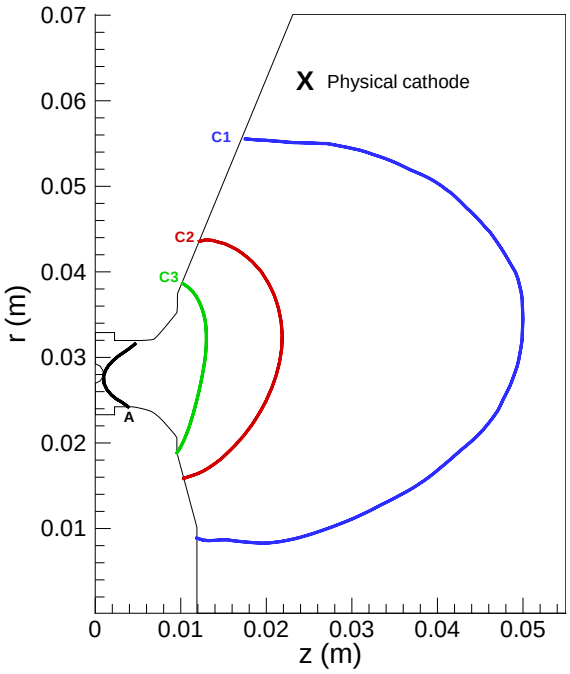

Figure 6-9: BHT-600 lambda lines.

Figure 6-10 plots the simulated erosion profiles for both outer and inner insulators at 225 and 368 hours of operation. As seen in Figure 6-10(c), after 225 hours, the leftmost cathode line position, C3, has already caused significant erosion of the inner insulator's front face which is not observed in the experimental data. Thus, this candidate is eliminated and not tested further. At 368 hours, little difference between the two cathode lines is seen, though C2 captures the erosion at the inner insulator corner marginally better.

Figure 6-11 shows the erosion rates of the outer and inner walls during the run representing 153-225 hours of operation. Note that in this and future plots, due to the exit ring shape, the distribution is plotted as a function of nodal position along the wall. For ease of comparison to the wall profiles, reference nodes on the insulator plots are labeled. In general, the inner exit ring exhibits greater erosion than the outer one. In addition, as already witnessed in the erosion profiles, moving the cathode line closer to the discharge increases the erosion. Figures 6-12 and 6-13

give the averaged outer and inner wall distributions from the same run. Evidence for the greater erosion of the inner insulator is seen in the overall higher levels of flux and energy impinging this wall. As in the BHT-200, erosion rates are tracked well by the energy distributions. While peak flux and energy remain in the same location for lambda lines C2 and C3, proof of the plasma being pushed further back into the discharge chamber is seen with C1 as the maxima occur earlier.

Tables 6.4 and 6.5 summarize the performance parameters. Bringing the cathode line closer to the acceleration channel increases the discharge current while its effect on thrust is less clear. Discharge current is predicted accurately by C2 while thrust is underpredicted by all cases. Because of its good agreement with the nominal discharge current, C2 is selected to continue in the simulation tuning.

Table 6.4: BHT-600: Simulated discharge current [A] – effect of cathode line position. Nominal=2.0.

Run (hours)	C1	C2	C3
80-153	1.768384	1.925162	2.788134
153-225	1.752214	1.969709	2.831261
225-297	1.756765	1.956047	–
297-368	1.794367	2.002540	–
Average	1.767933	1.963365	2.809698

Table 6.5: BHT-600: Simulated thrust [mN] – effect of cathode line position. Nominal=39.1.

Run (hours)	C1	C2	C3
80-153	29.106	28.341	33.769
153-225	28.858	29.014	30.179
225-297	28.933	28.796	–
297-368	29.550	29.744	–
Average	29.112	28.974	31.974

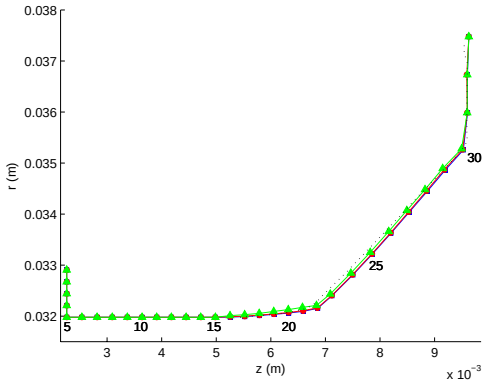

(a) Outer insulator, 225 hours.

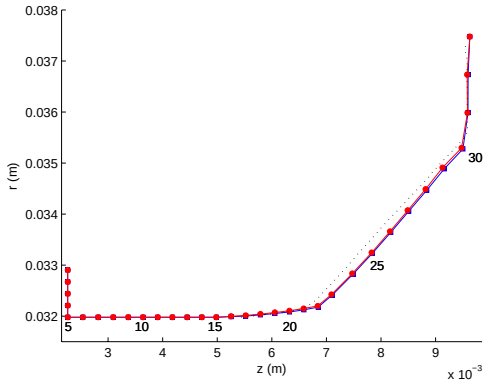

(b) Outer insulator, 368 hours.

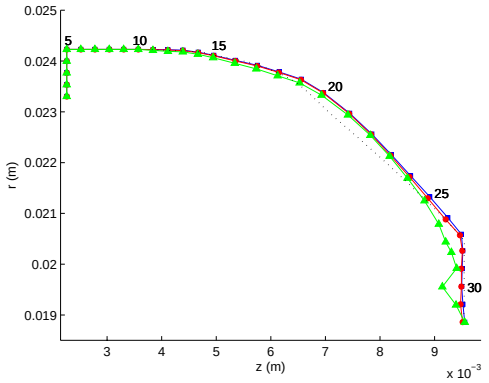

(c) Inner insulator, 225 hours.

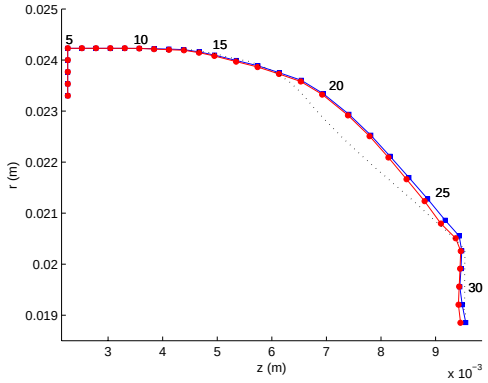

(d) Inner insulator, 368 hours.

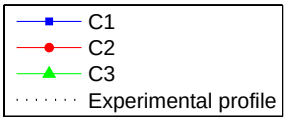

Figure 6-10: BHT-600: Erosion profile evolution – effect of cathode line position.

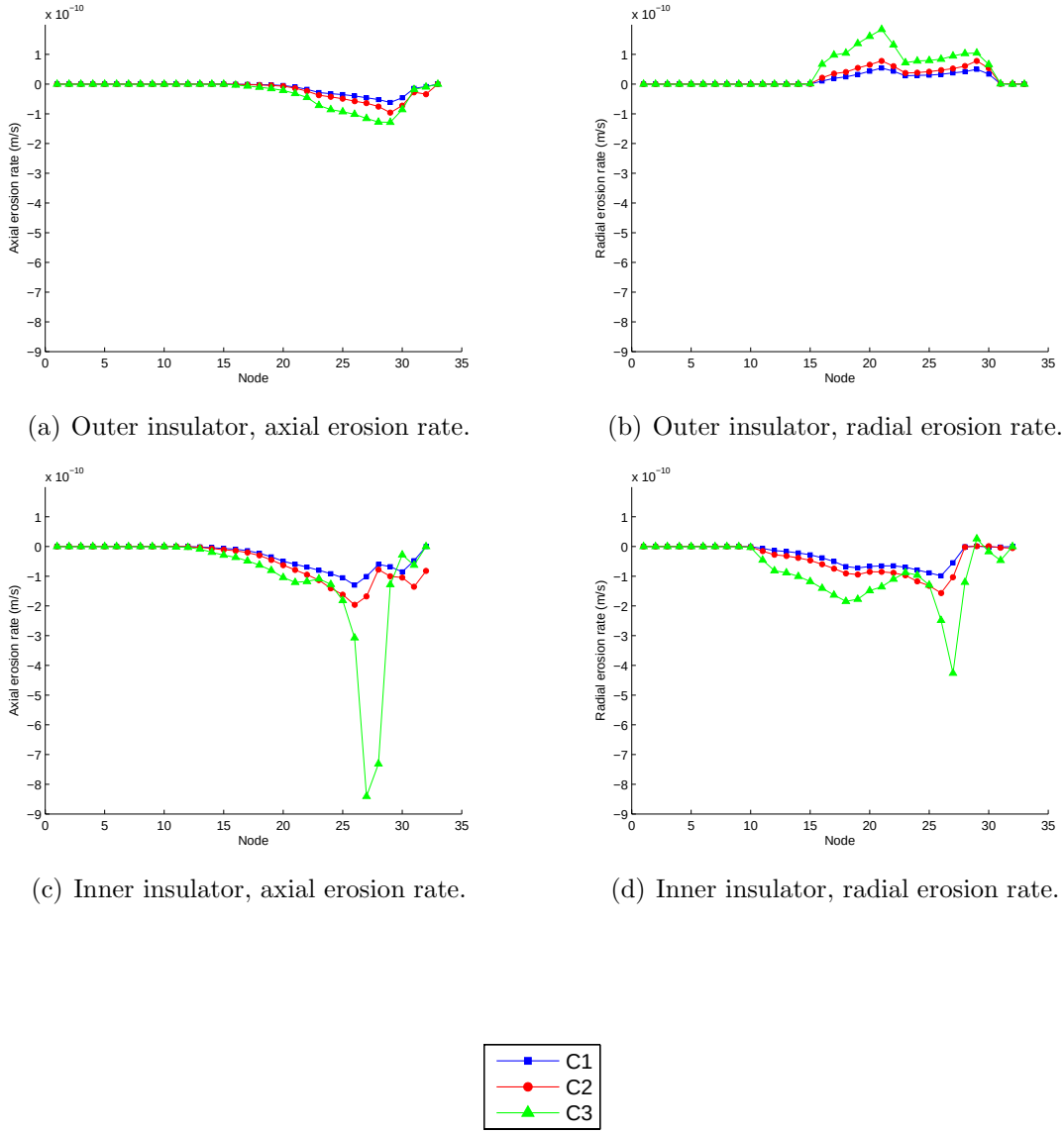

(a) Outer insulator, axial erosion rate.

(b) Outer insulator, radial erosion rate.

(c) Inner insulator, axial erosion rate.

(d) Inner insulator, radial erosion rate.

Figure 6-11: BHT-600: Wall erosion rates during 153-225 hour run – effect of cathode line position.

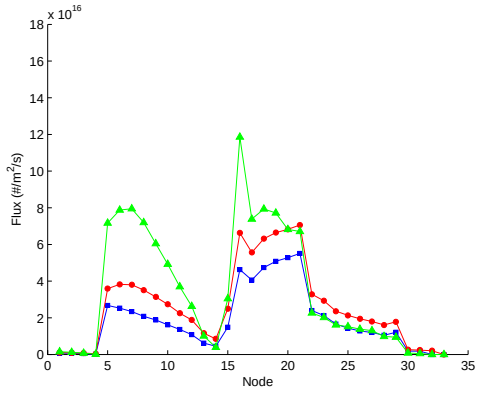

(a) Flux.

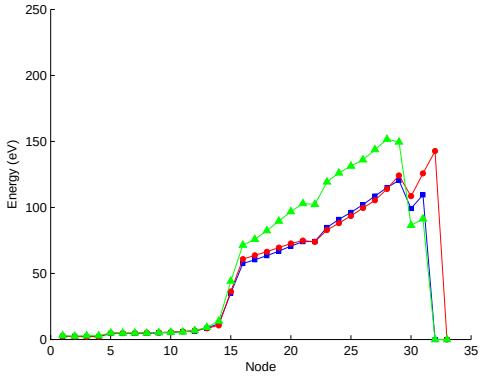

(b) Energy.

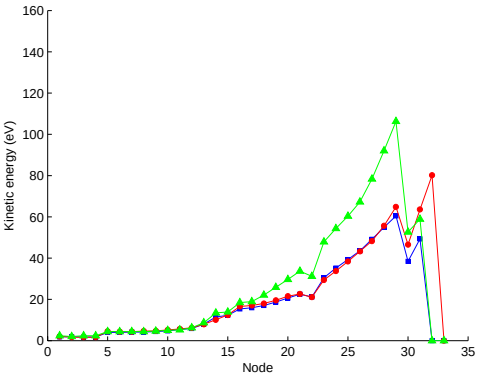

(c) Kinetic energy.

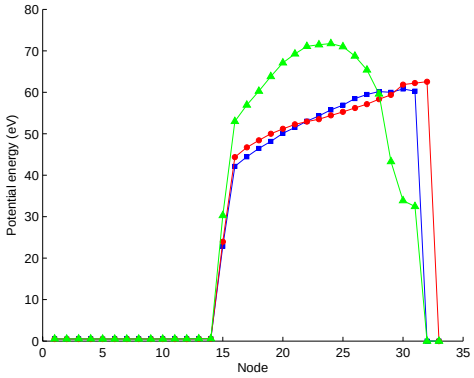

(d) Potential energy.

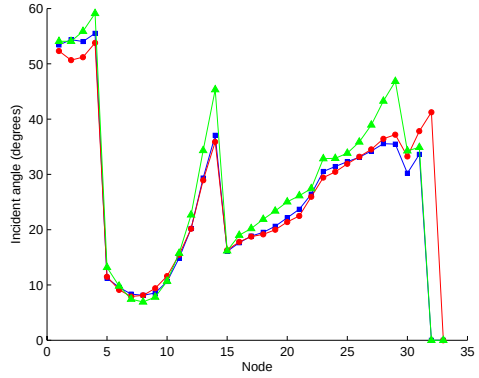

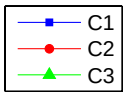

(e) Incident angle.

Figure 6-12: BHT-600: Averaged outer wall distributions during 153-225 hour run – effect of cathode line position.

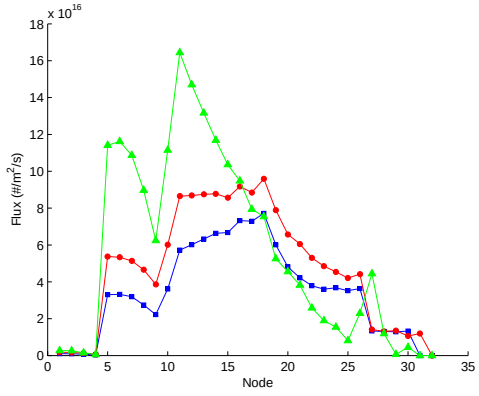

(a) Flux.

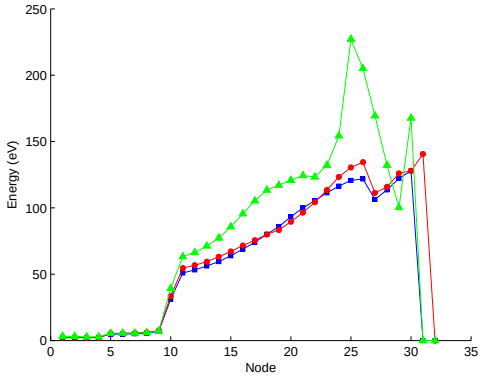

(b) Energy.

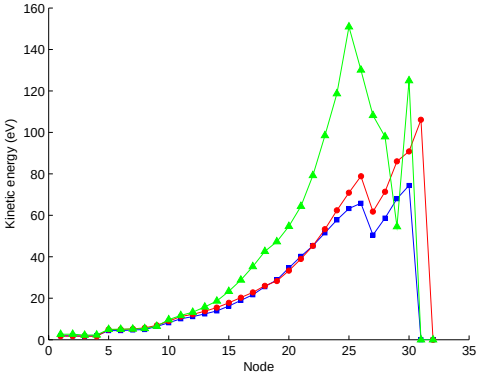

(c) Kinetic energy.

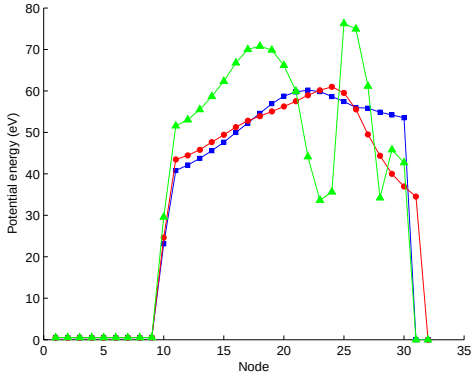

(d) Potential energy.

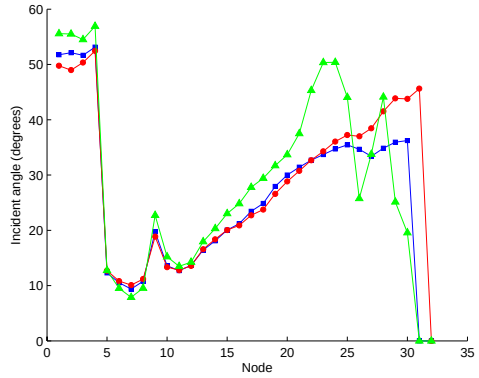

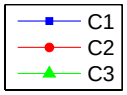

(e) Incident angle.

Figure 6-13: BHT-600: Averaged inner wall distributions during 153-225 hour run – effect of cathode line position.

6.3.2 Effect of anomalous transport model

In the case of the BHT-200, the anomalous transport model is needed to position the plasma such that the erosion is predicted correctly. This section outlines the process followed in tuning the barrier parameters for the 600W thruster.

Imposed transport barrier

Transport barriers of various widths and positions are tried with the BHT-600 geometry. Figure 6-14 shows the locations of the most successful of these cases.

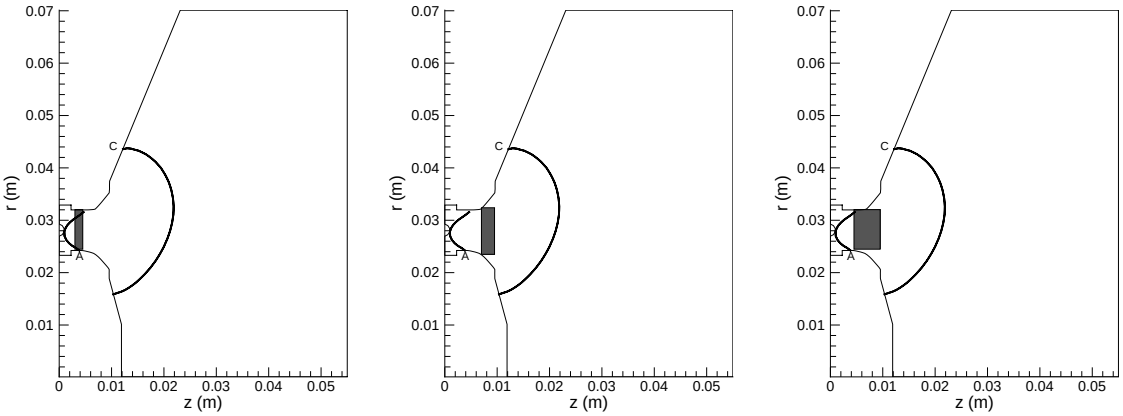

(a) Left, z=0.003-0.0045 m. (b) Right, z=0.007-0.0095 m. (c) Wide, z=0.0045-0.0095 m.

Figure 6-14: BHT-600: Imposed transport barrier locations.

Figures 6-15 and 6-16 show the erosion profiles and rates for the different transport barriers. Again, more erosion of the inner insulator is observed. At 225 hours, all cases do well in the upstream region of both insulators, but begin to diverge from the experimental profiles in the mid-region along the exit ring chamfer. The wide transport barrier does marginally better in the middle of the chamfer. At 368 hours, the right, wide and no barrier cases exhibit the same trends and underpredict the erosion. The left barrier case, on the other hand, behaves differently. Although it overpredicts erosion in the upstream region, the left barrier shows better agreement along the chamfer and with the net erosion. Averaged wall distributions are given in Figures 6-17 and 6-18. In these cases, the correlation between the energy and erosion rate distributions is less apparent. Because the majority of erosion is occuring on the

chamfer, the flux distribution to this hard-to-reach area is now of importance also.

Tables 6.6 and 6.7 compare the performance parameters between cases. The right and wide barriers lead to reduced discharge currents and thrusts while the left barrier maintains current and improves thrust.

Table 6.6: BHT-600: Simulated discharge current [A] – effect of imposed transport barrier. Nominal=2.0.

Run (hours)	none	left	right	wide
80-153	1.925162	1.975790	1.101357	1.127590
153-225	1.969709	1.972013	1.090079	1.126179
225-297	1.956047	1.970575	1.069803	1.135166
297-368	2.002540	1.979899	1.193645	1.115174
Average	1.963365	1.974569	1.113721	1.126027

Table 6.7: BHT-600: Simulated thrust [mN] – effect of imposed transport barrier. Nominal=39.1.

Run (hours)	none	left	right	wide
80-153	28.341	29.782	22.898	24.553
153-225	29.014	30.797	22.875	24.538
225-297	28.796	30.727	22.416	24.708
297-368	29.744	30.810	24.007	24.477
Average	28.974	30.529	23.049	24.569

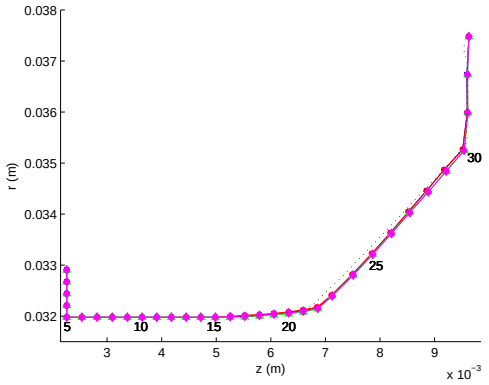

(a) Outer insulator, 225 hours.

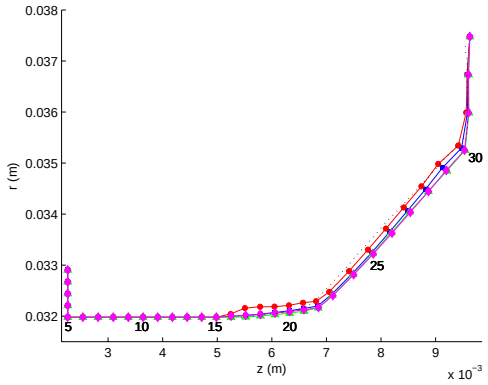

(b) Outer insulator, 225 hours.

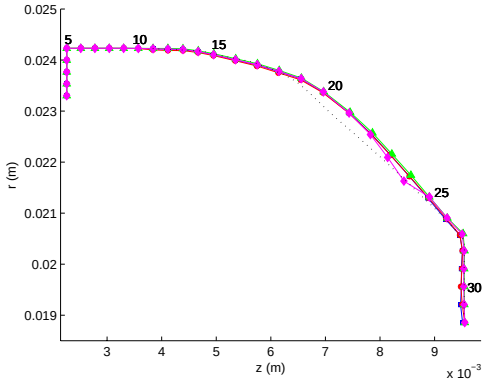

(c) Inner insulator, 225 hours.

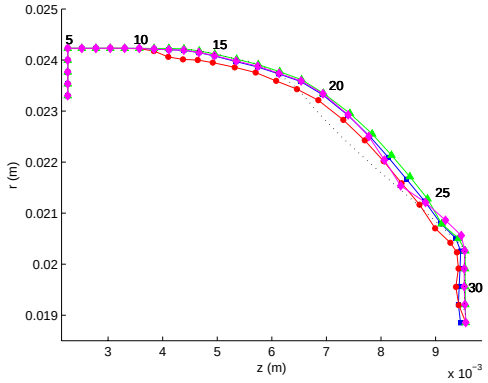

(d) Inner insulator, 368 hours.

Figure 6-15: BHT-600: Erosion profile evolution – effect of imposed transport barrier.

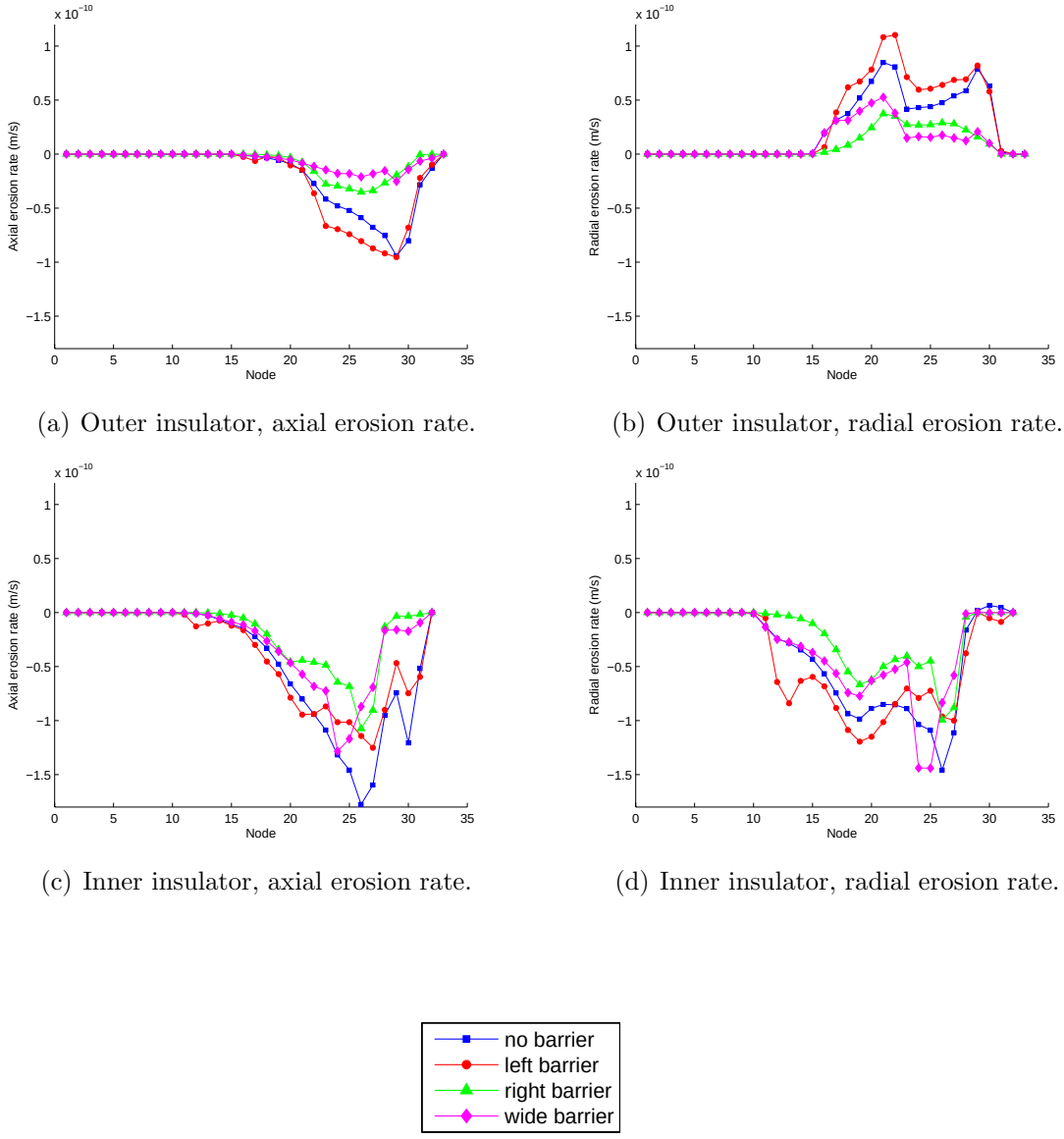

(a) Outer insulator, axial erosion rate.

(b) Outer insulator, radial erosion rate.

(c) Inner insulator, axial erosion rate.

(d) Inner insulator, radial erosion rate.

Figure 6-16: BHT-600: Wall erosion rates during 297-368 hour run – effect of imposed transport barrier.

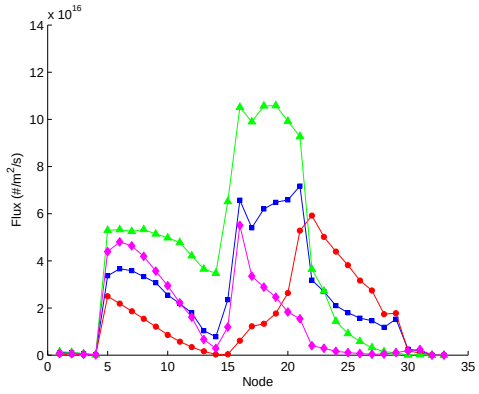

(a) Flux.

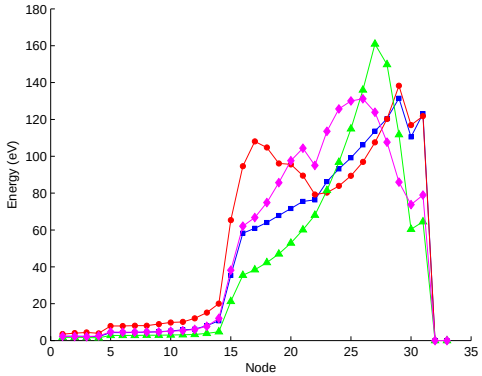

(b) Energy.

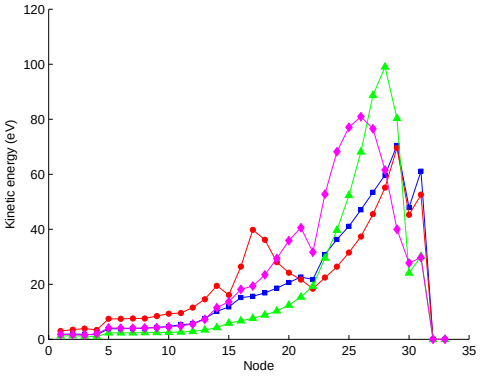

(c) Kinetic energy.

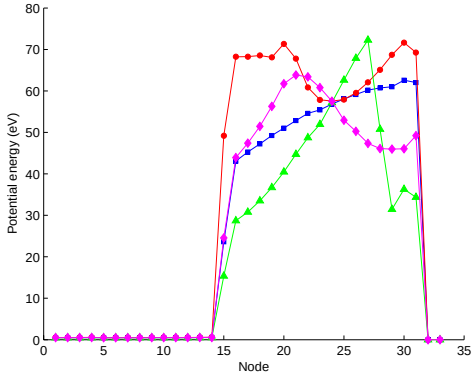

(d) Potential energy.

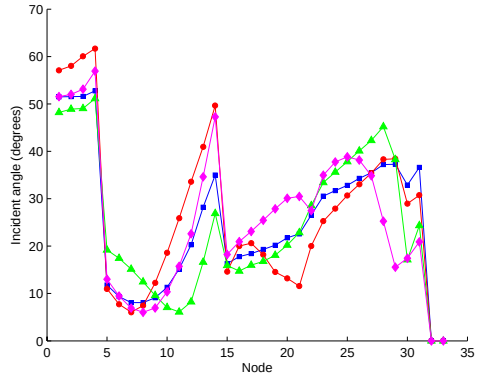

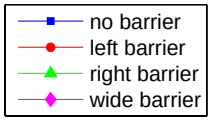

(e) Incident angle.

Figure 6-17: BHT-600: Averaged outer wall distributions during 297-368 hour run – effect of imposed transport barrier.

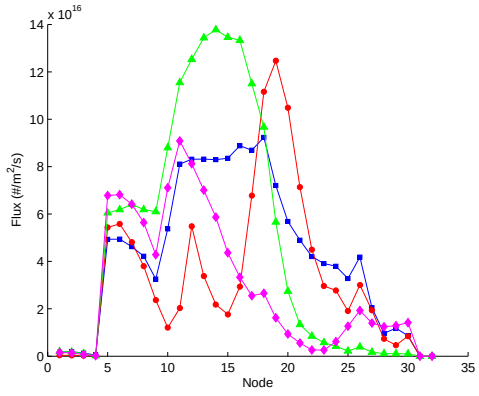

(a) Flux.

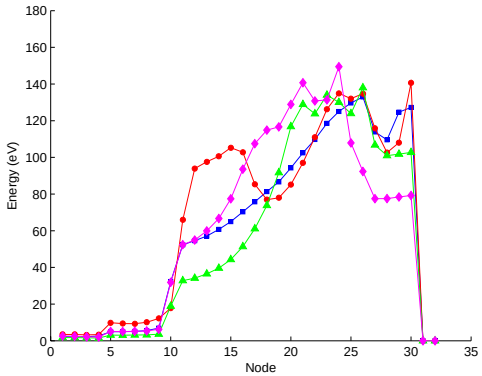

(b) Energy.

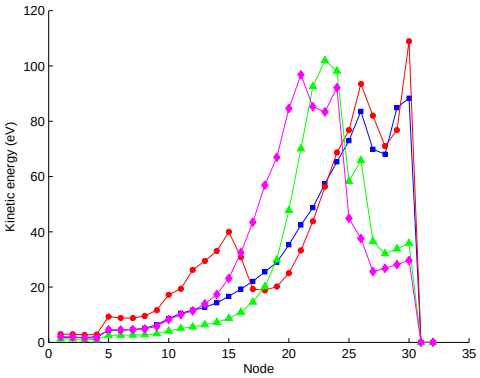

(c) Kinetic energy.

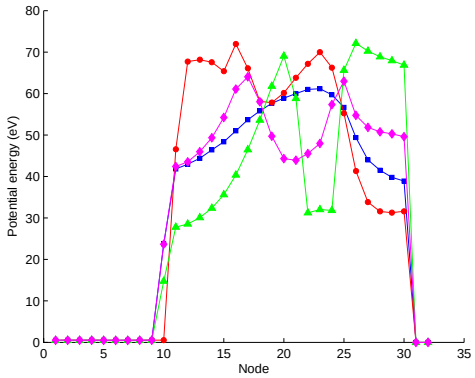

(d) Potential energy.

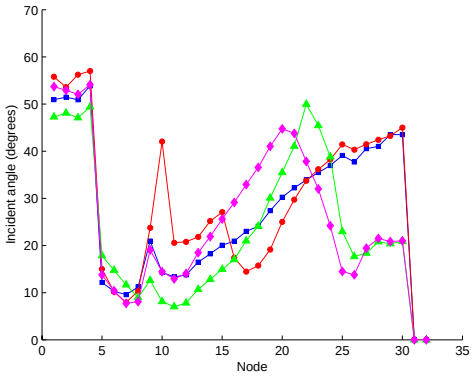

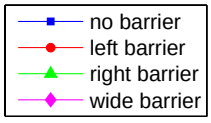

(e) Incident angle.

Figure 6-18: BHT-600: Averaged inner wall distributions during 297-368 hour run – effect of imposed transport barrier.

Understanding transport barriers

To better understand how the transport barrier affects the discharge plasma, Figure 6-19 compares the plasma density contour maps for each case. The left barrier has the least effect while the right barrier pushes the density further into the channel and the wide barrier spreads the plasma out. Figure 6-20 shows the electron temperature maps for each barrier. Again, the left barrier has little influence while the right and wide barriers cause the band of high electron temperature to collapse to a narrow region centered approximately in the middle of the imposed barrier. It is conjectured that the sharp boundaries of the imposed barrier lead to the abrupt edges of this area of high electron temperature. A Gaussian barrier is implemented where the mean of the distribution is centered at the midpoint of the barrier and the standard deviation is its half-width. Figure 6-21 illustrates the barrier weightings for the right and right Gaussian barriers. Figure 6-22 shows electron temperature maps for the right and wide cases where a Gaussian barrier is used. Comparing the contour plots, it is observed that the Gaussian barriers tend to slightly reduce the peak electron temperature and spread the band. The effect of these smooth barriers is further demonstrated in Figures 6-23 and 6-24 which compare the wall flux and energy distributions to the inner insulator between the step and Gaussian barriers. The shape of the barrier clearly plays a role in the subsequent wall distributions, especially that of the flux. The detailed effect of the shape is determined by the barrier location. Thus, the shape of the transport barrier is an additional parameter that can be tuned to control the plasma behavior which in turn determines the erosion.

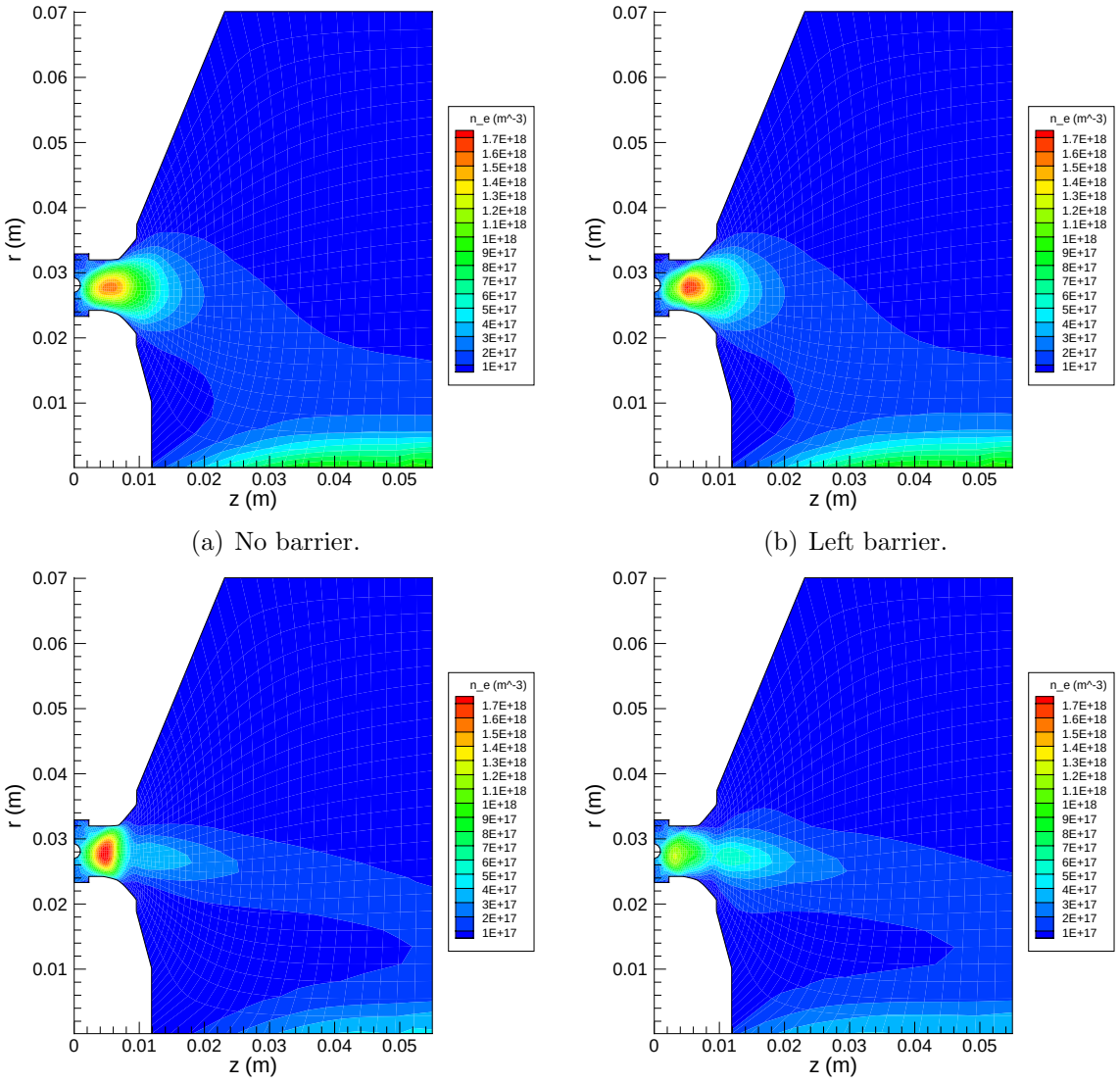

(a) No barrier.

(b) Left barrier.

(c) Right barrier.

(d) Wide barrier.

Figure 6-19: BHT-600: Plasma density – effect of transport barrier.

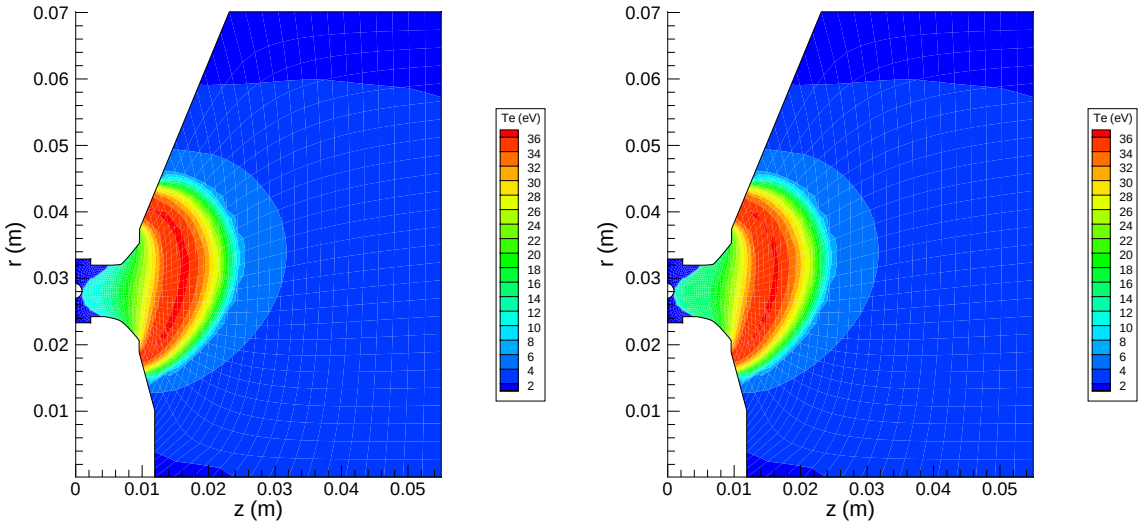

(a) No barrier.

(b) Left barrier.

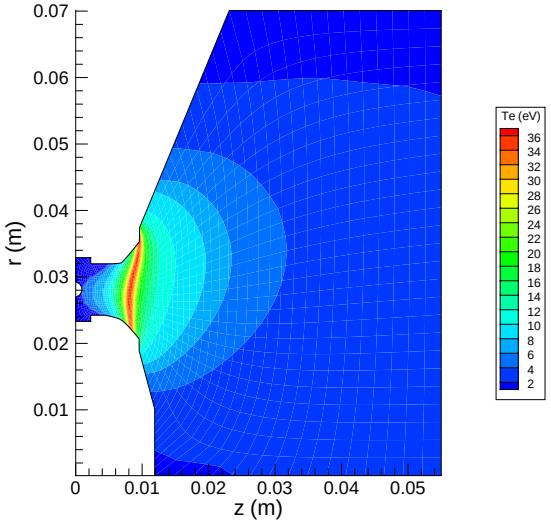

(c) Right barrier.

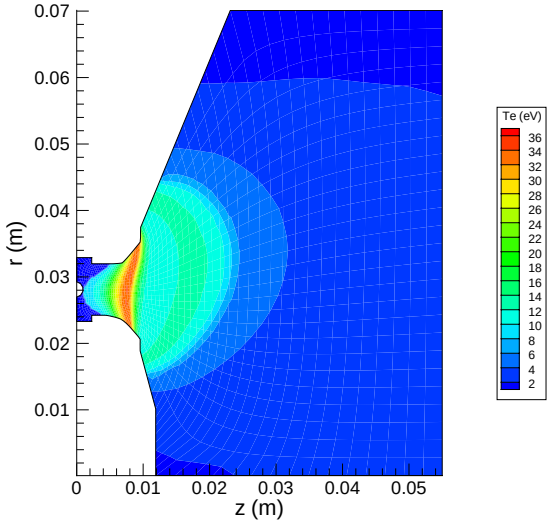

(d) Wide barrier.

Figure 6-20: BHT-600: Electron temperature – effect of transport barrier.

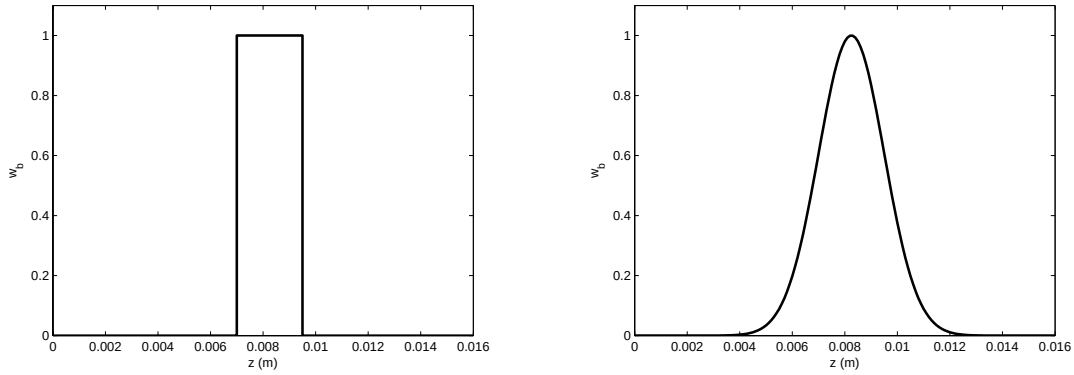

(a) Right barrier weighting.

(b) Right Gaussian barrier weighting.

Figure 6-21: BHT-600: Imposed transport barrier weightings.

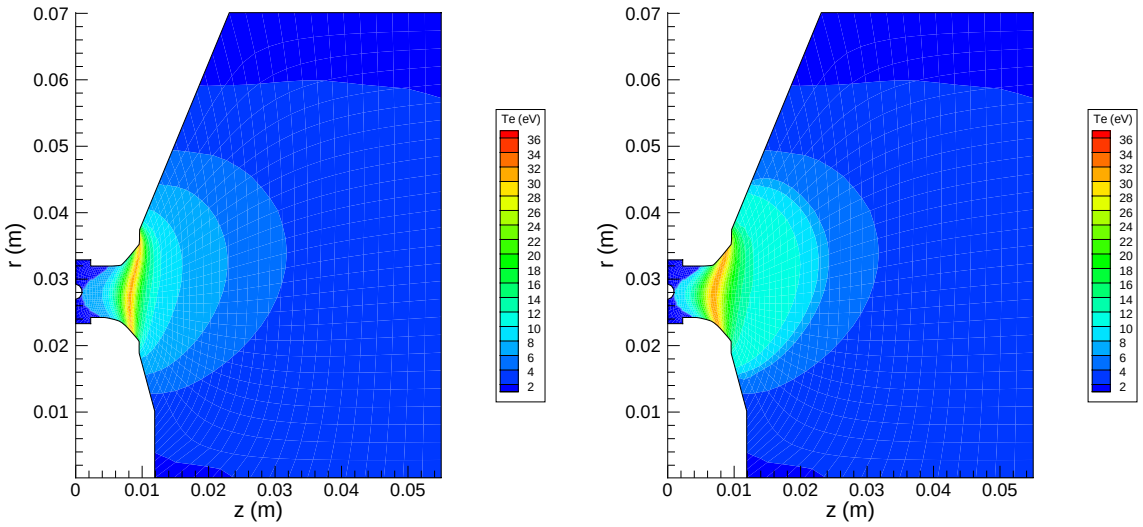

(a) Right Gaussian barrier.

(b) Wide Gaussian barrier.

Figure 6-22: BHT-600: Electron temperature – effect of Gaussian transport barrier.

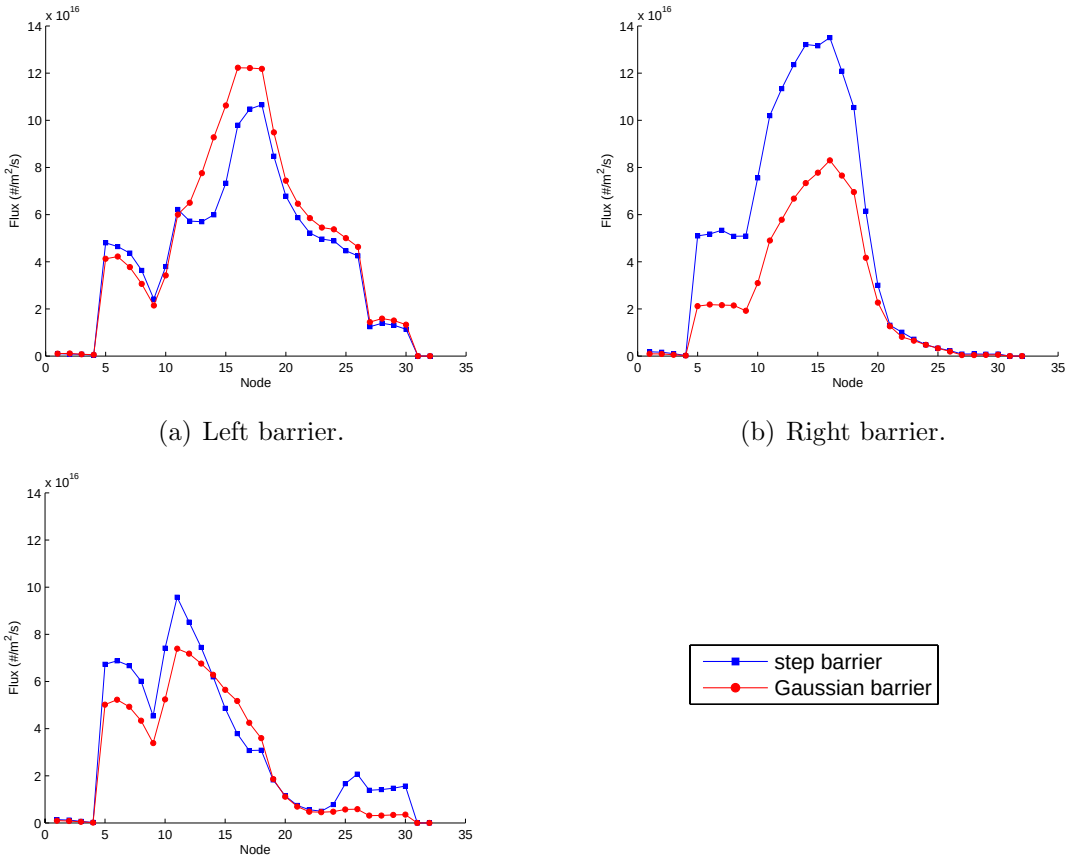

(a) Left barrier.

(b) Right barrier.

(c) Wide barrier.

Figure 6-23: BHT-600: Inner wall flux distributions during 80-153 hour run – effect of transport barrier shape.

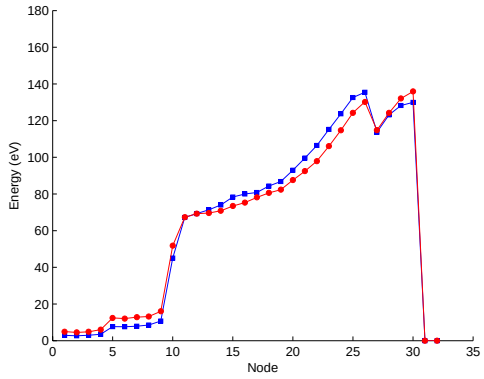

(a) Left barrier.

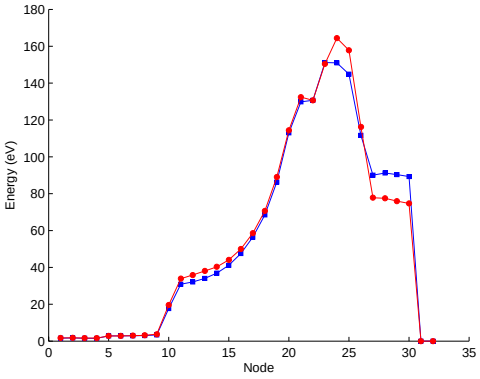

(b) Right barrier.

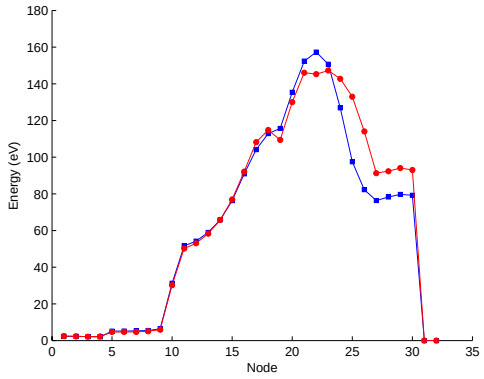

(c) Wide barrier.

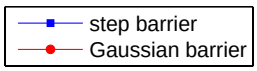

Figure 6-24: BHT-600: Inner wall energy distributions during 80-153 hour run – effect of transport barrier shape.

Since the exact shape of the transport barrier is unknown, further study will be performed with the step barriers. Figure 6-25 plots the wall ion flux distributions separately with a box overlaid to denote each barrier location. Contrary to expectation, the barrier position corresponds to a region of depressed wall flux rather than an increase due to the concentration of electrons. To investigate this behavior further, traces of the centerline plasma properties inside the acceleration channel are taken and shown in Figure 6-26 with corresponding barrier locations. Plasma density has a close resemblance to the flux striking the wall, but again its correlation with the barrier position is unclear. Ionization rate exhibits little difference caused by the barriers. Hence, shifting of the ionization region due to the barrier is eliminated as the possible cause of the decreased wall flux. Potential, on the other hand, is clearly affected by the imposed barriers. Due to its lower conductivity coupled with the requirement of current conservation, the transport barrier region has a higher electric field. This behavior is observed in the potential traces since a steepening of the potential gradient occurs inside the barrier. The role of the potential gradient is to accelerate ions from the site where they are created. As an ion moves from areas of high to low potential, it gains kinetic energy. If an ion lies in a region of steep axial potential gradient, it will gain forward momentum, be less likely to get diverted radially and accelerate out of the thruster channel. Conversely, if an ion lies in a region of flat axial potential gradient, it will be more susceptible to any radial potential gradient and the likelihood of striking the wall is greater. Comparing Figures 6-25 and 6-26(c), a correlation between decreases in wall flux and steep potential gradients is observed. Both of these phenomena lie within the imposed transport barriers. Figure 6-27 illustrates this effect with two representative particle trajectories for the no and right barrier cases. In the no barrier case, the ion is created in a region with enough axial potential gradient to accelerate it out of the thruster, leading to less flux to the channel wall. In the right barrier case, the ion is born in a region of flat axial potential gradient – the radial forces dominate and the particle is diverted into the wall, leading to the observed peak in the flux distribution.

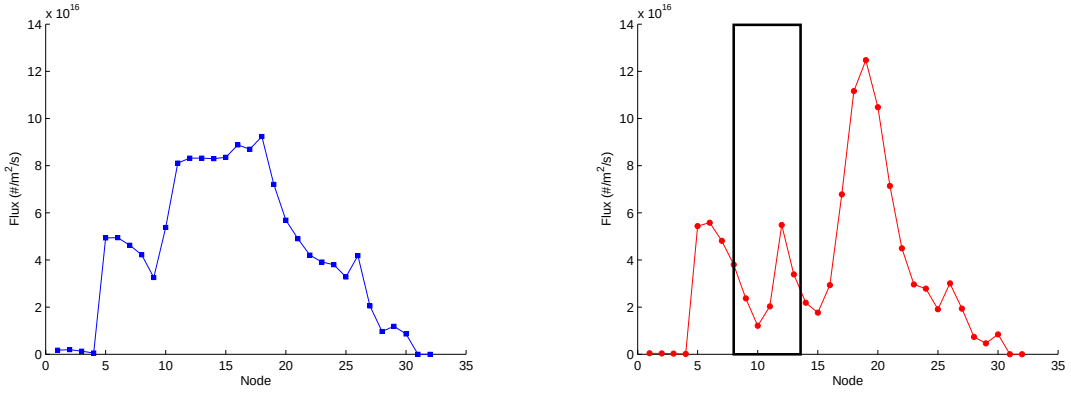

(a) No barrier.

(b) Left barrier.

(c) Right barrier.

(d) Wide barrier.

Figure 6-25: BHT-600: Flux distribution to inner wall during 297-368 hour run.

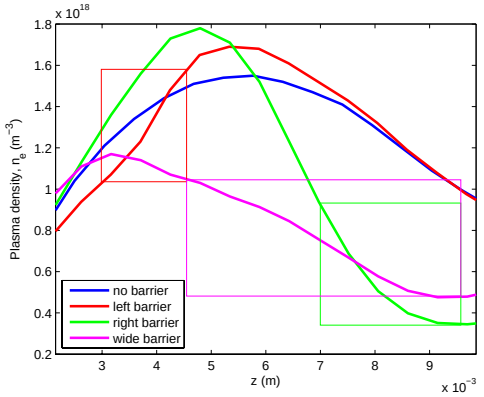

(a) Plasma density.

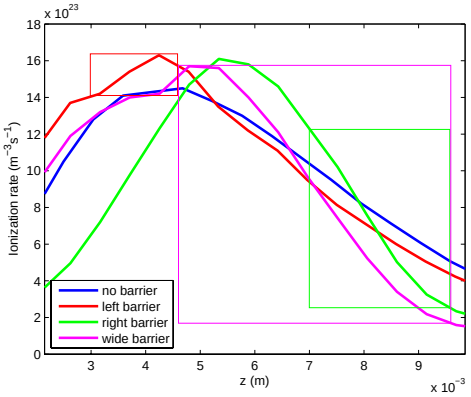

(b) Ionization rate.

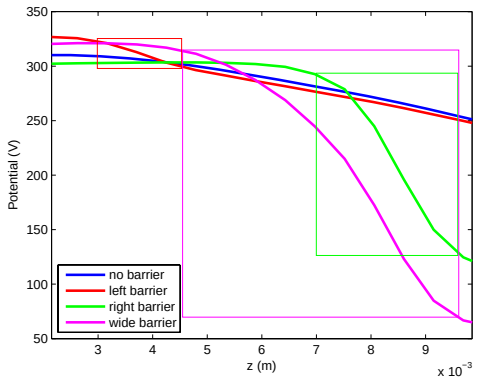

(c) Potential.

Figure 6-26: BHT-600: Centerline plasma properties – effect of transport barrier.

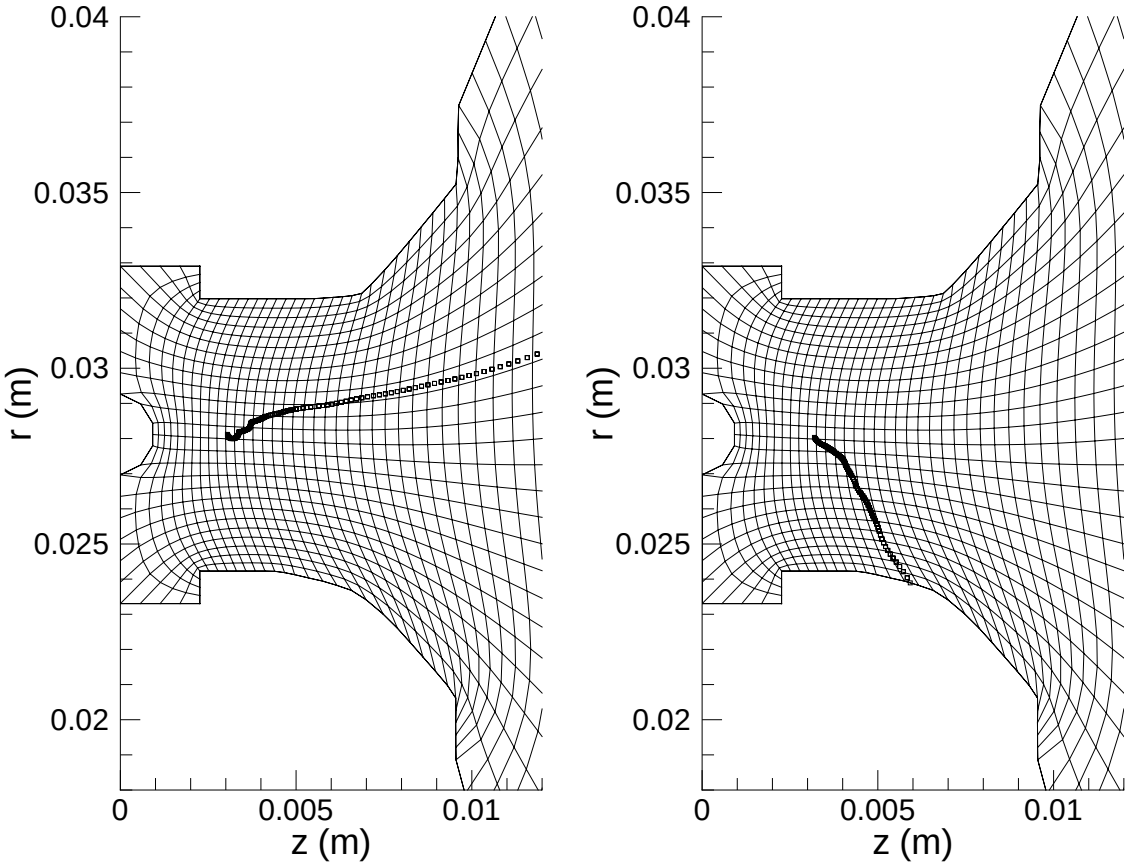

(a) No barrier.

(b) Right barrier.

Figure 6-27: BHT-600: Representative particle trajectory – effect of transport barrier.

6.4 Simulated life test

Because of its better agreement in the chamfer region, net erosion and performance parameters, the left barrier case is chosen to complete the simulated life test up to the full 932 hours of operation. Figure 6-28 compares simulated and experimental profiles at the intermediate times of 494 and 665 hours. Figure 6-29 gives the comparison at the final 932 hour mark. As exhibited throughout the test, erosion is overpredicted upstream and underpredicted in the downstream chamfer region for both inner and outer insulators. Though the exact shape of the wall profiles is not reproduced, the overall erosion is captured well as is the relative amounts of erosion on the inner and outer exit rings.

To improve the predictions, the transport model requires more tuning to better place the plasma. A number of adjustments can be made through the position of the cathode lambda line, the Bohm coefficient and the position and shape of the imposed barrier. This last parameter deserves a closer look as the current method is rather crude and experimental observations have shown that the actual barrier shape is smoother than the one used here. As seen in the previous section, imposing a smooth Gaussian barrier results in a smearing of the electron temperature that could lead to improved transport and subsequently the correct erosion behavior. The present results show promise and indicate that finding the proper barrier could lead to successful prediction of the erosion. Experimental measurements of the barrier in the thrusters of interest would greatly benefit solving of this issue.

Figure 6-30 plots the simulated thruster performance over the 932 hours. No clear trend in either the discharge current or thrust is seen over the course of the thruster's life. The discharge current matches closely with the nominal value of 2.0 A while the thrust is consistently underpredicted.

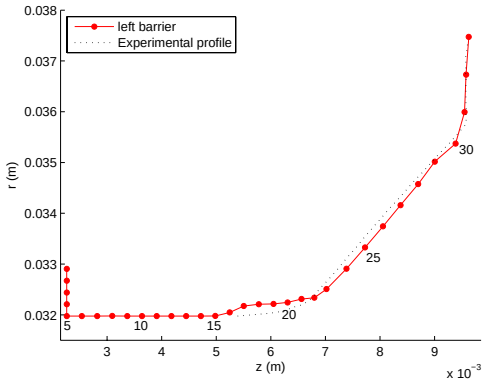

(a) Outer insulator, 494 hours.

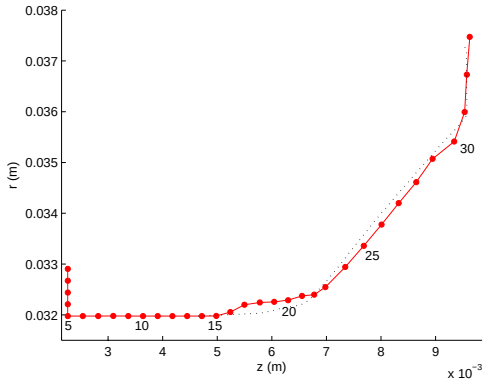

(b) Outer insulator, 665 hours.

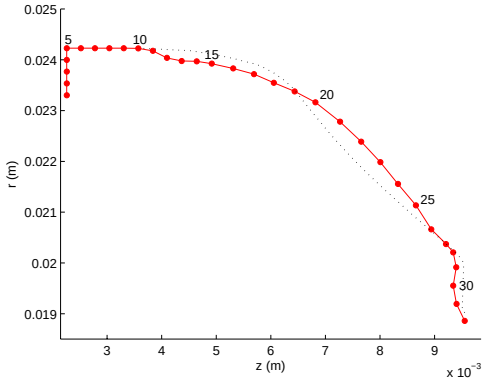

(c) Inner insulator, 494 hours.

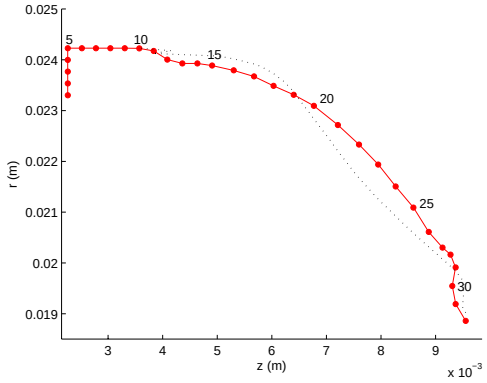

(d) Inner insulator, 665 hours.

Figure 6-28: BHT-600: Erosion profile evolution – intermediate cases of simulated life test.

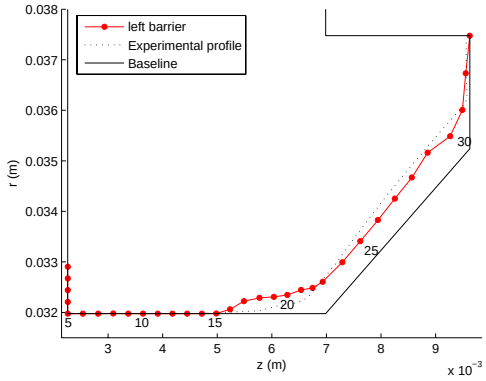

(a) Outer insulator, 932 hours.

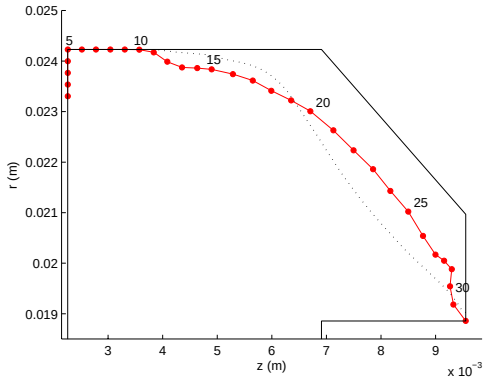

(b) Inner insulator, 932 hours.

Figure 6-29: BHT-600: Erosion profile evolution – end of life of simulated life test.

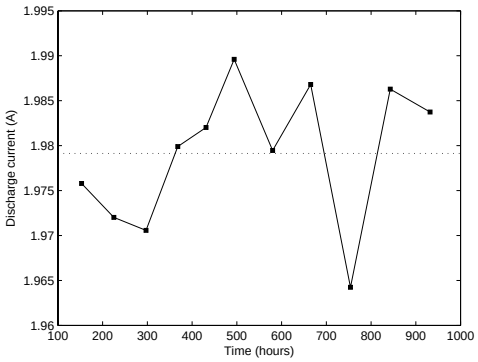

(a) Discharge current, nominal=2.0 A.

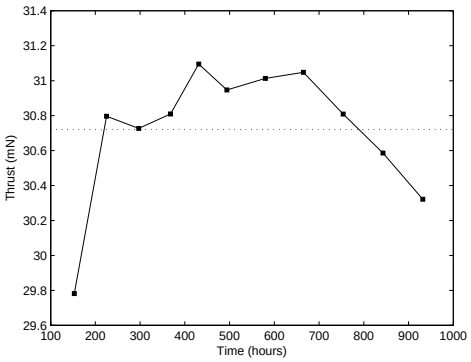

(b) Thrust, nominal=39.1 mN.

Figure 6-30: BHT-600 simulated performance over lifetime. Average marked with dashed line.

6.4.1 Importance of double ions

To check the importance of double ions in this geometry, a case with identical parameters to that used for the simulated life test is run, except double ions are turned off. Figures 6-31 and 6-32 show the inner and outer averaged wall distributions for the cases with and without double ions. The addition of double ions results in slight increases in flux and energy on both exit rings. These increases translate into greater erosion rates as seen in Figure 6-33. Figure 6-34 compares the total ion with solely double ion flux. In the BHT-600, double ions account for less than 5% of the wall particle flux. However, the increase in the erosion rate is as high as a factor of $\sim$2-2.5 due to their addition. Therefore, inclusion of the double ions in the lifetime prediction model is imperative.

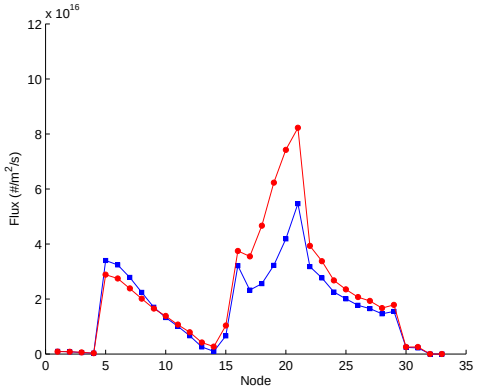

(a) Flux.

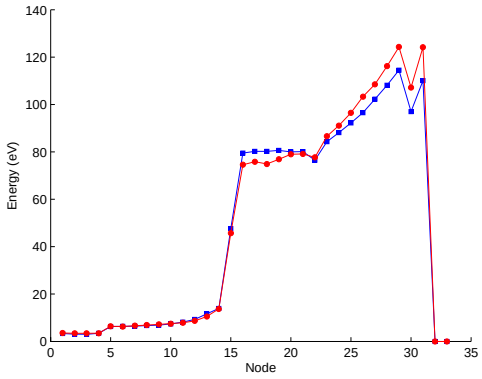

(b) Energy.

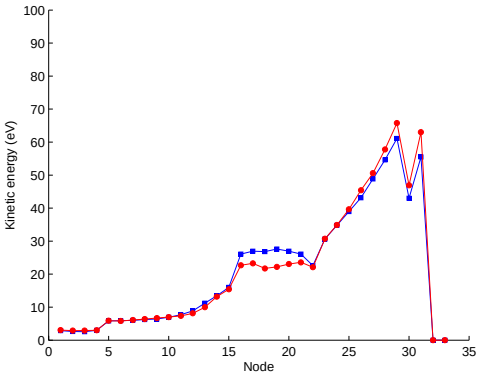

(c) Kinetic energy.

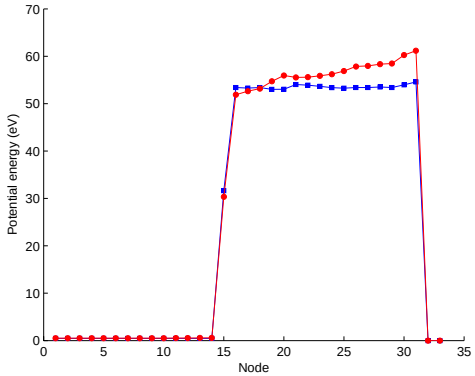

(d) Potential energy.

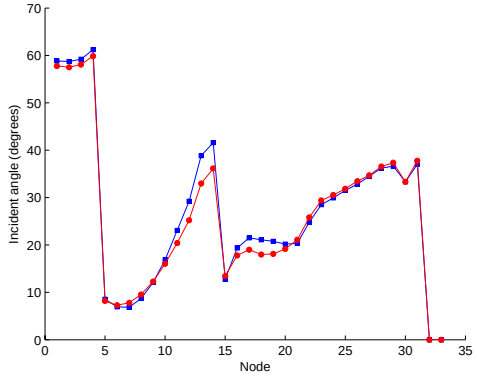

(e) Incident angle.

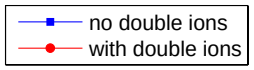

Figure 6-31: BHT-600: Averaged outer wall distributions during 80-153 hour run – effect of double ions.

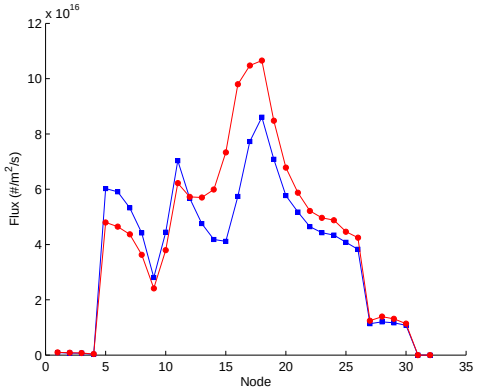

(a) Flux.

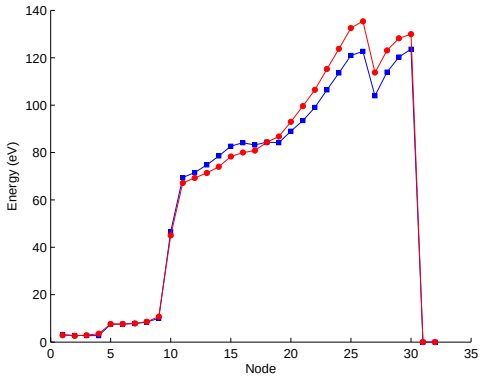

(b) Energy.

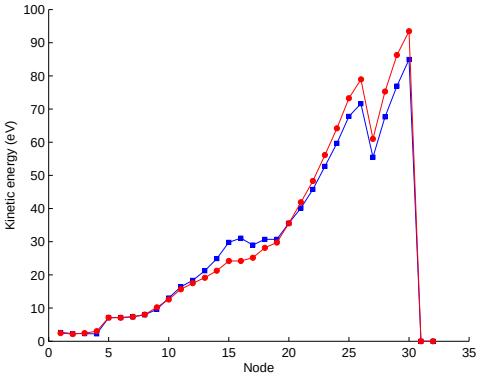

(c) Kinetic energy.

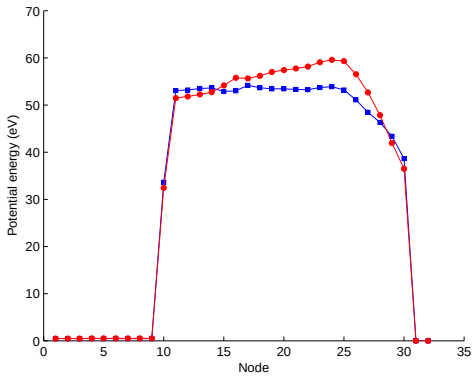

(d) Potential energy.

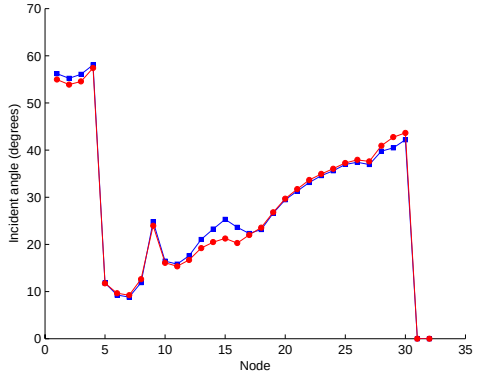

(e) Incident angle.

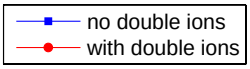

Figure 6-32: BHT-600: Averaged inner wall distributions during 80-153 hour run – effect of double ions.

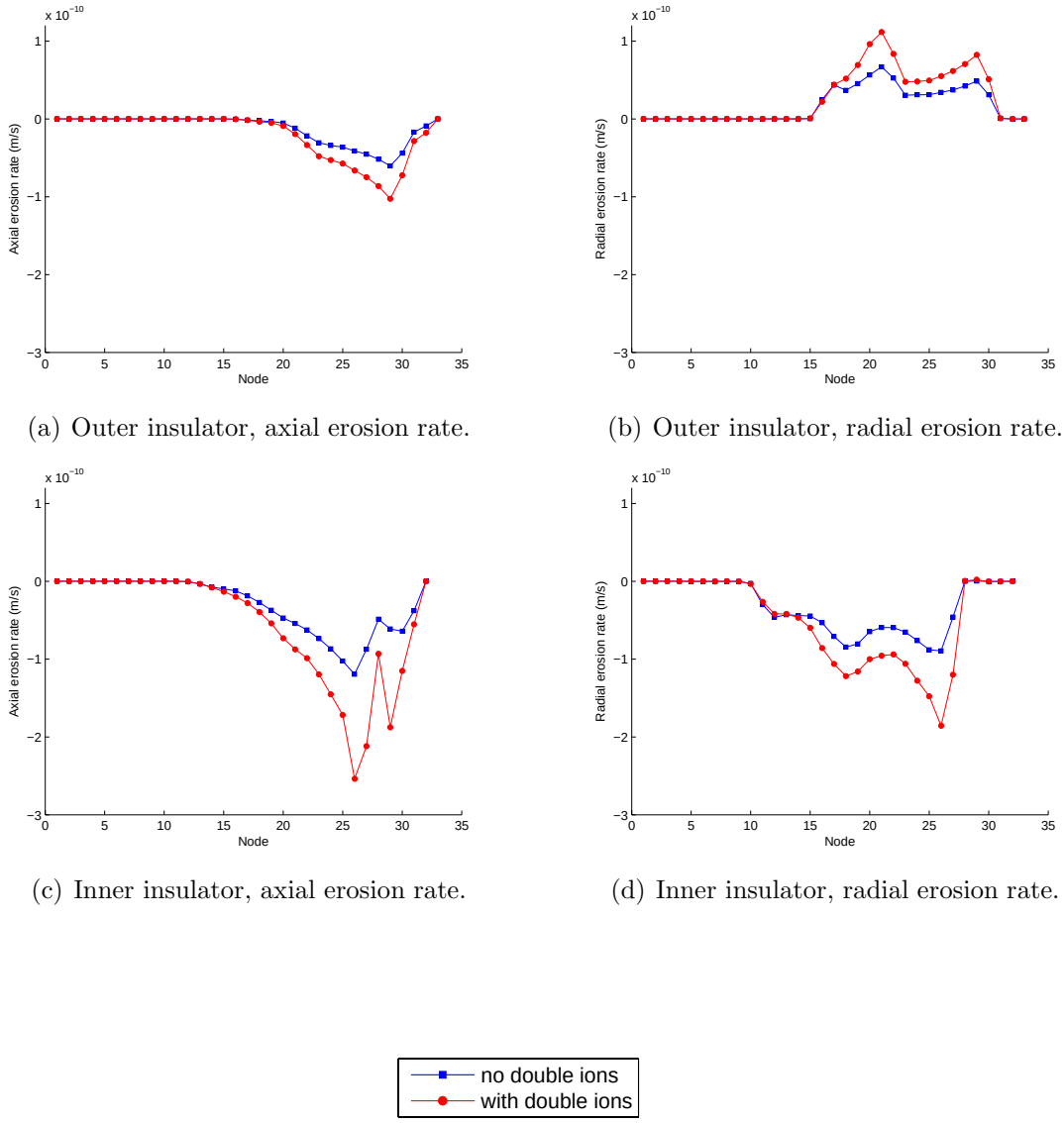

(a) Outer insulator, axial erosion rate.

(b) Outer insulator, radial erosion rate.

(c) Inner insulator, axial erosion rate.

(d) Inner insulator, radial erosion rate.

Figure 6-33: BHT-600: Wall erosion rates during 80-153 hour run – effect of double ions.

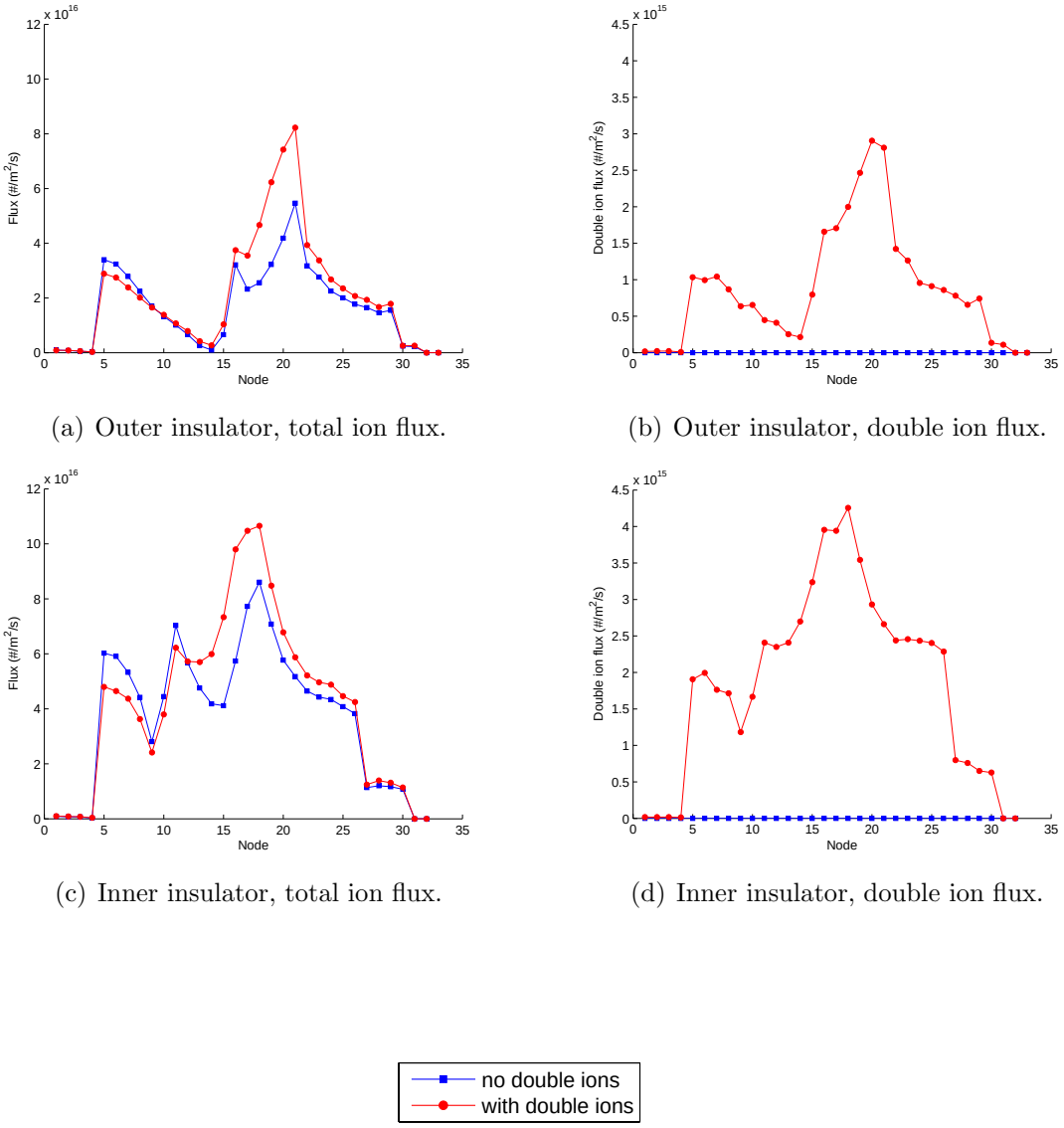

(a) Outer insulator, total ion flux.

(b) Outer insulator, double ion flux.

(c) Inner insulator, total ion flux.

(d) Inner insulator, double ion flux.

Figure 6-34: BHT-600: Flux comparison – effect of double ions.

Chapter 7

Conclusion

This chapter discusses the results, identifies contributions made to the field and concludes with recommendations for further work.

7.1 Discussion of results

The problem of Hall thruster lifetime prediction has been addressed by developing a computational method and testing it with two thruster geometries. Though the model does not exactly reproduce experimental erosion profiles, it does provide wall regression rates of the right order throughout the thruster's lifetime. As a result, overall agreement of the channel evolution is achieved.

As evidenced in the work with the BHT-200, it is possible to tune the simulation to a shorter test and then complete the life test numerically. Throughout the cases of Chapter 5, simulated erosion profiles for the first 100 hours of thruster operation appear almost identical and it is not until later times that differences can be discerned. Thus, if a short-duration test is to be used for simulation tuning, it should be long enough that a reasonable amount of wall material has been removed. For the BHT-200, 300 hours is sufficient. When the same approach is applied to the BHT-600, reasonable agreement is achieved with the later profiles, but more work on the transport model is needed to correctly place the plasma in the discharge channel. Nevertheless, features observed during the early stages of the simulation are carried

through the virtual lifetime test. Thus, matching of profiles early in life would lead to accurate predictions of those later in life.

Despite the model's success at capturing erosion behavior, it is deficient at simultaneously reproducing performance parameters. Cases that agree better with nominal discharge current and thrust do not necessarily correlate with improved wear prediction. Hence, the matching of simulated and experimental bulk properties does not provide insight into whether the detailed plasma distribution is correct or not. Since close attention is paid to the geometry and magnetic field definitions, this shortcoming of the simulation can be attributed to a lack of understanding in the sputter yield and anomalous transport models. By adjusting the sputtering model via the sputter threshold and the transport model via the Bohm coefficient, cathode line location and transport barrier position, agreement to either the erosion or the performance can be attained. Though tuning was extensive, it was not exhaustive and it is possible the correct combination of parameters could yield success on both metrics. However, the uncertainty in both fundamental physics models suggests further basic research is needed before progressing with the lifetime issue. Along with a deeper theoretical insight into the low-energy sputtering and anomalous transport processes, experimental measurements of sputter yield at low energy and internal discharge plasma parameters are key to the continued development of accurate lifetime prediction models. Although the thruster erosion profiles can serve as an interior diagnostic by dispensing clues about the energies of ions flowing to the walls, concrete data such as the potential or plasma density profile along the channel would enable pinning of the computational model to reality.

7.2 Contributions

- A multi-scale Hall thruster model that spans time scales on the order of tens of nanoseconds up to hundreds of hours has been developed to predict the erosion mechanisms that determine the lifetime of the device. The attention paid to definition of thruster geometry and magnetic field has eliminated these param-

eters as sources of error and allows closer examination of possible discrepancies in the underlying physics models.

- At the discharge voltages studied in this thesis, ions predominantly fall in the near-threshold regime of sputtering. Historically a difficult region to study, the results from this model suggest a sputter threshold of 30 eV or less for the grade of boron nitride used in the thrusters considered.

- Anomalous transport plays a critical role in determining the plasma discharge behavior and its subsequent erosion of the channel walls. To proceed further in this work, more theory and experimental data are needed.

- Two thrusters with significantly different geometries were studied. The contrast in evolution of erosion profiles for each points to the problem being unique to each thruster. Thus, lifetime prediction models must be detailed in taking these disparities into account and generic approaches to the issue are not adequate.

- Experimental data are necessary for proper tuning of the model for a specific thruster. A wall profile exhibiting a reasonable amount of material removal is preferred. For the BHT-200, a profile taken after 300 hours of operation is sufficient to characterize the thruster's erosion behavior. The simulation can then be used to complete the remainder of the life test. Note that 300 hours is a minimum recommendation for this thruster – having more data from later in life is always desirable for further validation and other thrusters may have different representative times.

- To validate that plasma properties are accurately modeled computationally, a detailed comparison to internal data is necessary. At present, erosion profiles are the best internal diagnostic available for this purpose. Assuming a simulation works based solely on matching of bulk performance parameters is both incorrect and unwise.

- Double ions are found to contribute greatly to the thruster erosion. Despite

composing a small part of the total wall particle flux, their increased energies place them higher on the sputter yield curve and result in significant wear.

- A tool that provides geometry evolution and wall erosion rates in the right range throughout the thruster lifetime has been developed. As a design tool, the simulation gives a sense of where weak points of the thruster may develop and cause eventual failure. As a qualification tool, the simulation approximates the time duration a thruster will last until its channel walls are eroded through.

7.3 Recommendations

In the process of completing this research, several areas that should be addressed to support further work in lifetime prediction were encountered.

- Basic understanding of the low-energy sputter yield behavior for relevant thruster materials is mandatory for accurately predicting erosion and lifetime. Though the detailed shape of the low-energy yield curve is most desirable, a good measurement of the absolute sputter threshold would do much to resolve confusion in the field.

- Anomalous transport is another poorly understood area of Hall thruster physics and deserves careful consideration. Development of theory to explain the phenomenon would greatly aid simulations, which currently resort to arbitrarily trying different Bohm coefficients and transport barriers. Of utmost importance is understanding the nature of the barrier formation as well as its dependency on thruster properties and operating conditions. In the interim, experimental measurements of electron mobility for more thrusters would give a clearer picture of how its behavior changes from one device to another.

- Internal thruster measurements would assist modelers in validating whether their codes are accurately describing the discharge. Most thruster simulations use performance parameters such as discharge current and thrust as their primary success metrics – while these are important to match, they represent

average properties of the engine and do little to ensure the detailed plasma property distributions inside the acceleration region are properly represented.

- This thesis addressed modeling of two different thrusters at their nominal operation points, but much could also be learned from investigating a single thruster operated at various conditions. Verification of a tuned code at disparate firing parameters would give further confidence that all relevant physics is accounted for. Along this line, comparison to more thruster models would serve as additional validation.

- Deposition of sputtered products on surfaces internal and external to the acceleration channel is observed during thruster operation. The effect that interior residue accumulation has on thruster lifetime has not been considered in this study. A model for outgoing sputter distributions could be implemented and eroded material tracked to determine its surface redeposition and dispersion through the plume. However, much work in understanding the basic physics of the behavior of ejected sputter material would first be required.

- Use of an axisymmetric simulation models the erosion as having azimuthal uniformity about the thruster annulus. However, experimental observations indicate that thruster erosion does not occur evenly about the acceleration channel circumference. To fully study the erosion patterns, a three-dimensional model that includes the cathode and near-exit region would be necessary.

- For thrusters operating at higher voltages, wall temperatures may no longer lie in the safe region of the sputter yield temperature dependence curve. Both data and theory are required to incorporate the effects of the surface temperature on sputtering.

- Implementing the model within a full PIC simulation would allow validation that the important erosion physics are being captured in the computational models. In addition, the more-detailed method may provide further insight into issues such as the nature of the transport barrier and its effect on the plasma.

Bibliography

[1] Abgaryan, V., H. Kaufman, V. Kim, D. Ovsyanko, I. Shkarban, A. Semenov, A. Sorokin and V. Zhurin, "Calculation Analysis of the Erosion of the Discharge Chamber Walls and Their Contamination During Prolonged SPT Operation." AIAA-1994-2859, 30^{th} AIAA/ASME/SAE/ASEE Joint Propulsion Conference and Exhibit, Indianapolis, IN, June 1994.

[2] Absalamov, S. K., V. B. Andreev, T. Colbert, M. Day, V. V. Egorov, R. U. Gnizdor, H. Kaufman, V. Kim, A. Korakin, K. N. Kozubsky, S. S. Kudravzev, U. V. Lebedev, G. A. Popov and V. V. Zhurin, "Measurement of Plasma Parameters in the Stationary Plasma Thruster (SPT-100) Plume and its Effects on Spacecraft Components." AIAA-1992-3156, 28^{th} AIAA/ASME/SAE/ASEE Joint Propulsion Conference and Exhibit, Nashville, TN, July 1992.

[3] Ahedo, E., I. Maqueda, A. Anton, Y. Raitses and N. J. Fisch, "Numerical simulations of a 2kW Hall thruster." AIAA-2006-4655, 42^{nd} AIAA/ASME/SAE/ASEE Joint Propulsion Conference and Exhibit, Sacramento, CA, July 2006.

[4] Allis, M. K., N. Gascon, C. Vialard-Goudou, M. A. Cappelli and E. Fernandez, "A Comparison of 2-D Hybrid Hall Thruster Model to Experimental Measurements." AIAA-2004-3951, 40^{th} AIAA/ASME/SAE/ASEE Joint Propulsion Conference and Exhibit, Fort Lauderdale, FL, July 2004.

[5] Allis, M. K., C. A. Thomas, N. Gascon, M. A. Cappelli and E. Fernandez, "Introduction of Physical Transport Mechanisms into 2D Hybrid Hall Thruster

Simulations." AIAA-2006-4325, 42^{nd} AIAA/ASME/SAE/ASEE Joint Propulsion Conference and Exhibit, Sacramento, CA, July 2006.

[6] Arkhipov, B., R. Gnizdor, K. N. Kozubsky and N. A. Maslennikov, "SPT-100 Module Lifetime Test Results." AIAA-1994-2854, 30^{th} AIAA/ASME/SAE/ASEE Joint Propulsion Conference and Exhibit, Indianapolis, IN, June 1994.

[7] Arkhipov, B., A. S. Bober, R. Y. Gnizdor, K. N. Kozubsky, A. I. Korakin, N. A. Maslennikov and S. Y. Pridannikov, "The Results of 7000-Hour SPT-100 Life Testing." IEPC-1995-39, 24^{th} International Electric Propulsion Conference, Moscow, Russia, September 1995.

[8] Baranov, V. I., Y. S. Nazarenko, V. A. Petrosov, A. I. Vasin and Y. M. Yashnov, "The Mechanism of Anomalous Erosion in Accelerators with Closed Drift of Electrons." IEPC-1995-43, 24^{th} International Electric Propulsion Conference, Moscow, Russia, September 1995.

[9] Baranov, V., Y. Nazarenko and V. Petrosov, "The Wear of the Channel Walls in Hall Thrusters." IEPC-2001-48, 27^{th} International Electric Propulsion Conference, Pasadena, CA, October 2001.

[10] Belikov, M. B., N. V. Blinov and O. A. Gorshkov, "Operation Peculiarities of Hall Thruster with Power 1.5-2.0 kW at High Discharge Voltages." IEPC-2003-121, 28^{th} International Electric Propulsion Conference, Toulouse, France, March 2003.

[11] Bugrova, A. I., A. M. Bishaev, A. V. Desyatskov, M. V. Kozintseva and M. Prioul, "Spectral Investigation of SPT MAG Insulator Erosion." IEPC-2005-167, 29^{th} International Electric Propulsion Conference, Princeton, NJ, October 2005.

[12] Cappelli, M. A., N. B. Meezan and N. Gascon, "Transport Physics in Hall Plasma

Thrusters." AIAA-2002-0485, 40^{th} AIAA Aerospace Sciences Meeting and Exhibit, Reno, NV, January 2002.

[13] Chen, M., G. Rohrbach, A. Neuffer, K. -L. Barth and A. Lunk. "Simulation of Boron Nitride Sputtering Process and Its Comparison with Experimental Data." *IEEE Transactions on Plasma Science*, 26(6):1713-1717, December 1998.

[14] Cheng, S. Y., *Computational Modeling of a Hall Thruster Plasma Plume in a Vacuum Tank*, SM Thesis, Massachusetts Institute of Technology, February 2002.

[15] Clauss, C., M. Day, V. Kim, Y. Kondakov and T. Randolph, "Preliminary Study of Possibility to Ensure Large Enough Lifetime of SPT Operating Under Increased Powers." AIAA-1997-2789, 33^{rd} AIAA/ASME/SAE/ASEE Joint Propulsion Conference and Exhibit, Seattle, WA, July 1997.

[16] Dankanich, J. W. and T. Polsgrove, "Mission Benefits of Gridded Ion and Hall Thruster Hybrid Propulsion Systems." AIAA-2006-5162, 42^{nd} AIAA/ASME/SAE/ASEE Joint Propulsion Conference and Exhibit, Sacramento, CA, July 2006.

[17] de Grys, K., B. Welander, J. Dimicco, S. Wenzel, B. Kay, V. Khayms and J. Paisley, "4.5 kW Hall Thruster System Qualification Status." AIAA-2005-3682, 41^{st} AIAA/ASME/SAE/ASEE Joint Propulsion Conference and Exhibit, Tucson, AZ, July 2005.

[18] Doerner, R. P., S. I. Krasheninnikov and K. Schmid. "Particle-induced erosion of materials at elevated temperature." *Journal of Applied Physics*, 95(8):4471-4475, 15 April 2004.

[19] Doerner, R. P., M. J. Baldwin, S. I. Krasheninnikov and K. Schmid. "High temperature erosion of beryllium." *Journal of Nuclear Materials*, 337-339:877-881, 1 March 2005.

[20] Dyshlyuk, E. N. and O. Gorshkov, "Spectroscopic Investigation of a Hall Thruster Ceramic Acceleration Channel Erosion Rate." AIAA-2006-4660, 42^{nd}

AIAA/ASME/SAE/ASEE Joint Propulsion Conference and Exhibit, Sacramento, CA, July 2006.

[21] Elovikov, S. S., V. A. Eltekov, N. N. Negrebetskaya, J. V. Sushkova, V. E. Yurasova, I. I. Shkarban, O. I. Buzhinskij and I. V. Opimach. "The sputtering of different modifications of boron nitride under ion and electron irradiation." *Journal of Nuclear Materials*, 212-215(2):1335-1338, September 1994.

[22] Elovikov, S. S., E. Yu. Zykova, A. A. Semenov, I. I. Shkarban and V. E. Yurasova. "Dependence of boron nitride sputtering on ion energy, mass, and incidence angle." *Bulletin of Russian Academy of Sciences: Physics*, 66(4):608-612, 2002.

[23] Elovikov, S. S., I. K. Khrustachev, A. S. Mosunov and V. E. Yurasova. "Mass Dependence of Nitride Sputtering." *Radiation Effects and Defects in Solids*, 158(8):573-582, August 2003.

[24] Fernandez, E., M. A. Cappelli and K. Mahesh. "2D simulations of Hall thrusters." *CTR Annual Research Briefs*, 81-90, 1998.

[25] Fife, J. M., *Two-Dimensional Hybrid Particle-In-Cell Modeling of Hall Thrusters*, SM Thesis, Massachusetts Institute of Technology, May 1995.

[26] Fife, J. M., *Hybrid-PIC Modeling and Electrostatic Probe Survey of Hall Thrusters*, PhD Thesis, Massachusetts Institute of Technology, September 1998.

[27] Fox, J. M., *Parallelization of a Particle-in-Cell Simulation Modeling Hall-Effect Thrusters*, SM Thesis, Massachusetts Institute of Technology, January 2005.

[28] Fox, J. M., A. A. Batishcheva, O. V. Batishchev and M. Martinez-Sanchez, "Adaptively Meshed Fully-Kinetic PIC-Vlasov Model For Near Vacuum Hall Thrusters." AIAA-2006-4324, 42^{nd} AIAA/ASME/SAE/ASEE Joint Propulsion Conference and Exhibit, Sacramento, CA, July 2006.

[29] Franke, E., H. Neumann, M. Zeuner, W. Frank and F. Bigl. "Particle energy and angle distributions in ion beam sputtering." *Surface and Coatings Technology*, 97(1-3):90-96, December 1997.

[30] Frisbee, R. H., "Evaluation of High-Power Solar Electric Propulsion Using Advanced Ion, Hall, MPD, and PIT Thrusters for Lunar and Mars Cargo Missions." AIAA-2006-4465, 42^{nd} AIAA/ASME/SAE/ASEE Joint Propulsion Conference and Exhibit, Sacramento, CA, July 2006.

[31] Gamero-Castaño, M. and I. Katz, "Estimation of Hall Thruster Erosion Using HPHall." IEPC-2005-303, 29^{th} International Electric Propulsion Conference, Princeton, NJ, October 2005.

[32] Garner, C. E., J. R. Brophy, J. E. Polk and L. C. Pless, "Cyclic Endurance Test of a SPT-100 Stationary Plasma Thruster." AIAA-1994-2856, 30^{th} AIAA/ASME/SAE/ASEE Joint Propulsion Conference and Exhibit, Indianapolis, IN, June 1994.

[33] Garner, C. E., J. R. Brophy, J. E. Polk, S. Semenkin, V. Garkusha, S. Tverdokhlebov and C. Marrese, "Experimental Evaluation of Russian Anode Layer Thrusters." AIAA-1994-3010, 30^{th} AIAA/ASME/SAE/ASEE Joint Propulsion Conference and Exhibit, Indianapolis, IN, June 1994.

[34] Garner, C. E., J. R. Brophy, J. E. Polk and L. C. Pless, "A 5,730-Hr Cyclic Endurance Test of the SPT-100." AIAA-1995-2667, 31^{st} AIAA/ASME/SAE/ASEE Joint Propulsion Conference and Exhibit, San Diego, CA, July 1995.

[35] Garnier, Y., J. -F. Roussel and J. Bernard. "Low-energy xenon ion sputtering of ceramics investigated for stationary plasma thrusters." *Journal of Vacuum Science and Technology A*, 17(6):3246-3254, November-December 1999.

[36] Garrigues, L., G. J. M. Hagelaar, J. Bareilles, C. Boniface and J. P. Bouef. "Model study of the influence of the magnetic field configuration on the performance and lifetime of a Hall thruster." *Physics of Plasmas*, 10(12):4886-4892, December 2003.

[37] Gorshkov, O. A., A. A. Shagayda and S. V. Irishkov, "The Influence of the Magnetic Field Topology on Hall Thruster Performance." AIAA-2006-4472,

42^{nd} AIAA/ASME/SAE/ASEE Joint Propulsion Conference and Exhibit, Sacramento, CA, July 2006.

[38] Hagelaar, G. J. M., J. Bareilles, L. Garrigues and J. -P. Boeuf. "Two-dimensional model of a stationary plasma thruster." *Journal of Applied Physics*, 91(9):5592-5598, May 2002.

[39] Hall Effect Thruster Systems: Low Power Nominal Specifications. Busek Co. Inc. 1 May 2007 <http://www.busek.com/halleffect.html>.

[40] Personal communication with W. Hargus.

[41] Hofer, R. R., I. Katz, I. G. Mikellides and M. Gamero-Castaño, "Heavy Particle Velocity and Electron Mobility Modeling in Hybrid-PIC Hall Thruster Simulations." AIAA-2006-4658, 42^{nd} AIAA/ASME/SAE/ASEE Joint Propulsion Conference and Exhibit, Sacramento, CA, July 2006.

[42] Hofer, R. R., T. M. Randolph, D. Y. Oh, J. S. Snyder and K. H. deGrys, "Evaluation of a 4.5 kW Commercial Hall Thruster System for NASA Science Missions." AIAA-2006-4469, 42^{nd} AIAA/ASME/SAE/ASEE Joint Propulsion Conference and Exhibit, Sacramento, CA, July 2006.

[43] Jacobson, D. T., "High Voltage TAL Erosion Characterization." AIAA-2002-4257, 38^{th} AIAA/ASME/SAE/ASEE Joint Propulsion Conference and Exhibit, Indianapolis, IN, July 2002.

[44] Khartov, S., A. Nadiradze and O. Duchemin, "SPT Ceramic Isolator Surfaced Layer Composition Change with Lifetime." IEPC-2003-059, 28^{th} International Electric Propulsion Conference, Toulouse, France, March 2003.

[45] Khartov, S. A., A. B. Nadiradze, I. I. Shkarban and Y. V. Zikeeva, "SPT's high lifetime – some problems of solution." IEPC-2005-62, 29^{th} International Electric Propulsion Conference, Princeton, NJ, October 2005.

[46] Kim, V., V. Abgaryan, V. Kozlov, A. Skrylnikov and L. Jolivet, "Development of the Accelerated Test Procedure for the SPT Discharge Chamber Wall Wearing During Long Thruster Operation." AIAA-2003-5003, 39^{th} AIAA/ASME/SAE/ASEE Joint Propulsion Conference and Exhibit, Huntsville, AL, July 2003.

[47] Koo, J. W. and I. D. Boyd. "Computational model of a Hall thruster." *Computer Physics Communications*, 164(1-3):442-447, December 2004.

[48] Koo, J. W. and I. D. Boyd, "Anomalous electron mobility modeling in Hall thrusters." AIAA-2005-4057, 41^{st} AIAA/ASME/SAE/ASEE Joint Propulsion Conference and Exhibit, Tucson, AZ, July 2005.

[49] Le Godec, Y., D. Martinez-Garcia, V. L. Solozhenko, M. Mezouar, G. Syfosse and J. M. Besson. "Compression and thermal expansion of rhombohedral boron nitride at high pressures and temperatures." *Journal of Physics and Chemistry of Solids*, 61(12):1935-1938, December 2000.

[50] Lovtsov, A. S., A. A. Shagayda and O. A. Gorshkov, "Semi-Empirical Method of Hall Thrusters Lifetime Prediction." AIAA-2006-4661, 42^{nd} AIAA/ASME/SAE/ASEE Joint Propulsion Conference and Exhibit, Sacramento, CA, July 2006.

[51] Manzella, D., J. Yim and I. Boyd, "Predicting Hall Thruster Operational Lifetime." AIAA-2004-3953, 40^{th} AIAA/ASME/SAE/ASEE Joint Propulsion Conference and Exhibit, Fort Lauderdale, FL, July 2004.

[52] Marchandise, F. R., J. Biron, M. Gambon, N. Cornu, F. Darnon and D. Estublier, "The PPS-1350 qualification demonstration 7500h on ground, about 5000h in flight." IEPC-2005-209, 29^{th} International Electric Propulsion Conference, Princeton, NJ, October 2005.

[53] Marrese, C., J. E. Polk, L. B. King, C. Garner, A. D. Gallimore, S. Semenkin, S. Tverdoklebov and V. Garkusha, "Analysis of Anode Layer Thruster Guard

Ring Erosion." IEPC-1995-196, 24^{th} International Electric Propulsion Conference, Moscow, Russia, September 1995.

[54] Martinez-Sanchez, M. and J. E. Pollard. "Spacecraft Electric Propulsion – An Overview." *Journal of Propulsion and Power*, 14(5):688-699, September-October 1998.

[55] Martinez-Sanchez, M., *16.522 Space Propulsion class notes*, Massachusetts Institute of Technology, Spring 2000.

[56] Maslennikov, N. A., "Lifetime of the Stationary Plasma Thruster." IEPC-1995-75, 24^{th} International Electric Propulsion Conference, Moscow, Russia, September 1995.

[57] Mason, L. S., R. S. Jankovsky and D. H. Manzella, "1000 Hours of Testing on a 10 Kilowatt Hall Effect Thruster." AIAA-2001-3773, 37^{th} AIAA/ASME/SAE/ASEE Joint Propulsion Conference and Exhibit, Salt Lake City, UT, July 2001.

[58] Morozov, A. I. and V. V. Savelyev, "The Electron Dynamics in SPT-Channel and the Problem of Anomalous Erosion." IEPC-1995-42, 24^{th} International Electric Propulsion Conference, Moscow, Russia, September 1995.

[59] Mosunov, A. S., A. A. Promokhov, D. S. Colligon and V. E. Yurasova. "Sputtering Mechanisms of Boron Nitride Single Crystals." *Bulletin of Russian Academy of Sciences: Physics*, 62(4):556-561, 1998.

[60] Nakles, M. R., W. A. Hargus and D. B. VanGilder, "Comparison of Numerical and Experimental Near-Field Ion Velocity Distributions of the BHT-200-X3 Hall Thruster." AIAA-2006-4479, 42^{nd} AIAA/ASME/SAE/ASEE Joint Propulsion Conference and Exhibit, Sacramento, CA, July 2006.

[61] Parra, F. I., E. Ahedo, J. M. Fife and M. Martinez-Sanchez. "A two-dimensional hybrid model of the Hall thruster discharge." *Journal of Applied Physics*, 100(2):023304, July 2006.

[62] Peterson, P. Y. and D. H. Manzella, "Investigation of the Erosion Characteristics of a Laboratory Hall Thruster." AIAA-2003-5005, 39^{th} AIAA/ASME/SAE/ASEE Joint Propulsion Conference and Exhibit, Huntsville, AL, July 2003.

[63] Petrosov, V. A., A. I. Vasin, V. I. Baranov, J. R. Wetch, E. J. Britt, S. P. Wong and R. Lin, "A 2000 Hours Lifetime Test Results of 1.3 kW T-100 Electric Thruster." IEPC-1995-41, 24^{th} International Electric Propulsion Conference, Moscow, Russia, September 1995.

[64] Petrosov, V. A., V. I. Baranov, A. I. Vasin, A. A. Kaliaev and Y. S. Nazarenko, "The SPT Channel Erosion Model." IEPC-1995-60, 24^{th} International Electric Propulsion Conference, Moscow, Russia, September 1995.

[65] Promokhov, A. A., A. S. Mosunov, S. S. Elovikov and V. E. Yurasova. "Features of sputtering of nitrides with various component mass ratios." *Vacuum*, 56(4):247-252, March 2000.

[66] Raneev, A. N., A. A. Semenov and O. B. Solovyev, "Surface temperature influence onto ceramic sputtering rate." XIII International Conference about Ion Interaction with a Surface, Moscow, Russia, 1997, as documented in [45].

[67] Reinke, S., M. Kuhr and W. Kulisch. "Critical test of the c-BN sputter model." *Surface and Coatings Technology*, 74-75(2):723-728, October 1995.

[68] Schmid, K., M. Baldwin and R. P. Doerner. "Modelling of thermally enhanced erosion of beryllium." *Journal of Nuclear Materials*, 348(3):294-301, 1 February 2006.

[69] Semenkin, A., A. Kochergin, A. Rusakov, V. Bulaev, J. Yuen, J. Shoji, C. Garner and D. Manzella, "Development Program and Preliminary Test Results of the TAL-110 Thruster." AIAA-1999-2279, 35^{th} AIAA/ASME/SAE/ASEE Joint Propulsion Conference and Exhibit, Los Angeles, CA, June 1999.

[70] Shutthanandan, V., J. Zhang and P. K. Ray. "On the preferential emission of heavy isotopes in sputtering." *Vacuum*, 52(3):353-357, March 1999.

[71] Smentkowski, V. S. "Trends in sputtering." *Progress in Surface Science*, 64(1-2):1-58, May 2000.

[72] Solodukhin, A. E. and A. V. Semenkin, "Study of Discharge Channel Erosion in Multi Mode Anode Layer Thruster." IEPC-2003-0204, 28^{th} International Electric Propulsion Conference, Toulouse, France, March 2003.

[73] Sommier, E., M. K. Allis and M. A. Cappelli, "Wall Erosion in 2D Hall Thruster Simulations." IEPC-2005-189, 29^{th} International Electric Propulsion Conference, Princeton, NJ, October 2005.

[74] Sommier, E., M. K. Allis, N. Gascon and M. A. Cappelli, "Wall Erosion in 2D Hall Thruster Simulations." AIAA-2006-4656, 42^{nd} AIAA/ASME/SAE/ASEE Joint Propulsion Conference and Exhibit, Sacramento, CA, July 2006.

[75] Szabo, J. J., M. Martinez-Sanchez and J. Monheiser, "Application of a 2-D Hybrid PIC Code to Alternative Hall Thruster Geometries." AIAA-1998-3795, 34^{th} AIAA/ASME/SAE/ASEE Joint Propulsion Conference and Exhibit, Cleveland, OH, July 1998.

[76] Tverdokhlebov, O. S. and G. F. Karabadzhak, "TAL Relative Erosion Rate Real-Time Measurements Through Analysis of its Emission Spectra." IEPC-2003-0336, 28^{th} International Electric Propulsion Conference, Toulouse, France, March 2003.

[77] Vinogradov, V. N., V. M. Murashko and F. Scortecci. "Cost-Optimum Electric Propulsion for Constellations." *Journal of Spacecraft and Rockets*, 39(1):146-149, January-February 2002.

[78] Welander, B., C. Carpenter, K. de Grys, R. R. Hofer and T. M. Randolph, "Life and Operating Range Extension of the BPT-4000 Qualification Model Hall

Thruster." AIAA-2006-5263, 42^{nd} AIAA/ASME/SAE/ASEE Joint Propulsion Conference and Exhibit, Sacramento, CA, July 2006.

[79] Winski, R., J. Wang, C. Carpenter, J. Cassady and A. Hoskins, "Lunar Robotic Precursor Missions Using Electric Propulsion." AIAA-2006-5165, 42^{nd} AIAA/ASME/SAE/ASEE Joint Propulsion Conference and Exhibit, Sacramento, CA, July 2006.

[80] Yalin, A. P., V. Surla, C. Farnell, M. Butweiller and J. D. Williams, "Sputtering Studies of Multi-Component Materials by Weight Loss and Cavity Ring-Down Spectroscopy." AIAA-2006-4338, 42^{nd} AIAA/ASME/SAE/ASEE Joint Propulsion Conference and Exhibit, Sacramento, CA, July 2006.

[81] Yamamura, Y. "An Empirical Formula for Angular Dependence of Sputtering Yields." *Radiation Effects and Defects in Solids*, 80(1-2):57-72, February 1984.

[82] Yamamura, Y. and H. Tawara. "Energy Dependence of Ion-Induced Sputtering Yields from Monatomic Solids at Normal Incidence." *Atomic Data and Nuclear Data Tables*, 62(2):149-253, March 1996.

[83] Yim, J. T., M. Keidar and I. D. Boyd, "An Evaluation of Sources of Erosion in Hall Thrusters." AIAA-2005-3530, 41^{st} AIAA/ASME/SAE/ASEE Joint Propulsion Conference and Exhibit, Tucson, AZ, July 2005.

[84] Yim, J. T., M. Keidar and I. D. Boyd, "A Hydrodynamic-Based Erosion Model for Hall Thrusters." IEPC-2005-013, 29^{th} International Electric Propulsion Conference, Princeton, NJ, October 2005.

[85] Yim, J. T., M. Keidar and I. D. Boyd, "An Investigation of Factors Involved in Hall Thruster Wall Erosion Modeling." AIAA-2006-4657, 42^{nd} AIAA/ASME/SAE/ASEE Joint Propulsion Conference and Exhibit, Sacramento, CA, July 2006.

[86] Yamamoto, N., S. Yokota, M. Matsui, K. Komurasaki and Y. Arakawa, "Estimation of Erosion Rate by Absorption Spectroscopy in a Hall Thruster." IEPC-2005-

037, 29^{th} International Electric Propulsion Conference, Princeton, NJ, October 2005.

[87] Zhang, J., S. Bhattacharjee, V. Shutthanandan and P. K. Ray. "Sputtering investigation of boron nitride with secondary ion and secondary neutral mass spectrometry." *Journal of Vacuum Science and Technology A*, 15(2):243-247, March-April 1997.